FACULTY OF SCIENCE
UNIVERSITY OF COPENHAGEN

MID-IR SPECTROSCOPY OF STAR-FORMING GALAXIES ACROSS COSMIC TIME

MASTER THESIS

Evangelos-Dimitrios Paspaliaris
dqh550@alumni.ku.dk

Supervisors:
Georgios Magdis, Vassilios Charmandaris, Sune Toft

Submitted on:
20 November 2018

CONTENTS

ACKNOWLEDGEMENTS

Firstly I would like to express my gratefulness to my supervisors Prof. Georgios Magdis [1,2], Prof. Vassilios Charmandaris [3,4] and Prof. Sune Toft [1,2] for giving me the opportunity to do research in the context of a very interesting thesis project and helping me improve my cognitive level in this topic and generally in the methods of doing research.

I would also like to thank Prof. Hanae Inami[5] and Dr. Tanio Diaz-Santos[6] for their really useful advises and comments on my work. Moreover, I would like to thank Michael Kottas [4] for his comments during my efforts to create a fast Python code that calculates the median spectra.

My studies would have been impossible without the support from my family. I also thank my cousin Constantinos for sheltering me during my first months in Athens. I would also like to thank all my new friends at the National Observatory of Athens, for their help and the interesting discussions we had. Finally, I thank my girlfriend Katerina for supporting me during this year.

This research has made use of the NASA/IPAC Infrared Science Archive (IRSA) and Extragalactic Database (NED), which are operated by the Jet Propulsion Laboratory, California Institute of Technology, under contract with the National Aeronautics and Space Administration (NASA). The Spitzer Space Telescope is operated by the Jet Propulsion Laboratory, California Institute of Technology, under NASA contract 1407.

1 Cosmic Dawn Center (DAWN), Niels Bohr Institute, University of Copenhagen, Denmark
2 Dark Cosmology Centre, Niels Bohr Institute, University of Copenhagen, Denmark
3 Department of Physics, University of Crete, Greece
4 Institute for Astronomy, Astrophysics, Space Applications and Remote Sensing, National Observatory of Athens, Greece
5 Centre de Recherche Astrophysique de Lyon (CRAL), Univ Lyon, Saint- Genis-Laval, France
6 Universidad Diego Portales, Santiago, Chile

ABSTRACT

The mid-infrared part of the spectrum of galaxies is rich in spectral features that can serve as a powerful tool to study their physical properties and characterize the physical conditions of the interstellar medium. In this project I combine Spitzer/IRS spectra of IR-luminous galaxies at a wide range of redshifts in order to detect and investigate the weak 3.3 μm polycyclic aromatic hydrocarbon (PAH) emission feature. The 3.3 μm and the 6.2 μm PAH features are widely used as indicators for the starburst (SB) and active galactic nucleus (AGN) powering mechanisms of local star-forming galaxies. However, the 3.3μm feature will be the only observable PAH feature at redshifts higher than 3.5. Thus, this is a preparatory project that characterizes the emission of the 3.3 μm PAH feature of high-redshift sources and could serve as a recipe for the forthcoming observations with the James Webb Space Telescope (JWST), targeting this feature.

1

INTRODUCTION

1.1 OBSERVING GALAXIES IN THE INFRARED

The existence of a population of InfraRed (IR) luminous galaxies in the local Universe, whose number density rises and becomes significant in high redshifts was an important result by the observations of the InfraRed Astronomy Satellite (IRAS; Soifer, Neugebauer, and Houck 1987) which was launched by the National Aeronautics and Space Administration (NASA) in 1983. Following IRAS, the Cosmic Background Explorer (COBE) space mission, which was launched in 1989, made fundamental contributions to the study of the Cosmic Infrared Background (CIB; Puget et al. 1996). The intensity of the CIB is unexpectedly high, in comparison to the optical light from galaxies of the Hubble Deep Field (Hauser et al. 1998). Moreover, it suggests that the star formation rate (SFR) is at least two times higher than the one estimated from ultraviolet(UV)/optical observations. Hence, this was the first strong evidence that at least half of the star formation in the Universe is obscured by dust and that half of the energy is emitted in IR.

With the contribution of later launched IR missions, such as the Spitzer Space Telescope (Werner et al. 2004) and the Herschel Space Observatory (Pilbratt et al. 2010), the Spectral Energy Distribution (SED) and also the surface brightness of the CIB were measured in better detail. Although how the contribution of the galaxies to the CIB evolves at various redshifts is still under investigation, the current available results make clear that dust provides information for the galaxy evolution that

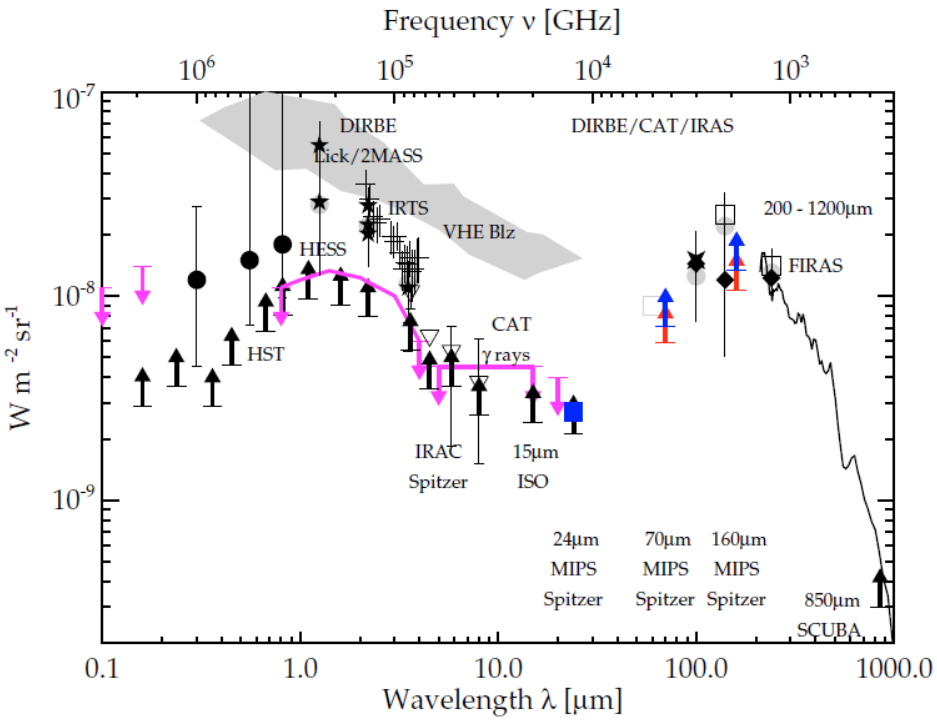

Figure 1: The Spectral Energy Destribution (SED) of the extragalactic background light from 0.1 μm to 1 mm by Dole et al. 2005. The Cosmic Optical Background (COB) covers the area of $\lambda \leq 8\mu$m while the Cosmic InfraRed Background (CIB) the area of $\lambda > 8\mu$m.

cannot be provided from any other source. As is illustrated in Fig. 1, the CIB coming from dusty galaxies constitutes half of the information of the extragalactic background light (EBL; Dole et al. 2005; Hauser et al. 2001). EBL is the integrated energy emitted by all the galaxies; thus, observations of dusty IR-luminous galaxies are important for the investigation and understanding of the energy density as a function of redshift, in the Universe.

IRAS measured IR thermal emission in almost the whole sky, using its four bands, centered at 12, 25, 60 and 100μm. Although the IR-luminous galaxies are locally rare (Lonsdale et al. 2006) and their contribution on the total energy density is about 3% (Soifer and Neugebauer 1991), their high IR-luminosity ($L_{8-1000\mu m} > 10^{11} L_{\odot}$) allowed IRAS not to be restricted at the limits of the local Universe and observe such sources also at high redshifts (Rowan-Robinson et al. 1991). The result

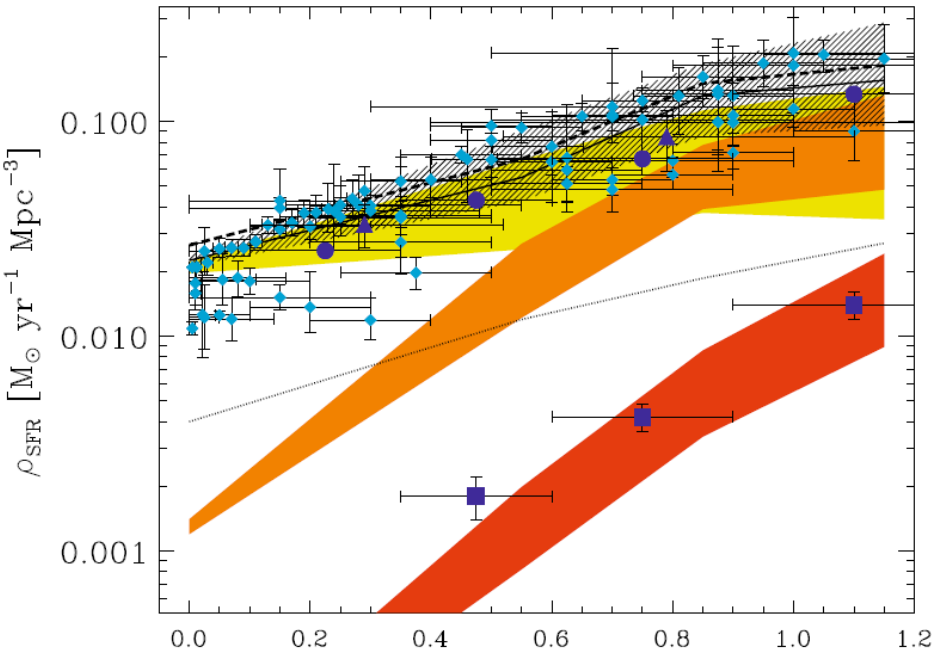

Figure 2: The star formation rate (SFR) density of the universe up to redshift ∼1.2. and the different contributions of the normal galaxies (yellow area), the LIRGs (orange area) and ULIRGs (red area) (Magnelli et al. 2009).

of these observations was the creation of several important samples of IRAS (U)LIRGs[1], like the Revised Bright Galaxy Sample (RBGS) of Sánchez et al. 2004, the 2Jy sample of Strauss et al. 1990 and the FIRST/IRAS sample of Stanford et al. 2000, including more than 60,000 sources (Surace et al. 1998).

The Infrared Space Observatory (ISO; Kessler et al. 1996) also contributed in resolving the CIB by observing extragalactic sources. Its observations confirmed that the number of the IR-luminous dusty galaxies increases with redshift and that in z∼1 the IR light density is more than 40 times greater than in the local Universe. Additional observations in longer wavelengths, performed with the Sub-millimetre Common User Bolometer Array (SCUBA) also shew that the ULIRGs are a significant contributor at z $>$ 1 (Bertoldi et al. 2000; Fox et al. 2002; Borys et al. 2004; Webb et al.

1 Luminous Infrared Galaxy (LIRG): $10^{11}L_\odot < L_{8-1000\mu m} < 10^{12}L_\odot$

Ultra-Luminous Infrared Galaxy (ULIRG): $L_{8-1000\mu m} > 10^{12}L_\odot$,

where $L_\odot$ is the solar luminosity

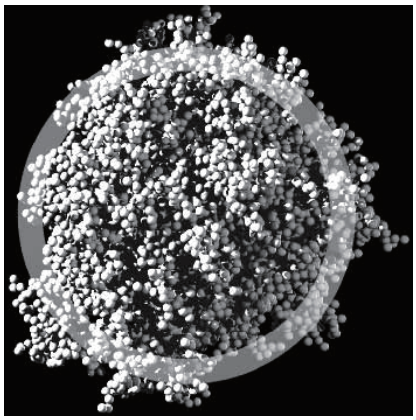

Figure 3: Micron size scale dust grain consisting of ∼8000 atoms in the three-dimensional numerical simulations by Wada et al. 2009. The grey ring indicates the size of the characteristic diameter.

2003). As we go at higher redshifts, LIRGs and ULIRGs dominate the star formation activity of the Universe as is shown in Fig. 2, that presents the SFR density of the universe up to z∼1.2. More specifically, the different contributions of the normal galaxies ($10^7 L_\odot < L_{8-1000\mu m} < 10^{11} L_\odot$) (yellow area), the LIRGs (orange area) and ULIRGs (red area) are also presented in the same figure of Magnelli et al. 2009.

1.2 DUST GRAINS AND MACROMOLECULES

The IR light coming from the star-forming galaxies discussed above, comes from the interstellar dust that is illuminated from starlight, consisting of UV and optical photons. The dust grains consist of tens of hundreds of atoms (Draine and Li 2001) and have diameter of micron size scale. They are mainly made of carbon and silicon. A dust grain that consists of 8000 particles is illustrated in Fig. 3. The production of these grains occurs at the late stages of the stellar evolution in the outer layers of the stars and the circumstellar areas. Later, the death of the stars followed by nova or supernova explosion leads to the spreading of the dust grains.

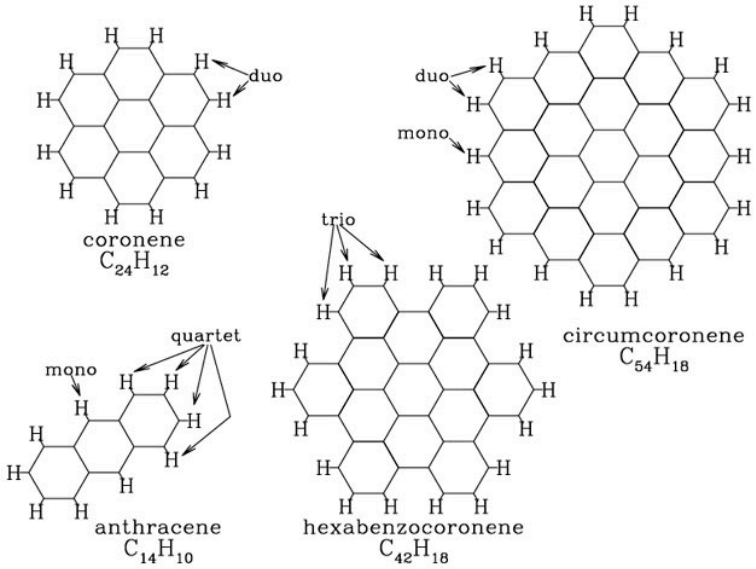

Figure 4: The molecular structure of several PAHs, indicating how individual benzene rings may be characterized by the number of their C-H bonds (from mono to quatro) (Draine 2003).

The absorbed starlight increases the dust grains thermal energy in the form of oscillations of their atoms. This thermal energy is then re-emitted in IR photons during the following cooling-down period (Draine 2003). The same procedure occurs at the macro-molecules in the dusty regions. In this thesis I investigate the emitted flux from the Polycyclic Aromatic Hydrocarbons (PAHs). During the first years of the IR spectroscopy, several spectral features emitted by PAHs were noticed. These features were observed in spectra of bright reflection nebulae, HII regions and planetary nebulae (Gillett et al. 1973; Soifer et al. 1976; Russell et al. 1977) and they are also conspicuous on the spectra of distant galaxies with vigorous star formation.

The PAHs are planar molecules that consist of carbon hexagon rings linked with hydrogen atoms. A single ring creates a benzene molecule. The molecular structure of more complex PAHs is illustrated in Fig 4. The IR emission arises from vibrationally excited PAHs and specifically from the stretching or bending of the C-H and C-C bonds. The contribution of their emission is about 10% - 20% of the total IR emission of galaxies (Helou et al. 2001; Peeters et al. 2002; Smith et al. 2007).

1.3 DUST EMISSION FROM GALAXIES

Dust-rich galaxies emit in the IR part of the electromagnetic spectrum and specifically in the range of 2.2-1,000 μm. The radiation emitted mainly by young stars is absorbed and then re-emitted by dust, being imprinted on the spectrum with the form of several broad emission features, emission lines, power law continuum in its mid-IR part and as black-body (BB) radiation in its far-IR part respectively. Fig. 5 shows two different SEDs of a star-forming galaxy with SFR of 100 $M_{\odot}$/yr and stellar mass of 5×10^5 $M_{\odot}$, where $M_{\odot}$ is the solar mass. The black SED corresponds to the case that the galaxy does not contain interstellar dust, while the red SED corresponds to the dusty version of the same galaxy. The SED is made with the CIGALE code (Code Investigating GALaxy Emission; Noll et al. 2009; Ciesla et al. 2015). The dusty galaxy shows no emission in shorter wavelengths than the Lyman-limit (0.912 μm) and is generally less luminous in the UV and optical, because these parts of the spectrum are absorbed by the dust and re-emitted in the IR, from 2.2 to 1,000 μm. In contrast, the dust-free galaxy emits less in the mid-IR and does not show any emission in the far-IR. Therefore, by the comparison of these two SEDs, it is obvious that the UV and optical observations are not enough to provide the full information of a dusty star-forming galaxy.

IR features emitted from regions powered by young massive stars, such as HII regions of dusty galaxies, are very strong and can be used as quantitative tracers of intense galactic star formation. Some of the characteristics of these features, like the peak's position or their width, vary due to the physical conditions of the region that they were emitted from (Tielens 2008). Fig. 6 resembles a typical SED of a star-forming galaxy between 1 and 10^4 μm, made with the CIGALE code. The mid-IR part consisting of some continuum areas and a suit of features, attributed to the PAHs, is plotted with the black line. Additionally, the red line shows the BB emission in the far-IR and sub-mm regime. The BB emission peaks at $\sim$100 μm and in longer wavelengths decreases monotonically in the Rayleigh-Jeans regime (Casey et al. 2014). In this thesis, I focus in the mid-IR spectrum of high-redshift galaxies.

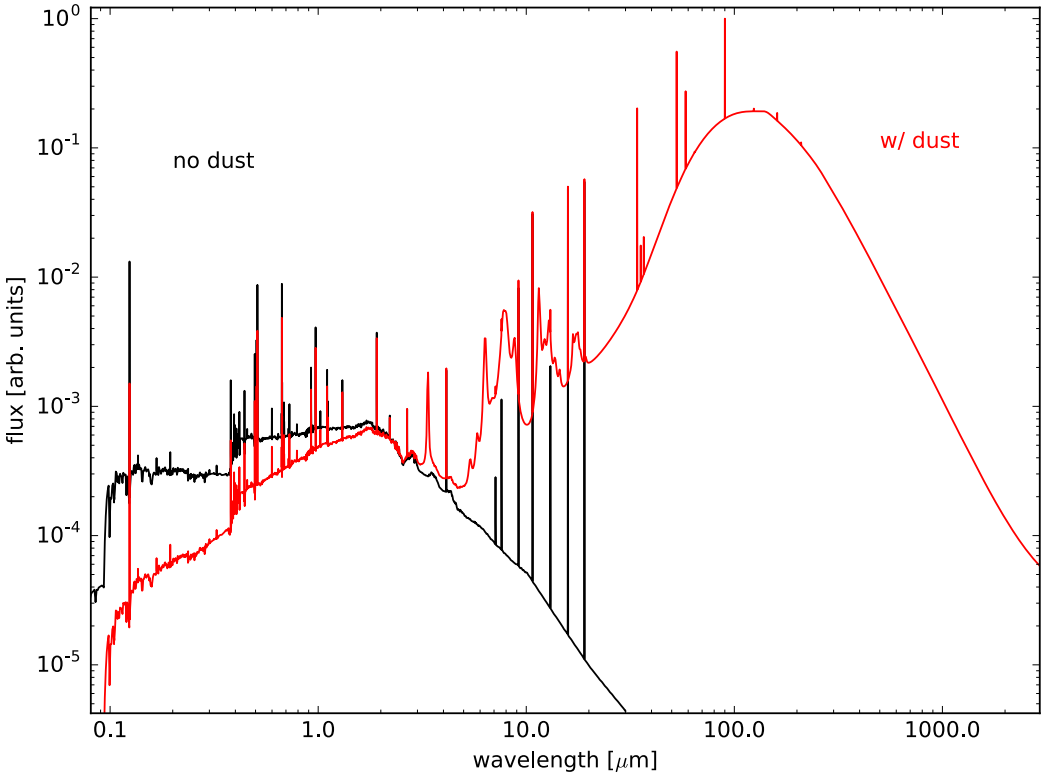

Figure 5: SEDs of the same star-forming galaxy, made with the CIGALE code, in the case that it does not contain interstellar dust (black line) and in the case that it contains interstellar dust (red line).

1.3.1 *Mid-IR spectral decomposition*

Although the ISO satellite expanded our knowledge of the mid-IR spectra of IR-luminous galaxies, Spitzer with its InfraRed Spectrograph (IRS) contributed in a more detailed investigation of the mid-IR spectra of local and high-redshift star-forming galaxies. A wide variety of spectral features that can be detected in the low-resolution IRS spectra of local galaxies, is also present in spectra of high-redshift galaxies. These features are widely used as diagnostics for the characterization of the major sources and the mechanisms that cause and dominate the IR emission in galaxies (Laurent et al. 2000; Lutz et al. 1996; Genzel et al. 1998; Peeters et al. 2004; Spoon et al. 2007). Low-resolution IRS spectra of a starburst-(SB-)dominated and an AGN-dominated source are illustrated in Fig. 7. The SB-dominated spectra have a redder slope and their most characteristic features due to PAHs

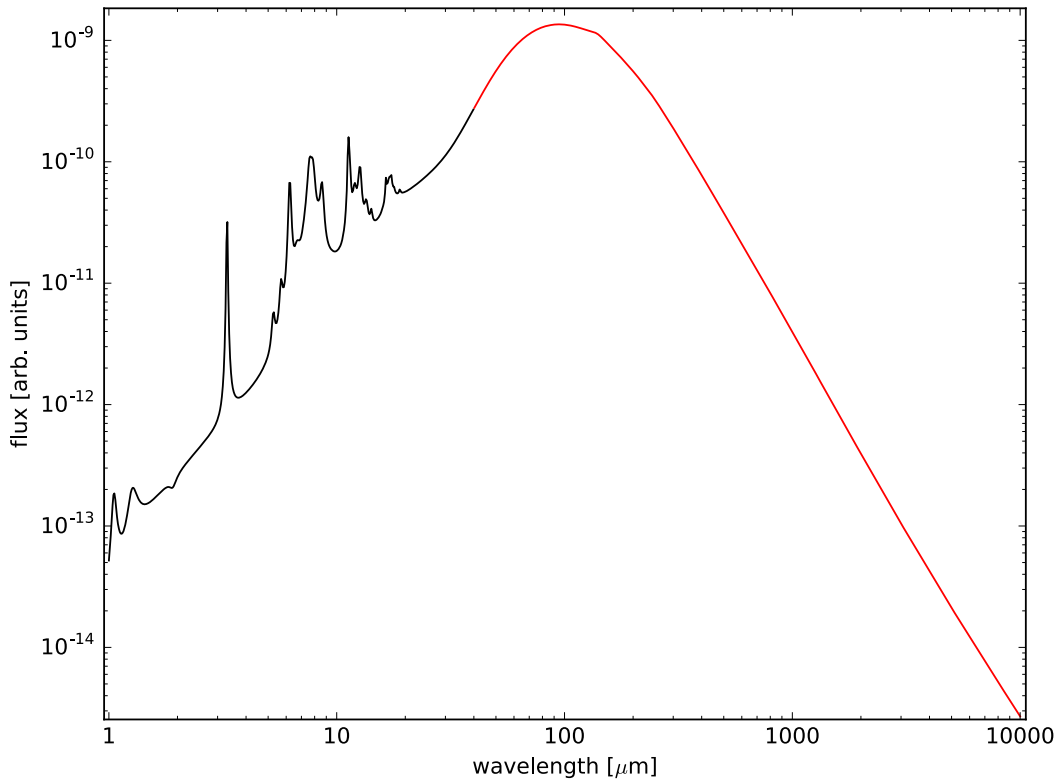

Figure 6: A typical SED of a star-forming galaxy between 1 and 10^4 μm, made with the CIGALE code. The black line corresponds to the mid-IR part, while the red line corresponds to the far-IR and sub-mm part.

are generally absent in strongly AGN-dominated galaxies, since they are destroyed by the hard AGN radiation field in UV/x-rays and the smaller photo-dissociation regions (PDRs) (Voit 1992, Weedman et al. 2005). Ionic lines can be detected in both SB- and AGN-dominated spectra.

The major features in a low-resolution IRS spectrum of galaxy are the PAH emission features at the 6.2, 7.7, 11.3 and 12.7 μm (Fig. 7a). The 6.2 and 7.7 μm features arise from C-C skeleton stretching vibrational modes of ionized PAHs, while the 11.3 μm feature arises from the solo C-H out-of-plane bending mode of neutral PAHs and the 12.7 μm feature from duo and trio C-H (Fig. 4) out-of-plane bending modes (Hony et al. 2001; Bauschlicher et al. 2008; Bauschlicher et al. 2009). A weaker PAH feature at 8.6 μm arises from C-H in-plane bending modes of ionized PAHs and is tightly correlated with the features at 6.2 and 7.7 μm (Peeters et al. 2017). The relative strengths of the features depend on the dust grain sizes, the PAHs' charge state and the intensity of the incident

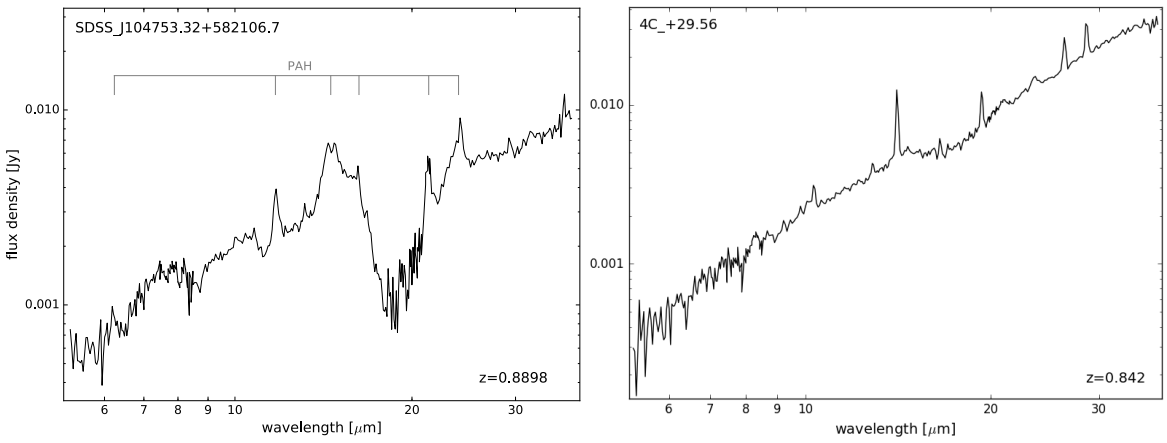

(a) (b)

Figure 7: Two IRS low-resolution spectra of high-redshift galaxies. (a) A SB-dominated source (SDSS_J104753.32+582106.7) at z = 0.8898 and (b) an AGN-dominated source (4C_+29.56), at z = 0.842. The indicated PAH features are centered at 3.3, 6.2, 7.7, 8.6, 11.3 and 12.7 μm.

radiation (Draine and Li 2001). Hence the PAH features are an important diagnostic of the dust grain properties in SB-dominated galaxies.

Observed in both local and high-redshift galaxies with recent or ongoing star formation, PAH features are widely used to probe galaxy characteristics and local physical conditions. Variations in their structure make them useful galaxy classification tools (Inami et al. 2018), while their relative strength shows the degree of ionization in their region (Tielens 2008). They have been also used as direct redshift indicators for starburst galaxies (Negrello et al. 2009). Additionally they can give information about the metallicity of their environment, since the low metal content enables hard UV photons to propagate easier and thus to destroy PAH molecules further away from the massive star forming regions (Madden et al. 2006; Smith et al. 2007; Gordon et al. 2008).

In addition to the PAH features, there is also an array of weaker features in the spectral area of 3 to 20 μm. A series of pure rotational lines of molecular hydrogen (H_2 S(7), S(5) and S(3)) and cooling lines from low-ionization elements sit between the stronger features (Sturm et al. 2000). Another line emitted from HII regions is the Brα hydrogen recombination line that traces ionizing photons

Table 1: Weak emission line parameters.

line name	**central wavelength [μm]**	**line name**	**central wavelength [μm]**
H_2(S7)	5.511.....	Brα	4.05.....
H_2(S5)	6.909.....	Fe II	5.304.....
H_2(S3)	9.665.....	S IV	10.511.....

from young stars and can thus trace the SFR of dusty galaxies. The ionized iron (Fe II) emission line at 5.304 μm can also be detected in some spectra indicating shocked gas and outflows from young stars in dusty regions of star formation (Hartigan et al. 2004). These lines though, are not always detectable because of their weakness or of low spectral resolution. The strongest absorption feature is the 9.7 μm silicate feature that sits between the prominent 7.7 and 11.3 μm PAH emission features. This absorption featured is a useful tool that helps to separate sources with buried nucleus from sources with more extended and clumpy dust regions (Spoon et al. 2007; Imanishi et al. 2007; Levenson et al. 2007). The sulfur line at 10.51 μm is often weak but it can be detected in the silicate trough. The parameters of the weak features discussed in this thesis are included in Tab. 1.

All the above mentioned features are set against a background continuum. The mid-IR spectral area (5-25 μm) is dominated by warm dust emission, arising from small dust grains heated by photons produced by young stars or through AGN accretion activity (Magdis et al. 2013). Specifically, mid-IR wavelengths in the area of 5-8 μm are dominated by the continuum emission of hot dust grains and as the emission of the dust grains rises proportionally to their temperature, emission from cooler dust grains dominates the far-IR wavelengths ($>$8 μm). As was previously mentioned, the integrated emission in the area of 8-1,000 μm is called infrared luminosity L_{IR}. In galaxies highly obscured by dust, L_{IR} approximates well the bolometric luminosity and can be an important tracer of the SFR (Kennicutt 1998).

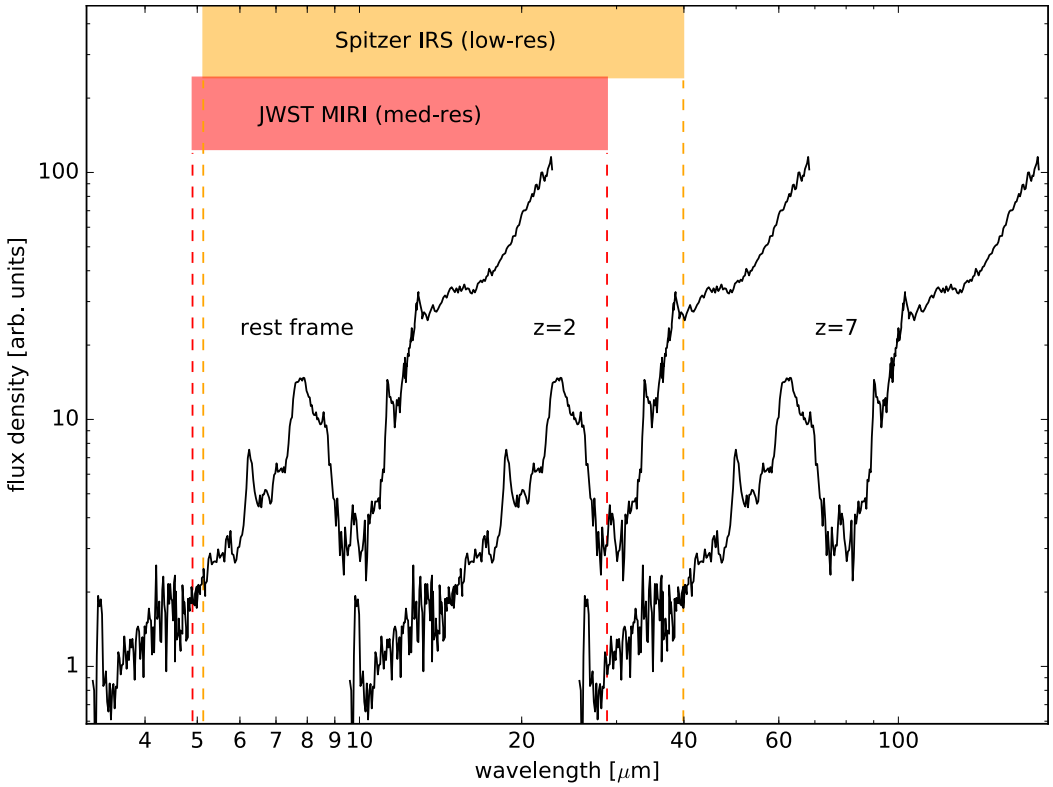

Figure 8: The IRS spectrum of the source IRAS_F14537+1950 with strong PAH features in the rest frame and also in redshifts 2 and 7 assuming exposure times during the observations that provide the same flux density in these redshifts. The wavelength coverage of the Spitzer's IRS and the James Webb Space Telescope's Mid-InfraRed Instrument (MIRI) are also illustrated with the orange and red shaded area respectively.

1.4 THE 3.3 μm PAH FEATURE

The 3.3 μm PAH feature arises from the C-H stretching mode of neutral PAHs and is correlated with the 11.3 μm (Peeters et al. 2017). Observations of local LIRGs have shown that in the spectral range of 2.5-5 μm, the 3.3 μm PAH emission line is the most prominent feature (Inami et al. 2018). However, in high-redshift systems, due to the limited sensitivity of the IRS, it is only observed in a few very luminous sources.

The forthcoming James Webb Space Telescope (JWST) with its Mid-InfRared Instrument (MIRI) will be able to cover mid-IR wavelengths from 4.9 to 28.8 μm, using its Medium-Resolution Spec-

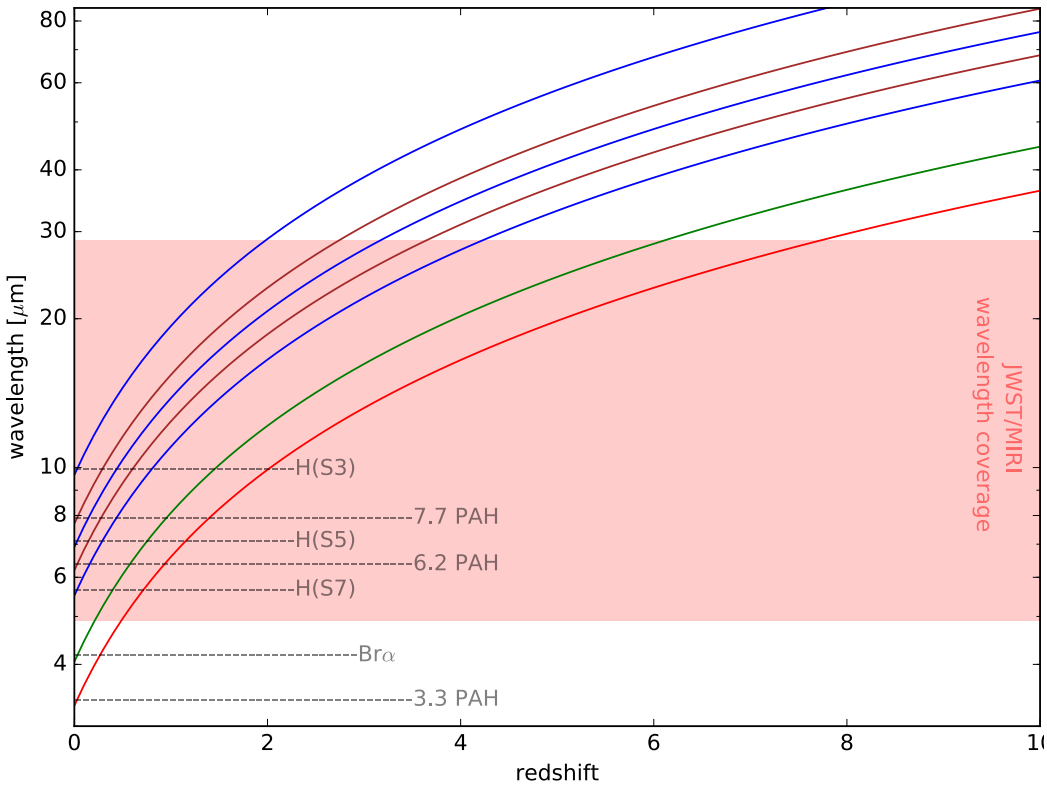

Figure 9: The different wavelength values that several mid-IR features can be observed as a function of redshift. The red shaded area corresponds to the wavelength coverage of the MIRI.

trometer (MRS) with resolution, R$\sim$1,500-3,000. Its ability to provide simultaneous spatial and spectral information with high sensitivity, will make, in principle, the detection of the 3.3 μm PAH feature possible up to redshift $\sim$8. Fig. 8 shows the wavelength coverage of the MIRI compared to the IRS coverage with an example of a SB-dominated galaxy plotted in several wavelengths. Moreover, Fig. 9 highlights that the 3.3 μm PAH will be the only observable PAH feature at redshift higher than 3.5. In this project I calculate the median spectrum of all the PAH-dominated high-redshift sources, observed by the IRS and cover the 3.3 μm band. The aim of the project is to recover the 3.3 μm PAH feature and characterize its emission.

1.5 THESIS LAYOUT

In the first chapter, the importance of observing galaxies in the IR part of the electromagnetic spectrum is emphasized, followed by an overview of the contribution of the dust in the observed IR radiation. A decomposition of the mid-IR spectrum is also presented with mentioning the most important spectral features of IR-luminous galaxies. Later, there is an extended analysis to the PAH features and especially to the 3.3 μm PAH feature and the motivation to investigate and characterize its emission.

The criteria for selecting the sources used in this project are presented in Chapter 2, followed by the steps of the processing before the spectra been used for the method to obtain the results of the project. The Spitzer Space Telescope was also discussed, with reference to some basic information about its main parts, including its cameras and spectrograph. In the same chapter are also presented the AGN-SB selection criteria that used to separate the sample into two sub-samples.

The analysis and the results are presented in Chapter 3, while Chapter 4 includes the conclusions and discussion of the results and their utility to the future observations. In the appendices of Chapter 5 are included all the photometric data as well as the spectra used in the project.

2

SAMPLE SELECTION AND PROCESSING

The aim of this project is to collect and analyze all high-redshift galaxies with available Spitzer/IRS spectra which sample the 3.3 μm PAH range and investigate possible relations between their IR spectral features and their physical properties. The comparison of my results, with corresponding analysis in local galaxies can help to improve our knowledge about galaxy evolution and the changes in the star formation efficiency in different cosmic epochs.

2.1 SPECTROSCOPY AND PHOTOMETRY WITH SPITZER

The Spitzer Space Telescope is a part of the NASA's Great Observatories Program. A program that consists of four space telescopes that observe the universe in different bands. Spitzer was built to observe in IR wavelengths, while the Hubble Space Telescope (HST) in optical, the Compton Gamma-Ray Observatory (CGRO) in gamma-rays and the Chandra X-Ray Observatory (CXO) in x-rays. Following ISO and IRAS, Spitzer is the observatory with the highest sensitivity, providing for the first time very efficient IR spectroscopy, with low- to moderate-resolution.

Since Spitzer was designed to observe IR photons, in order to avoid contamination from its own thermal radiation, it has to be cooled. At the same time, the telescope's temperature has to be low enough, in order to be able to detect radiation coming from relatively cold objects. Liquid helium was the coolant, that was keeping the temperature of the telescope mirror and the focal plane at about

5 Kelvins. The mission was launched in 25 August 2003, but its cryogenic era ended in 15 May 2009, when it ran out of helium. Since then it is in a warm era where only some of its instruments are still in operation. Its telescope is a Ritchey-Chretien with 0.85m diameter and focal length of 10.2m.

2.1.1 *The InfraRed Spectrograph (IRS)*

Spitzer is equipped with a spectrometer called IRS. It is one of the 3 instruments in the same focal plane and consists of four individual modules named Sort Low (SL), Sort High (SH), Long Low (LL) and Long High (LH). They cover a wavelength range from 5.2 to 38 microns with low (R$\sim$60-130) and moderate (R$\sim$600) spectral resolution.

Table 2: InfraRed Spectrograph (IRS) module characteristics

Module	**Wavelength Range [μm]**	**Slit Dimensions [arcsec]**	**Spectral Resolution [$\lambda/\Delta\lambda$]**
SL2	5.13 – 7.60	3.6 $\times$ 57	60 - 127
SL1	7.46 - 14.29	3.7 $\times$ 57	61 - 120
LL2	13.9 – 21.27	10.5 $\times$ 168	57 - 126
LL1	19.91 - 39.90	10.7 $\times$ 168	58 - 112
SH	9.89 - 19.51	4.7 $\times$ 11.3	$\sim$ 600
LH	18.83 - 37.14	11.1 $\times$ 22.3	$\sim$ 600

2.1.2 *The InfraRed Array Camera (IRAC)*

The first Spitzer's camera performs photometry using four individual filters, centered at 3.6μm, 4.5μm, 5.8μm and 8μm respectively. IRAC has two detectors enabling simultaneous 5.2 $\times$ 5.2

arcmin images at two filters. The IRAC pixel size is 1.2 arcsec, with a point spread function (PSF) $\sim$1.8 arcsec and the available circular apertures have 3.8 and 5.8 arcsec diameter, respectively.

Table 3: InfraRed Array Camera (IRAC) channel characteristics

Channel	**Wavelength Range [μm]**	**Field of View [arcmin]**	**Detector**
1	3.19–3.94	5.2 $\times$ 5.2	256 $\times$ 256 InSb
2	4.00–5.02	5.2 $\times$ 5.2	256 $\times$ 256 InSb
3	4.98–6.41	5.2 $\times$ 5.2	256 $\times$ 256 Si:As
4	6.45–9.34	5.2 $\times$ 5.2	256 $\times$ 256 Si:As

2.1.3 *The Multi-band Imaging Photometer for Spitzer (MIPS)*

The other camera is called MIPS and performs imaging in broad spectral bands, centered at 24μm, 70μm, and 160μm respectively.

Table 4: Multi-band Imaging Photometer for Spitzer (MIPS) characteristics

Band Identification	**Wavelength Range [μm]**	**Field of View [arcmin]**	**Detector Array**
24 μm	21.5–26.2	5.4 $\times$ 5.4	128 $\times$ 128 Si:As
70 μm	62.5-81.5	5.2 $\times$ 5.2	32 $\times$ 32 Ge:Ga
160 μm	139.5–174.5	5.3 $\times$ 0.5	2 $\times$ 20 Stressed Ge:Ga

Combining these three instruments, Spitzer provides broadband imaging and low spectral resolution spectroscopy contributing to the study of several astrophysical problems from our solar system to the dawn of the Universe.

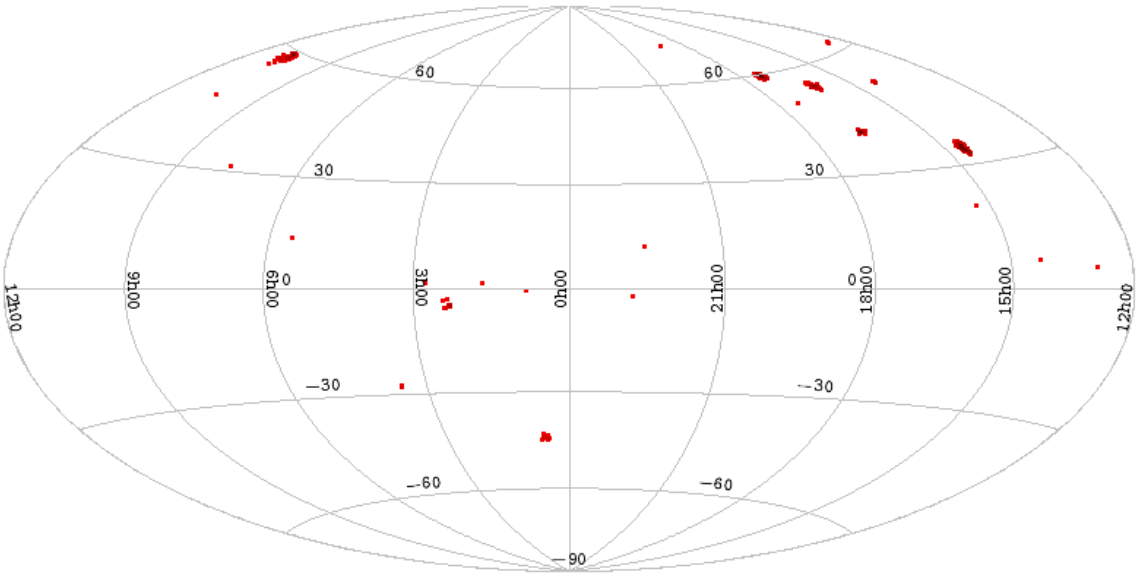

Figure 10: Sky plot of the 324 sources in our sample. It is clear that the sources are from several fields and some of them are dispersed.

2.2 SAMPLE SELECTION

During Spitzer's cryogenic mission the IRS collected spectra of about 14000 individual targets. The Cornell Atlas of Spitzer/IRS Sources[1] (CASSIS) (Lebouteiller et al. 2011) provides 13000 calibrated spectroscopic observations obtained with the SL and LL low-resolution modules. Since I am interested in PAH features and especially in the 3.3 μm PAH emission line, I need to select sources with redshift greater than 0.6, so that the 3.3 PAH is found within the spectral part covered by the SL2 module or the other modules with longer wavelength ranges. This lower redshift limit comes from the following equation,

$$5.13 < 3.3(1+z) \Rightarrow z \geq 0.56, \tag{1}$$

where 3.3 is the wavelength (in microns) that the PAH feature is expected to be emitted and 5.13 is the lower wavelength limit of the IRS (SL2 module, Tab. 2).

1 http://cassis.sirtf.com/

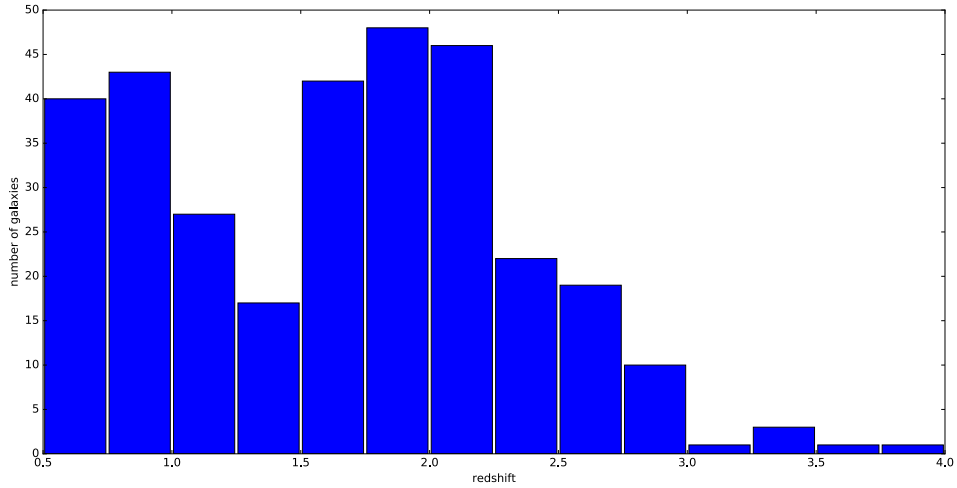

Figure 11: Histogram of the number of sources per redshift bin in our sample. The bins have width equal to 0.25.

By checking the sources provided by the CASSIS, 324 spectra, that are located in various deep fields across the sky (Fig. 10), satisfied the criterion of the equation 1 and are included in the sample. The Infrared Database of Extragalactic Observables from Spitzer[2] (IDEOS) provides a valid redshift value for every spectrum (Hernán-Caballero et al. 2016). The redshift values were found after associating the redshifts from optical counterparts of the NASA's Extragalactic Database (NED) with accurate values from the IRS spectra, measured by calculating a maximum combined pseudo-likelihood method (MCPL). In the cases where the redshift can be estimated from the IRS spectrum and the NED value is photometric, the IRS value is preferred.

The lowest redshift value, in the sample, is 0.60236, while the highest is 4.27. Most of the sources are at redshifts from 1.5 to 2.25 (Fig. 11). Every source in the IDEOS database is followed by a name that corresponds to the redshift verification status. If d = $(z_{IRS} - z_{NED})/(1 + z_{NED})$ and $\delta = |\mathrm{d}|$ indicates the accuracy of the MCPL redshift, when the two redshift values are in an agreement like $\delta < 0.005$, the redshift value is considered as "confirmed". In order of diminishing confidence, sources are also identified as "verified", "probable", "robust", "unchallenged" and "uncertain", respectively

2 http://ideos.astro.cornell.edu/redshifts.html

(Lebouteiller et al. 2011). Table 5 in the Appendices (Chapter 5) includes all the basic information for the sources in our sample.

From the 322 sources in the sample, there is available photometry, obtained by Spitzer's InraRed Array Camera (IRAC), for 292 sources. However, only 221 sources ($\sim$74%) have been observed in all 4 IRAC channels. I rejected 5 of these sources because their photometric data do not match to their spectroscopic data. The flux in the spectroscopic data is lower than the photometric flux for all these 5 sources. This is probably due to the incorrect placement of the slit on the source and this results in a part of the total flux of the source being lost. The IRAC photometry is provided by the Spitzer Enhanced Imaging Products (SEIP), Cryogenic Release version 3.0. This is a combination of images and tables with data of Spitzer's cryogenic mission, provided by the Spitzer Science Center (SSC) and the Infrared Science Archive[3] (IRSA). The photometric data used in this project have been extracted with both 3.8 and 5.8 arcsec apertures. The 221 sources observed in all four IRAC channels are included in Tab. 6 of the Appendices (Chapter 5). Consequently, as was mentioned above, all the spectroscopic and photometric data used for this thesis are obtained by Spitzer.

2.3 SPECTRA PROCESSING

The CASSIS database provides galaxy spectra that are extracted using two different methods, the tapered column and the optimal extracted spectra. The optimal extracted spectra provide the best signal-to-noise ratio (S/N) for faint point-like sources, since they fit and scale the PSF to the source's spatial profile and are the most suitable for our research. The optimal extracted spectrum of the source S2 is presented in Fig. 12. The parts of the spectrum observed with different low resolution modules of the IRS are denoted with different colors.

3 http://irsa.ipac.caltech.edu/frontpage/

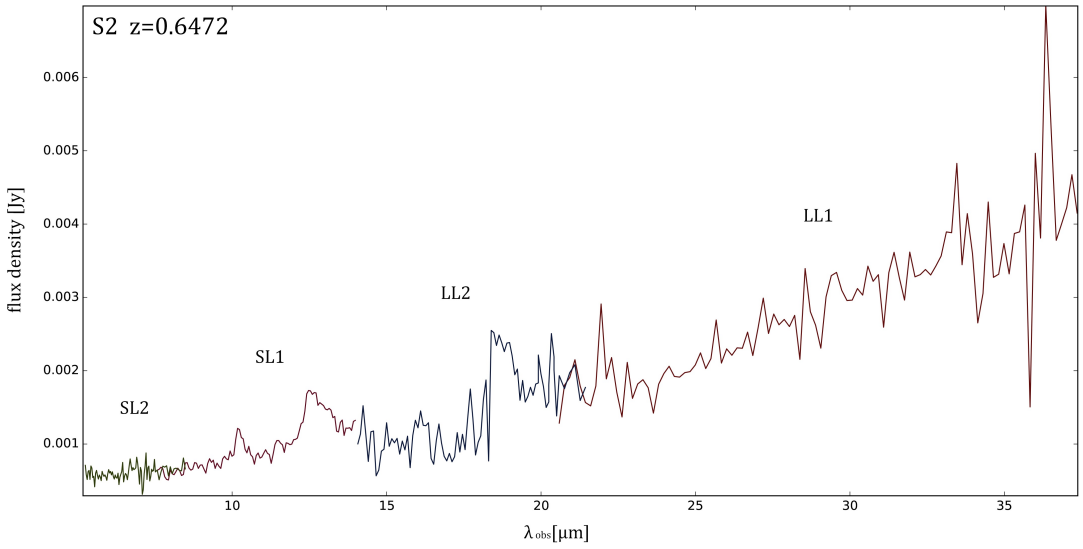

Figure 12: The IRS spectrum of the source S2 with redshift 0.6472. With different colors are illustrated the parts of the spectrum observed with the four low resolution modules.

After collecting the spectra and creating our sample, I firstly shift them to the rest frame by dividing the wavelength by the factor (1 + z), where z is the redshift of each source. I simultaneously divide the flux density (per frequency) by the same factor, in order to conserve the luminosity of the source.

Thereafter, I normalize every individual spectrum by using the median flux value in the range 3.55 to 3.65 μm. Since there are no known spectral features in this range, I am certain that I normalize to the continuum value. At the same time it is close to the weak 3.3 μm PAH that I am interested in. So I avoid this feature to be diluted in the continuum of the brightest galaxies during the stacking method I am using afterwards.

The spectral resolution of the IRS is not constant as a function of wavelength (Fig. 13). Thus, the step $\Delta\lambda$ from pixel to pixel is also changing. The final part of the spectra processing method is the interpolation. By performing linear interpolation I register the spectra of individual galaxies onto a wavelength grid, set to have a constant step $\Delta\lambda = 0.01\mu$m. Every step of the method that leads to the interpolation of the spectra is illustrated in Fig. 14. The processing method for the flux-error is the

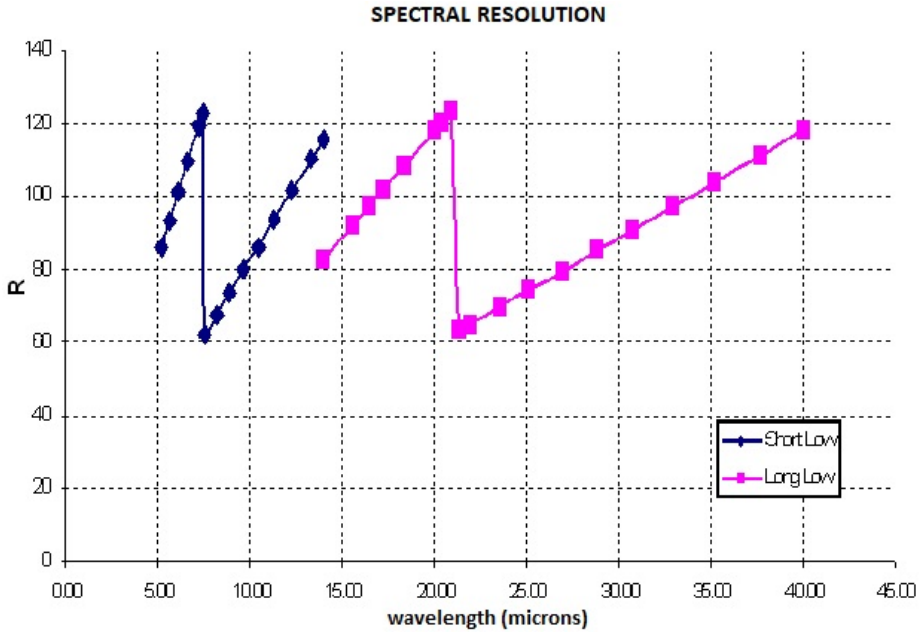

Figure 13: The spectral resolution of the IRS as a function of wavelength. The SL and LL modules are illustrated with blue and purple color respectively.

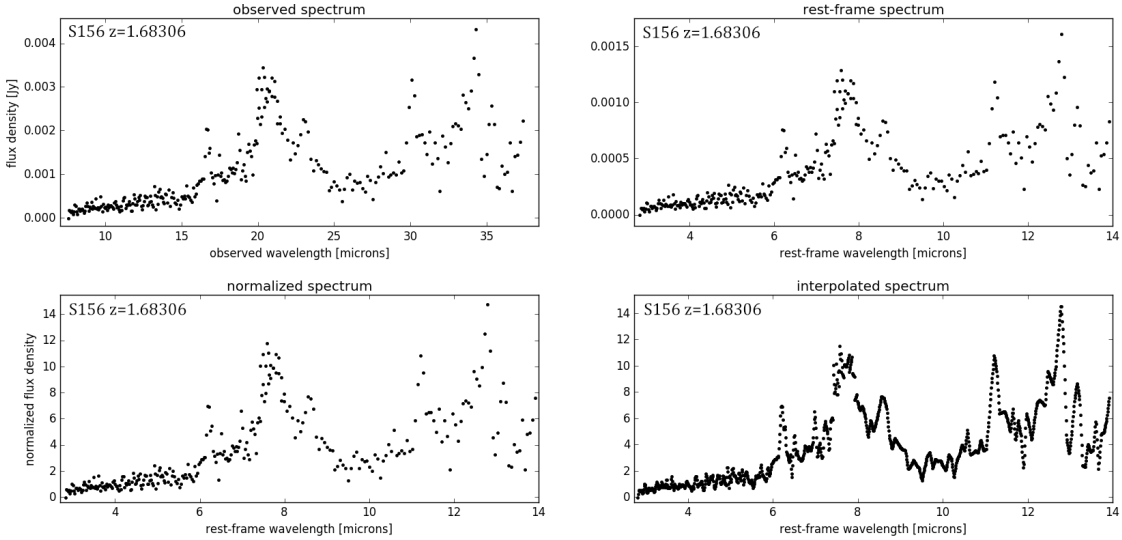

Figure 14: An example of the processing steps to the optimal extracted spectra in the sample. Firstly I shift the observed spectrum to the rest frame, then I normalize it and finally I interpolate it. In this example the spectrum of the source S156 with redshift 1.68306 is presented.

same as for the flux of the spectra. So, before stacking the spectra, I firstly shift, normalize and also interpolate the flux-error for every individual spectrum.

2.4 AGN AND SB SELECTION CRITERIA

Since the high-redshift sources we wish to study are faint, it is challenging to analyze their mid-IR spectral properties one by one. We can, however, separate them in a physically reasonable manner and examine the median spectra of each group, which will have, by definition, a higher S/N. One first approach is to study SB- and AGN-dominated sources, using criteria for identifying them mid-IR color-color diagrams.

Such criteria, were firstly introduced by Lacy et al. 2004, Lacy et al. 2007 and Stern et al. 2005, using IRAC photometric data and creating color-color diagrams for AGN selection. A revised IRAC criterion was later defined by Donley et al. 2012 and was able to improve some weaknesses of the former methods. This is the method used in this project in order to separate the AGN and SB sources in the sample.

The data that are needed for this method are the photometric measurements performed by the four IRAC channels. Sources with no available photometry in one or more IRAC channels, are excluded. By using the available photometric data (Tab. 6), a color-color diagram is created as is depicted in Fig. 15. The Donley et al. 2012 selection criteria used for creating this diagram are the following,

$$X = log_{10}\left(\frac{f_{5.8\mu m}}{f_{3.6\mu m}}\right), \qquad Y = log_{10}\left(\frac{f_{8.0\mu m}}{f_{4.5\mu m}}\right) \tag{2}$$

$$\begin{aligned} X \geq 0.08 \ \ and \ \ Y \geq 0.15 \\ and \ \ Y \geq (1.21 \times X) - 0.27 \ \ and \ \ Y \leq (1.21 \times X) + 0.27 \\ and \ \ f_{4.5\mu m} > f_{3.6\mu m} \ \ and \ \ f_{5.8\mu m} > f_{4.5\mu m} \ \ and \ \ f_{8.0\mu m} > f_{5.8\mu m}, \end{aligned} \tag{3}$$

where f is the flux density of each IRAC channel and X, Y are defined in Eq. 2.

In order to evaluate the robustness of the selection results I decided to check the relation of the flux values for the same IRAC channels, of the two different apertures. The ratios of the flux values of the sources for the two apertures, are illustrated in Fig. 16. For most of the sources the ratio is close

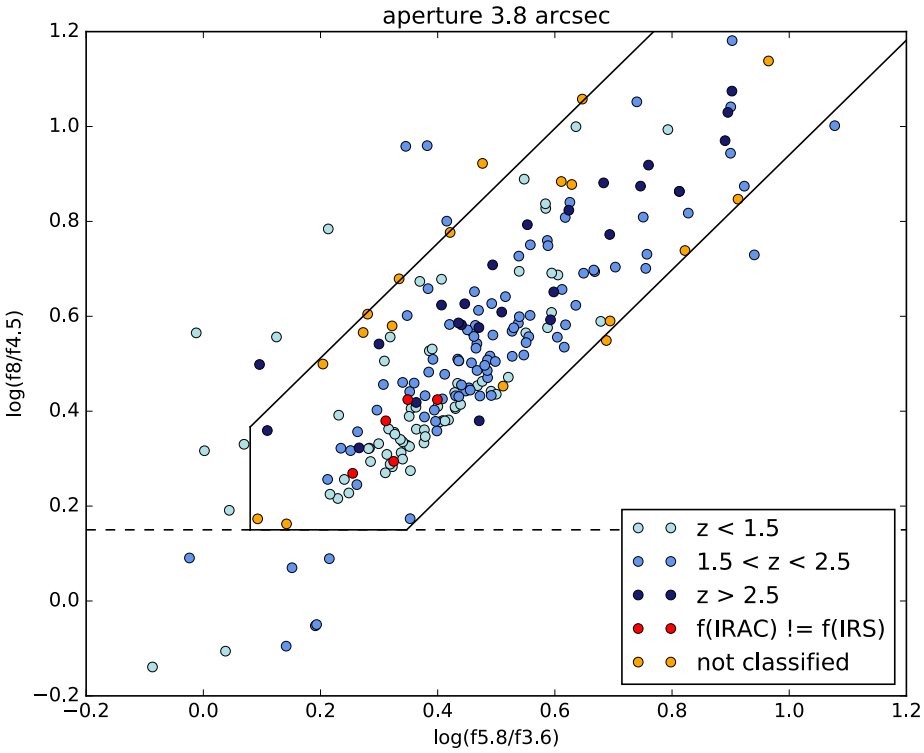

Figure 15: IRAC color-color diagram for the 3.8 arcsec aperture photomeetry. The sources are separated in three redshift bins, sources with redshift lower that 1.5 (cyan), sources with redshift between 1.5 and 2.5 (blue) and sources with redshift greater than 2.5 (dark blue). There are also some sources marked as rejected (red) and some not classified (yellow). The black dashed line indicates the $Y \geq 0.15$ cut, while the black solid lines indicate the other revised AGN selection criteria introduced by Donley et al. 2012.

to unity and a bit higher as it was expected for point-like sources and because the 5.8 arcsec aperture receives more flux than the 3.8 arcsec aperture. Nevertheless, for some sources the flux ratio deviates more than 25% from unity. For further investigation I plot the same ratio as a function of redshift as is illustrated in Fig. 17. No systematic trends are identified.

For further evaluation of the sources and for higher accuracy at their final classification as AGN or SB-dominated galaxies, I make one IRAC color-color diagram for each aperture size. The two color-color diagrams are illustrated in Fig. 18. Some sources sitting inside the box in the first diagram are moving out of it in the other and vice versa. Finally I identify 18 sources as ”not classified” and I

exclude them from the sources used for the stacking. These sources are marked with yellow circles in Fig. 15, while the rejected sources are marked with red.

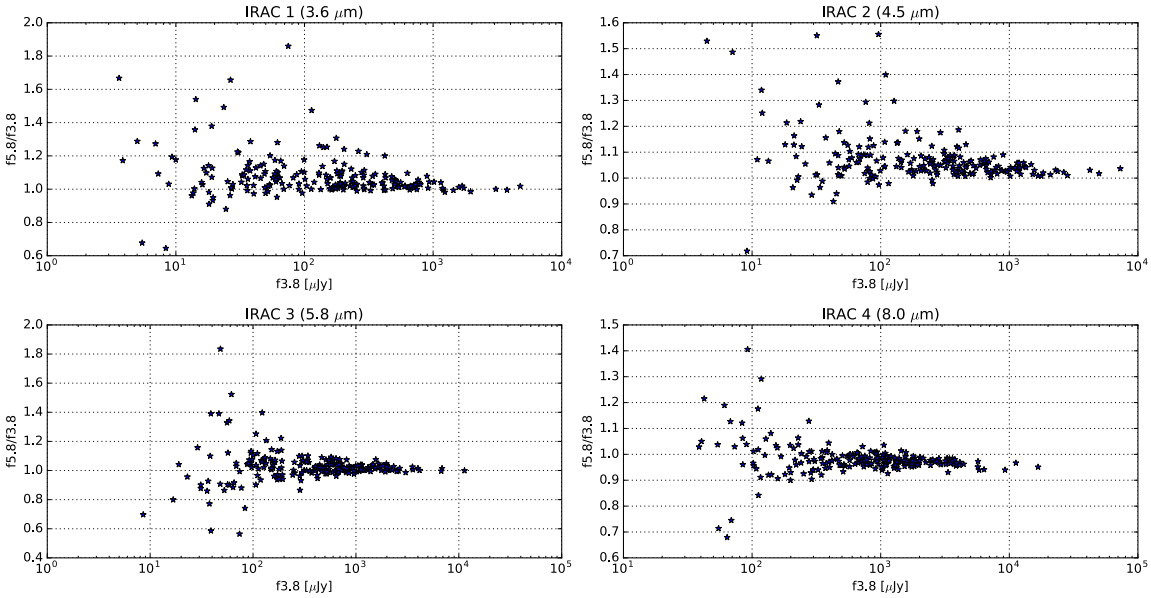

Figure 16: The ratio of the flux density measurements in the two apertures, f5.6 over f3.8, as a function of the 3.8arcsec flux density, for each one of the four IRAC filters.

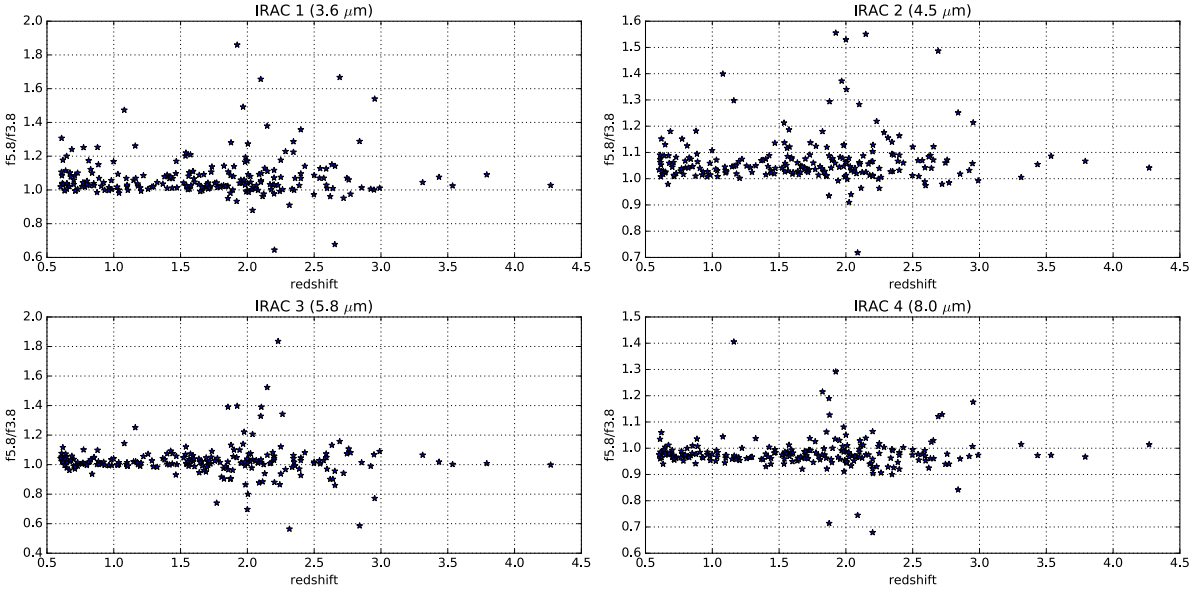

Figure 17: The ratio of the flux density measurements in the two apertures, f5.6 over f3.8, as a function of redshift, for each one of the four IRAC filters

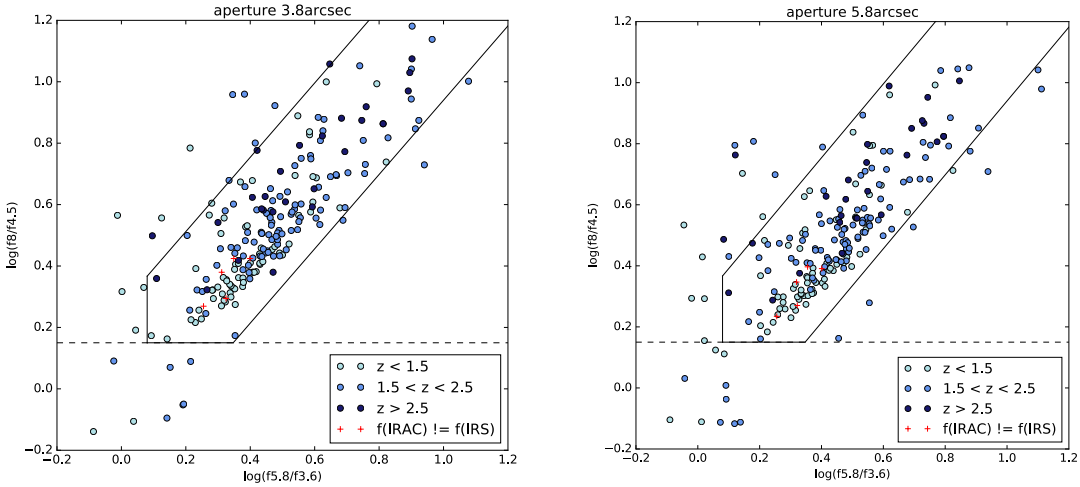

(a) IRAC color-color diagram for the 3.8 arcsec photometry.

(b) IRAC color-color diagram for the 5.8 arcsec photometry.

Figure 18: The IRAC color-color diagrams for the two different aperture size photometry. The sources are separated in three redshift bins, sources with redshift lower that 1.5 (cyan), sources with redshift between 1.5 and 2.5 (blue) and sources with redshift greater than 2.5 (dark blue). Rejected sources are marked with red crosses. The black dashed line indicates the $Y \geq 0.15$ cut, while the black solid lines indicate the other revised AGN selection criteria introduced by Donley et al. 2012

Based on the Donley et al. 2012 diagnostic, 177 sources ($\sim$80%) are classified as AGN-dominated galaxies, while 21 sources ($\sim$10%) are classified as SB-dominated galaxies. There are also 18 sources ($\sim$8%) that could not be classified because they sit close to the limits of the selection criteria (black dashed lines, Fig. 15).

3

DATA ANALYSIS AND RESULTS

3.1 STACKING ANALYSIS

The S/N of the 3.3μm PAH feature is very low, in most of the sources in my sample of high-redshift galaxies. One method that helps to recover weak or non-detected spectral features is called stacking. In this method the median spectrum of a group of galaxies with similar physical characteristics is measured. In this way, the S/N of the spectral features becomes higher, the weak lines are being recovered and it is possible to better characterize their emission.

In order to consider a spectral feature as detected, it has to be a 3-sigma detection, where sigma is the standard deviation of the local continuum near the feature. When the median spectrum is calculated, because the noise is random, the noise in the continuum decreases, while weak features, where positive signal is expected, become stronger in comparison to their local continuum.

Firstly I calculate the median spectrum of the whole sample. As is illustrated in Fig. 19 this blind-stack that contains SB-dominated galaxies with strong PAH features, AGN-dominated galaxies with PAH features on top of the power law continuum, as well as pure AGN-dominated galaxies without PAH features. Globally the spectrum seems to follow a power law. This indicates that the sample is dominated by AGNs. At the same time, the spectrum shows distinctive weak PAH emission at 6.2,

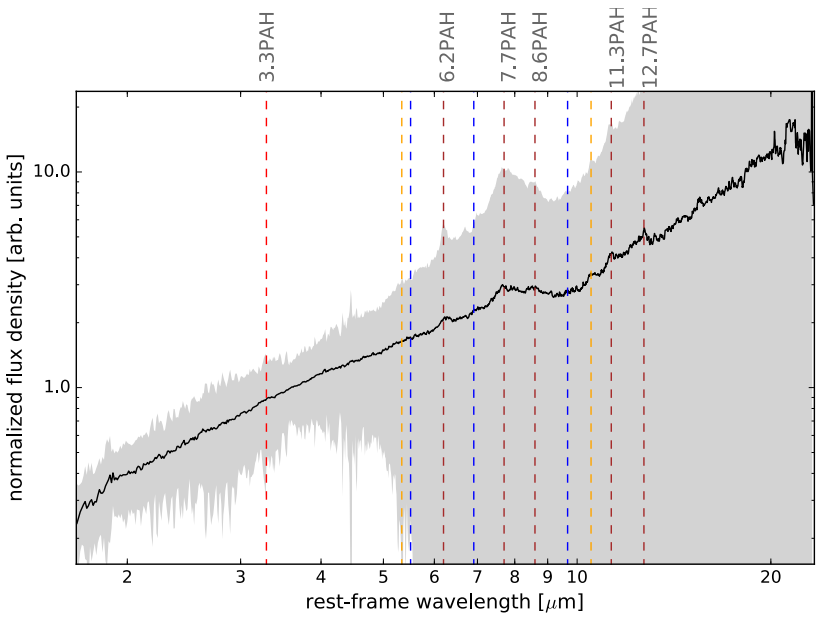

Figure 19: Median spectrum of all the 324 sources in the sample. The red and brown vertical dashed lines correspond to the wavelengths where the 3.3, 6.2, 7.7, 8.6, 11.3 and 12.7 μm PAH lines respectively, are expected to be. With different colors are indicated the 5.340 FeII (orange), the 5.511 H2 S(7), the 6.909 H2 S(5) and H2 S(3) (blue) and 10.511 SIV (yellow). The grey shaded area indicates the standard deviation of the normalized flux density.

7.7, 8.6, 11.3 and 12.7 μm. The PAH features are characteristic features of SB-dominated galaxies that are included in the sample.

3.1.1 *Selection based on Donley color-color diagram*

After calculating the median spectrum of the whole sample that provided us with some general information about the sources included in it, I used the sub-samples, created based on the selection criterion mentioned above. Therefore I calculated the median spectrum of the AGN- and SB-dominated galaxies separately and I also separated each sub-sample into three redshift bins:

$$\text{i) } z < 1.5, \quad \text{ii) } 1.5 \leq z < 2.5 \quad \text{and} \quad \text{iii) } z \geq 2.5$$

AGN-dominated sources

The three median spectra for the AGN-dominated sources are illustrated in Fig. 20. The first bin ($z \leq 1.5$), shows clear detection of 6.2, 7.7, 8.6, 11.3 and 12.7 μm PAH features. However the 3.3 μm PAH feature is not detected. For the second bin ($1.5 < z \leq 2.5$) the 6.2 is at 2σ level, so it is considered as not detected. Finally, for the last bin ($z > 2.5$) the median spectrum seems to follow a power law without any PAH or other feature emission.

I set the range of 3.00-3.23 and 3.37-3.60 μm as the local continuum of the 3.3 μm feature and the areas of 5.81-5.95 and 6.45-6.75 μm as the local continuum for the 6.2 μm feature respectively. From Inami et al. 2018 and Smith et al. 2007, I set a fixed Full Width at Zero Maximum (FWZM) for the two features as 0.14 and 0.5 μm, respectively, within which I measure the feature's flux.

For the non-detected features of the median spectra of the first two bins, after fitting the local continuum around the 3.3 and 6.2 μm respectively, I measure the flux in the area centered at these two wavelengths. I then subtract the continuum and add 3 times the σ of the local continuum for each occasion. Finally I calculate the ratio of the 6.2 to 3.3 μm PAH emission ($\frac{F_{6.2}}{F_{3.3}}$), which due to the non-detection of the 3.3 μm feature, is a lower limit.

For the first redshift bin ($z \leq 1.5$), the lower limit of the flux ratio of the 6.2 μm to 3.3 μm PAH emission was measured,

$$\left(\frac{F_{6.2}}{F_{3.3}}\right)_{lo.lim} = 7.52 \pm 2.96 \tag{4}$$

Similarly, for the second redshift bin ($1.5 < z \leq 2.5$), the flux ratio was respectively measured,

$$\left(\frac{F_{6.2}}{F_{3.3}}\right)_{lo.lim} = 16.55 \pm 6.05 \tag{5}$$

The uncertainty of the flux ratio was calculated by propagating the flux errors and adding them in quadrature. For the last bin ($z > 2.5$), it is obvious that no PAH emission is visible.

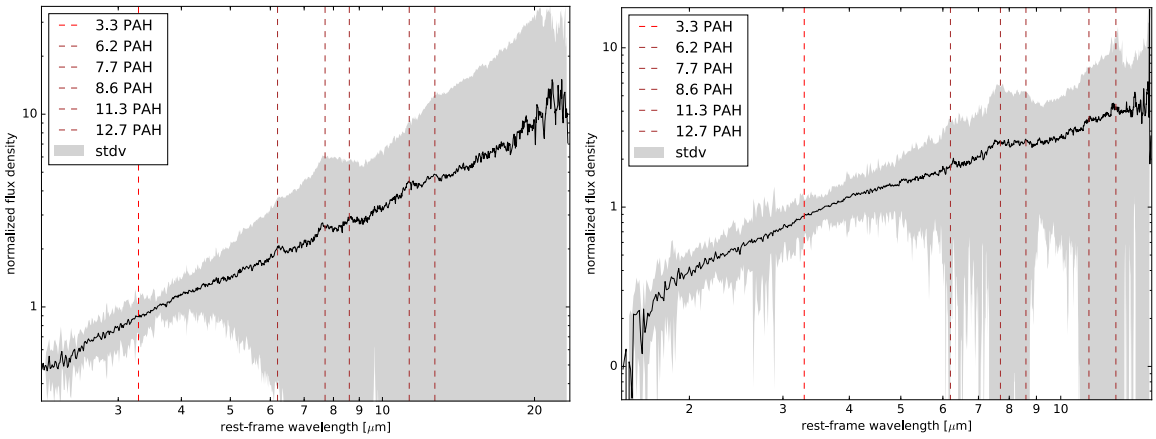

(a) Median spectrum of 62 AGN-dominated sources with $z \leq 1.5$

(b) Median spectrum of 85 AGN-dominated sources with $1.5 < z \leq 2.5$

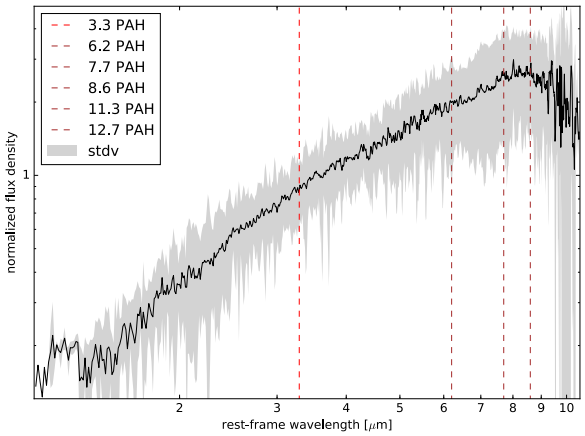

(c) Median spectrum of 24 AGN-dominated sources with $z > 2.5$

Figure 20: Median spectra of the AGN-dominated sources, separated into three different redshift bins. The grey shaded area indicates the standard deviation of the normalized flux density and the vertical dashed lines correspond to the wavelengths where the 3.3, 6.2, 7.7, 8.6, 11.3 and 12.7 μm PAH lines are expected to be.

SB-dominated sources

Fig. 21 presents the median spectra of the SB-dominated sources. It wasn't possible to calculate a median spectrum for redshift higher than 2.5, because there was only one SB-dominated source.

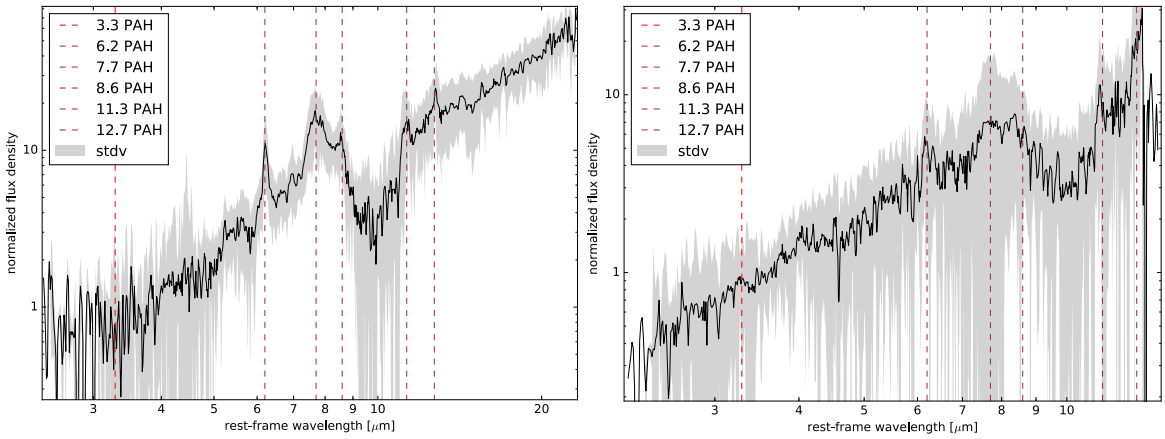

(a) Median spectrum of 8 SB-dominated sources with $z \leq 1.5$

(b) Median spectrum of 12 SB-dominated sources with $1.5 < z \leq 2.5$

Figure 21: Median spectra of the SB-dominated sources, separated into two redshift bins. The grey shaded area indicates the standard deviation of the normalized flux density and the vertical dashed lines correspond to the wavelengths where the 3.3, 6.2, 7.7, 8.6, 11.3 and 12.7 μm PAH lines are expected to be.

The median spectrum of $z \leq 1.5$ has strong PAH features, but the 3.3 μm PAH is again not detected. Similarly, in the median spectrum of $1.5 < z \leq 2.5$ neither the 3.3, nor the 6.2 μm PAH are detected.

Following the same procedure as for the analysis of the AGN-dominated sources, for the first redshift bin ($z \leq 1.5$), the lower limit of the flux ratio of the 6.2 μm to 3.3 μm PAH emission was measured,

$$\left(\frac{F_{6.2}}{F_{3.3}}\right)_{lo.lim} = 13.17 \pm 4.43 \tag{6}$$

Similarly, for the second redshift bin ($1.5 < z \leq 2.5$), the flux ratio was respectively measured,

$$\left(\frac{F_{6.2}}{F_{3.3}}\right)_{lo.lim} = 25.70 \pm 8.28 \tag{7}$$

3.1.2 *Manual selection of SB-dominated sources*

Not being able to detect the 3.3 μm PAH feature by stacking the AGN- and SB-dominated sources based on the Donley et al. 2012 criterion, led us to use a manual way to select SB-dominated sources to stack. From the SB-dominated sources classified by the Donley et al. 2012 criterion, only 26% of them display strong 6.2 and 7.7 μm PAH features (see Appendix). Hence, I decided to identify, by visual inspection, in which spectra these features are strong. These sources, 19 in total, are expected to be SB-dominated galaxies and are also expected to have in principle 3.3 μm PAH feature emission. Their redshift ranges from 0.636 to 1.911 with their average redshift being 1.274. From these sources, 13 are at redshift lower than 1.5, while the others at greater redshift than 1.5.

Their median spectrum which is illustrated in Fig. 22 clearly shows strong 6.2, 7.7, 11.3 and 12.7 μm PAH features as it was expected and the 3.3 μm PAH feature seems to be present. After fitting and subtracting the local continuum of the 3.3 and 6.2 μm PAH features, I measure their flux and also their flux ratio. The local continuum fitting is illustrated in Fig. 22 with red continuum lines. I set 3.00-3.23 μm and 3.37-3.60 μm as the local continuum of the 3.3 μm feature, assuming that the water ice absorption feature at 3.05 μm and the carbonaceous dust absorption feature at 3.4 μm are not detected. For the 6.2 μm feature, I set 5.81-5.95 μm and 6.45-6.75 μm as the local continuum respectively.

Since the 3.3 PAH feature is not a 3σ detection, we measure the lower limit of the flux ratio of the 6.2 μm to 3.3 μm PAH emission,

$$\left(\frac{F_{6.2}}{F_{3.3}}\right)_{lo.lim} = 20.15 \pm 4.14 \quad (8)$$

The uncertainty of the flux ratio was again calculated by propagating the flux errors of the two features and adding them in quadrature. This result agrees with the corresponding results of (Inami et al. 2018) for local LIRGs, where the ratio is 19.04 $\pm$ 1.62, but my ratio is the lower limit. For local galaxies with both star-forming activity and AGN, due to the detection of the NeII line, and

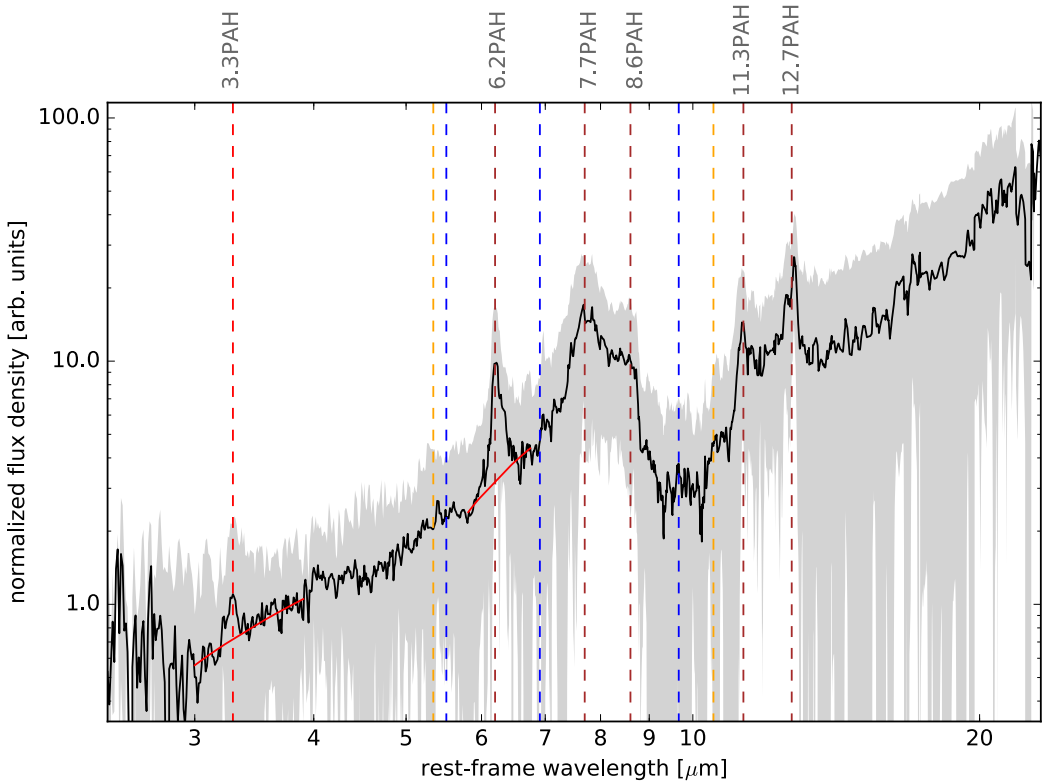

Figure 22: Median spectrum of 19 SB-dominated sources selected by visual inspection. The red and brown vertical dashed lines correspond to the wavelengths where the 3.3, 6.2, 7.7, 8.6, 11.3 and 12.7 μm PAH lines respectively, are expected to be. With different colors are indicated the 5.340 FeII (orange), the 5.511 H2 S(7), the 6.909 H2 S(5) and H2 S(3) (blue) and 10.511 SIV (yellow). The gray shaded area shows the standard deviation of the normalized flux density of the selected sources. The fitting of the local continuum of the 3.3 and 6.2 μm PAH features are denoted with red lines.

with average redshift equal to 0.85, Dasyra et al. 2009 measured the same ratio equal to 2.22. This value is lower than what is typically seen for local ULIRGs (Imanishi, Dudley and Maloney 2006; Imanishi et al. 2008) and may result when the emission from neutral PAHs is stronger than that from the ionized PAHs.

4

DISCUSSION AND CONCLUSIONS

Following several past studies which investigated the emission of the 3.3 μm PAH feature, using data of local galaxies from space telescopes such as AKARI and Spitzer (Imanishi et al. 2010; Kim et al. 2012; Inami et al. 2018), this is a work where the emission of the same feature is investigated for high-redshift, IR-luminous galaxies, using spectra obtained by Spitzer/IRS. Within this thesis I created the largest sample of high-redshift galaxies with available IRS spectra which sample the 3.3 μm PAH emission range. Based on the measurements of the 298 sources in the sample, I characterize the emission of the 3.3 μm PAH feature in order to examine their nature and properties.

Using the available IRAC photometry I separated the sources into two sub-samples, by their SB- or AGN-domination, following the Donley et al. 2012 criterion. Measuring the median spectra of the galaxies in the sub-samples, separated in three redshift-bins, I increased their S/N, in order to recover the weak 3.3 μm PAH emission. In order to derive information about the physical properties of the galaxies in the sample, I compare the 3.3 μm PAH flux with the flux of the 6.2 μm PAH .I also compare the stacked spectra from my sample with the median SEDs from Inami et al. 2018, which study a sub-sample of local LIRGs from the GOALS survay.

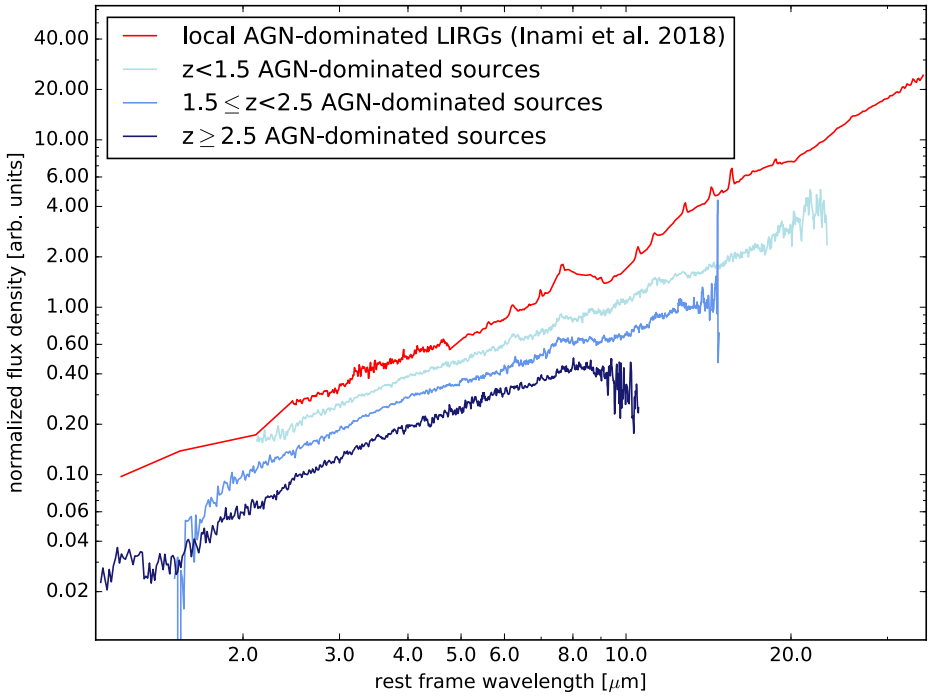

Figure 23: The median spectra of AGN-dominated sources. The stacks from the high-redshift sources in my sample are denoted by different shades of blue indicating the redshift bins. The median SED of local AGN-dominated LIRGs from Inami et al. 2018 is denoted by the red curve. The spectra fluxes are manually scaled in order to avoid big overlaps.

4.1 HIGH-REDSHIFT AGN-DOMINATED MEDIAN SPECTRA

The median spectra of the AGN-dominated sources in different redshift-bins from my sample are shown in Fig. 23. The first bin includes 62 sources, the second 85 and the third 24 sources. The median SED of local LIRGs with AGN fractions more than 60%, by Inami et al. 2018, is over-plotted in the same figure. The PAH features become weaker at higher redshifts, suggesting stronger radiation fields, originating from the AGNs, that could destruct the PAH molecules, and/or weaker surrounding starbursts. The PAH-free continuum of the third bin median spectrum provides a clear AGN signature with hard radiation fields heating the dust grains (Moorwood 1986; Imanishi and Dudley 2000) and lack of PDRs.

These results agree to the raise of the red 2.5-5 μm continuum slope that is dominated by hot dust emission from obscured AGNs (Risality et al. 2006; Sani et al. 2008). The 2.5-5 μm continuum slopes of the three redshift-bins are 0.37, 0.41 and 0.42, with ascending order of redshift. Moreover, the lower limits of the 6.2 to 3.3 μm PAH features flux ratio also increase with redshifts, being 7.52 $\pm$ 2.96 for the first bin and 16.55 $\pm$ 6.05 for the second bin, while for the local AGN-dominated LIRGs of Inami et al. 2018 is 3.98 $\pm$ 0.74. This increase could be attributed to the rise of the 2.5-5 μm continuum slope which probes the increasing AGN activity that suppresses the 3.3 μm emission flux with respect to the 6.2 μm PAH emission. Alternatively, it could be attributed to the PAH emission itself suggesting larger fraction of ionized PAH molecules with redshift. More sensitive observations with the JWST could be able to detect the weak 3.3 μm PAH emission in high-redshift AGNs and measurements of its equivalent width ($EW_{3.3PAH}$) in comparison to the $EW_{6.2PAH}$ could make us more confident about the validity of the second scenario.

4.2 HIGH-REDSHIFT SB-DOMINATED MEDIAN SPECTRA

The median spectra of the SB-dominated sources, in different redshift-bins, from my sample are shown in Figs. 24a and 24b. The first bin includes 8 sources, while the second includes 12 sources. The median SED of local LIRGs with AGN fractions less than 30%, by Inami et al. 2018, is over-plotted with the red curve and the green curve corresponds to the median SED of local LIRGs with AGN fractions more than 60%, by Inami et al. 2018.

By normalizing the median spectrum of the sources in the first redshift bin and the median SB-dominated SED by Inami et al. 2018, in order to have normalized flux density equal to unity at the peak of the 6.2 μm PAH feature, it is obvious that the spectra display very similar major PAH features (6-13 μm), but the 3.3 μm PAH feature is absent. Additionally, my 2.5-5 μm continuum area is noisy and redder than the median SB-dominated SED of Inami et al. 2018, indicating either high contribution by obscured AGN, or absence of the emission at the 3.3 μm that suggests small

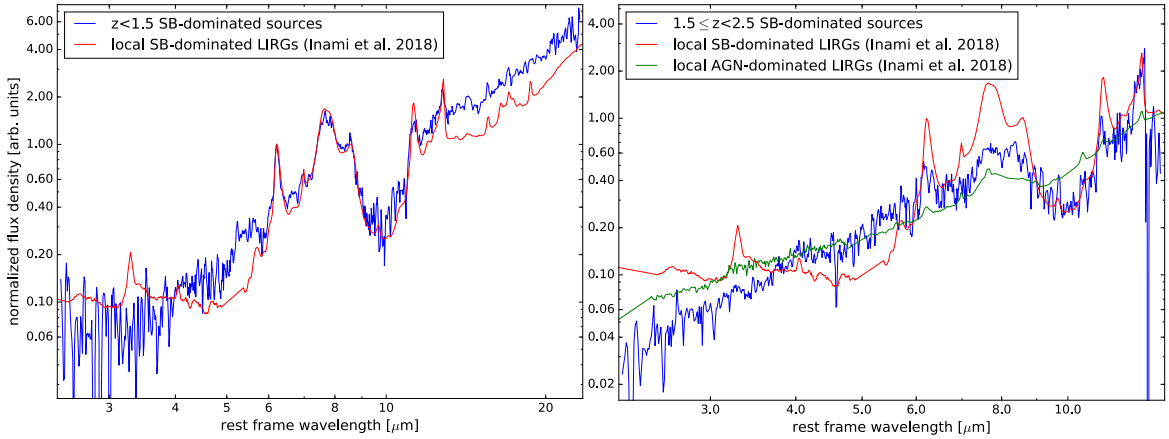

(a) (b)

Figure 24: Median spectra of the SB-dominated sources, separated into two bins, due to their redshift (blue). The SB- and AGN-dominated median SEDs by Inami et al. 2018 are denoted with the red and green curves, respectively. The spectra fluxes are manually scaled for illustrative purposes.

dust grains ionization (Draine et al. 2007b). The other emission feature that rises from neutral PAHs at 11.3 μm is distinctively detected. Smith et al. 2007 suggests that large SB magnitudes per unit volume in ULIRGs, could produce stronger radiation fields destructing more effectively the carriers of the 3.3 μm PAH emission than in local SB-dominated LIRGs. Hence, although the major PAH features suggest a SB-dominated galaxy, the 3.3 PAH feature could be weak or even absent in the SB-dominated sources of the first bin in the sample. The JWST/MIRI is expected to provide higher S/N at the area of 3 μm shedding light on the quest of the 3.3 μm feature.

While the 2.5-5 μm continuum slope of the first bin SB-dominated median spectrum is equal to 0.35, the slope of the same area in the second bin median spectrum is much redder and equal to 0.69, showing a trend of increase with redshift as was also ascertained for the AGN-dominated median spectra. However, this slope is surprisingly redder than all the slopes of the AGN-dominated median spectra. As is shown in Fig. 24b this median spectrum is more similar with the AGN-dominated median SED of Inami et al. 2018 than the SB-dominated one and has marginally detected

PAH features. Its flux mostly increases following a power law and the absorption feature at 9.7 μm typically traces the existence of buried AGN. This median spectrum could suggest strong AGN and starburst contribution in the galaxies included in this bin. Additional diagnostic criteria that take into account the $EW_{6.2PAH}$, like Inami et al. 2018 use in their research, could make the selection more robust and more sensitive observations could give more info about the characteristics of the PAH features in general.

4.3 MANUALLY SELECTED HIGH-REDSHIFT SB-DOMINATED MEDIAN SPECTRA

The median spectrum of 19 sources selected by visual inspection, discussed in paragraph 3.1.2, compared to the median SB-dominated SED by Inami et al. 2018 is shown in Fig. 25 (blue and red curve, respectively). In the area of the major PAH features, the spectra are almost identical and my stacked spectrum looks like a SB-dominated source, even though, the steep rise from 3 to 6 μm resembles an AGN-dominated system.

This result makes necessary the usage of a more systematic way of selecting the spectra. Consequently, I use the slope of the 2.5-5 μm area as a selection criterion of the already selected, by visual inspection, sources. Setting a cut at the slope of 0.35, I separate the sources, assuming strong AGN contribution at the sources with slope $\geq$0.35 and weak or no AGN contribution at those with slope $<$0.35, naming them as ”red” and ”flat” sources, respectively. Thus, by fitting the continuum in the 2.5-5 μm area, and calculating its slope, avoiding the 3.3 μm emission, 8 sources were classified as ”flat” and 11 as ”red”.

The median spectra of the two groups of sources are presented in Fig. 26 where the median SED of SB-dominated LIRGs by Inami et al. 2018 is also plotted. The stacked spectrum of the ”flat” sources matches very well with the one of the local LIRGs as is shown in Fig. 26a, hence I could conclude that the sources are SB-dominated with a very low AGN fraction. However, the 3.3 μm PAH feature

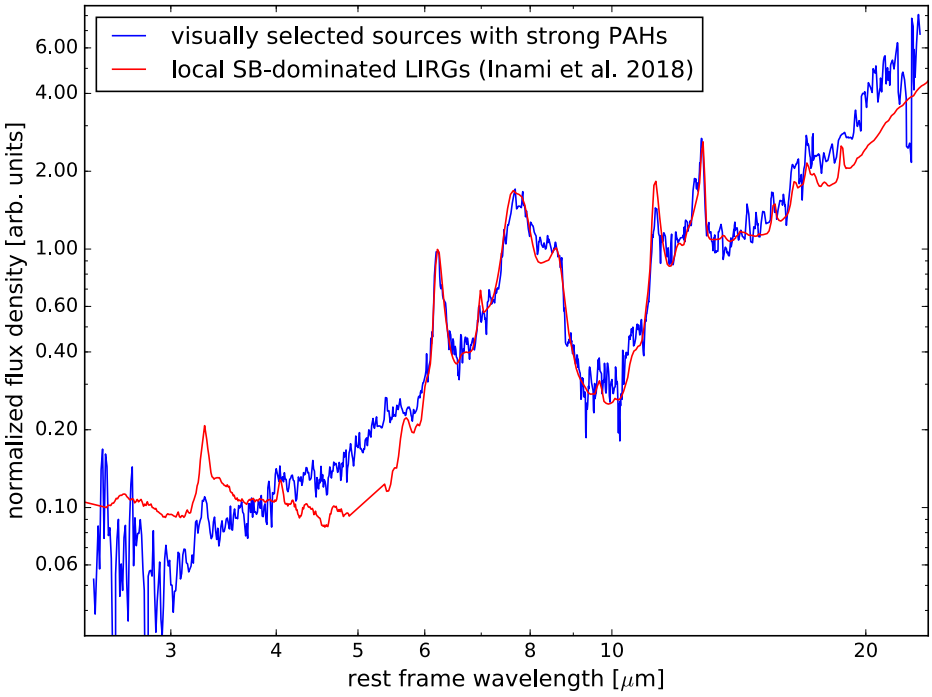

Figure 25: The median spectrum of 19 sources with strong PAH features identified by visual inspection (blue curve) and the median SED of local SB-dominated LIRGs by Inami et al. 2018 (red curve). The spectra fluxes are scaled to have flux density equal to unity at the peak of the 6.2 μm PAH feature.

is absent and the lower limit of the 6.2 to 3.3 μm flux ratio is 9.53 $\pm$ 3.03, but since the 2.5-5 μm spectral region is very noisy, this flux ratio is not consistent.

Only one of the ”flat” sources has negative slope, being contaminated by strong stellar emission and at the same time I have already avoided contribution by AGN, hence this two mechanisms are not responsible for the absence of the 3.3 μm PAH feature. If the strong noise in the 2.5-5 μm region is not the reason of the absence of the feature, the factor that may contribute at this absence, could be the existence of large SB magnitudes that produce strong radiation fields and preferentially destroy the 3.3 μm PAH carriers. A larger number of high-redshift flat sources and observations with better spectral resolution could reduce the noise in the area and verify this conclusion.

The stacked spectrum of the ”red” sources, compared to the median SED of the local SB-dominated LIRGs is presented in Fig. 26b. This stacked spectrum also shows strong major PAH features as it

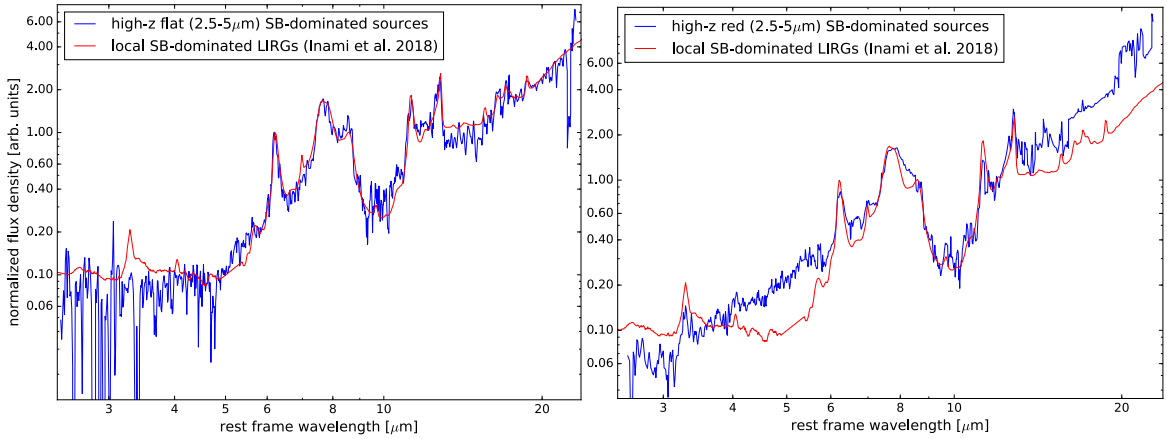

(a) (b)

Figure 26: The SB-dominated median spectra, (a) of the flat 2.5-5 μm continuum sources and (b) of the red 2.5-5 μm continuum sources. The SB-dominated median SED by Inami et al. 2018 is denoted with the red curve. Both the spectra are normalized in order to have normalized flux density equal to unity at the peak of the 6.2 μm PAH feature.

was expected. However, these features seem to be weaker compared to the underlying continuum emission. The red slope of the 3-6 μm continuum indicates strong AGN contribution. However the lower limit of the 6.2 to 3.3 μm flux ratio is equal to 13.34 ± 3.29 and lower than the flux ratio of the median spectrum of the local SB-dominated LIRGS (19.04 ± 1.62) and with AGN fraction $<30\%$.

It is unclear how both strong AGN and SB activities contribute to this median spectrum and how the neutral PAH carriers are maintained despite the strong radiation fields rising from the AGNs and the SBs, while the opposite is suggested by all the other stacked spectra. More targeted observations with the JWST/MIRI will give more information about this finding and X-ray observations with the Chandra observatory could give more information about the apparent contribution of the AGN radiation field in the sources.

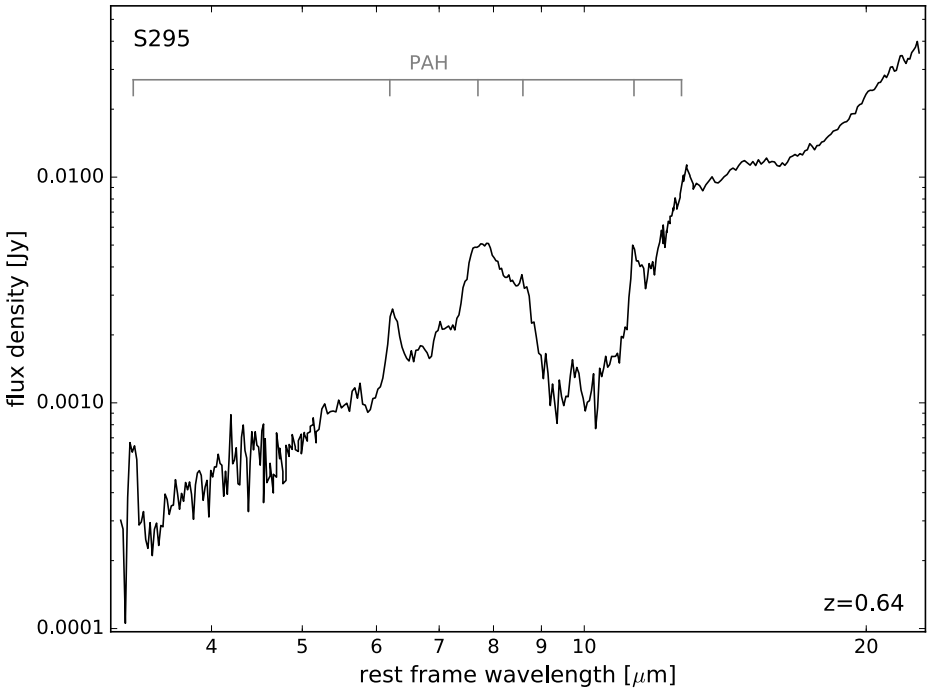

Figure 27: The source S495 (IRAS_F14537+1950), with the detected, at 4.7σ level, 3.3 μm PAH feature. The source is at redshift 0.64. The PAH features are indicated with gray marks.

4.4 INDIVIDUALLY DETECTED 3.3 μm PAH FEATURE

In my sample of 324 sources, the 3.3 μm PAH feature has been individually detected in only one source. This source is the S295 (Tab. 5), at redshift 0.64 and its spectrum is illustrated in Fig. 27. The 3.3 μm PAH feature has been detected at 4.7σ level and the flux ratio of the 6.2 to 3.3 μm is 10.62 ± 2.39. Although this flux ratio is lower than the corresponding ratio of the median SED of SB-dominated local LIRGs by Inami et al. 2018, it is a unique case in the sample and it is difficult to come to any conclusion from this. However, it is an indication that there are also sources at high redshifts with strong 3.3 μm emission with respect to the 6.2 μm feature and consequently, galaxies with big amounts of neutral PAHs compared to the ionized ones.

4.5 CONCLUSIONS

In this thesis, I investigated the 3.3 μm PAH feature of high-redshift star-forming and AGN-dominated galaxies using all available mid-IR spectra in the literature obtained by Spitzer/IRS. The main findings of the Thesis are summarized as follows:

1) The 3.3 μm PAH feature is not detected in the individual or the stacked spectra of high-redshift AGN-dominated sources. Based on the upper limits of 3.3 μm PAH feature measured from the stacked spectra in different redshift bins, we derive a lower limit for the $(\frac{F_{6.2}}{F_{3.3}})$ flux ratio that appears to increase as a function of redshift, indicating weaker 3.3 μm PAH emission with respect to the 6.2 μm emission for AGN-dominated sources, as we move to higher redshifts.

2) Similar trends stand for the starburst-dominated high-redshift sources. The 3.3 μm PAH feature is not detected in any of the stacks for the different redshift bins, while the lower limit of the $(\frac{F_{6.2}}{F_{3.3}})$ increases as a function of redshift, again suggesting that the 3.3 μm PAH feature is weaker with respect to the 6.2 μm emission at high-redshift SB-dominated sources.

3) We find a marginal 3.3 μm PAH emission feature detection (at 2.65σ level) in the stacked spectrum of a sub-sample of galaxies with strong PAH features. The emerging lower limit of $(\frac{F_{6.2}}{F_{3.3}})$ of this spectrum is comparable to the corresponding ratio of the median spectrum of SB-dominated local galaxies. Hence, the 3.3 μm PAH feature is weaker also in this case.

Bringing these results together, suggests that the 3.3 μm PAH emission feature is weaker as we move to higher redshifts. Future spectroscopic studies targeting the 3.3 μm PAH feature in high-redshift galaxies with JWST, have to take into account this result. More specifically, there is a tight correlation between the total infrared luminosity (L_{IR}) and the integrated luminosity of the 6.2 μm PAH feature ($L_{6.2PAH}$) for star-forming sources at both low and high redshifts (Schmidt 1959; Kennicutt 1998; Roussel et al. 2001; Huang et al. 2009; Menéndez-Delmestre et al. 2009; Rujopakarn et al. 2013; Cortzen et al. 2019). Thus, if the L_{IR} (or equally the star formation rate) of a source is known, the $L_{6.2PAH}$ can be easily predicted. Subsequently, the measured $(\frac{F_{6.2}}{F_{3.3}})$ presented in this

Thesis, can be used to place upper limits to the expected strength of the 3.3 μm PAH feature. On the other hand adopting the ($\frac{F_{6.2}}{F_{3.3}}$) flux ratio of local templates (Inami et al. 2018), is likely to overestimate the strengths of the 3.3 μm PAH feature of high-redshift starburst- and/or AGN-dominated sources.

5

APPENDICES

In this chapter all the data used for this work are included in tables.

Tab. 6 contains the IRAC photometric data and the description of its columns is explained more thoroughly by the Table 4.8 of the *Spitzer Enhanced Imaging Products Explanatory Supplement*[1]

There is also a collection of the spectra of all the sources in our sample.

1 https://irsa.ipac.caltech.edu/data/SPITZER/Enhanced/SEIP/docs/seip_explanatory_supplement_v3.pdf

Table 5:Coordinates in decimal degrees (J2000), Redshift and the redshift verification Status for the 324 sources in the sample.

Source ID	**AORkey**	**RA (deg)**	**DEC (deg)**	**redshift**	$\mathbf{z}_{verification}$
S1	10475264	213.96352	52.32354	0.62093	ROBUST
S2	10475520	213.87785	52.07759	0.6472	CONFIRMED
S3	10475776	213.63852	52.04891	0.77396	CONFIRMED
S4	10476288	213.89136	52.09948	0.9853	CONFIRMED
S5	10476544	214.42464	52.47315	1.14823	CONFIRMED
S6	10493952	287.09872	72.33663	3.536	ROBUST
S7	10494720	256.98541	56.50387	1.019	CONFIRMED
S8	10495488	303.71185	-27.17859	1.444	CONFIRMED
S9	10828032	214.78418	6.47638	1.43812	CONFIRMED
S10	10829568	261.07941	50.96117	1.079	CONFIRMED
S11	10830848	230.02266	20.26834	1.574	UNCHALLENGED
S12	10950144	359.97336	-12.69687	0.868	CONFIRMED
S13	10950656	333.88184	-17.73546	2.217	VERIFIED
S14	10950913	161.24843	36.93476	0.701	VERIFIED
S15	11296256	29.29375	28.86104	0.7348	CONFIRMED
S16	11298560	146.06891	9.77143	0.8177	VERIFIED
S17	11299584	176.37073	31.56343	0.811	CONFIRMED
S18	11302144	123.40014	48.21749	0.871	CONFIRMED
S19	11338496	248.10532	41.30663	1.54329	VERIFIED
S20	11338752	248.59224	41.73041	1.028	CONFIRMED
S21	11339520	248.81514	40.93563	2.5	UNCERTAIN
S22	11339776	248.90248	40.79832	0.619	CONFIRMED
S23	11341568	250.08351	42.01501	2.63259	UNCERTAIN

Source ID	AORkey	RA (deg)	DEC (deg)	redshift	$z_{verification}$
S24	11342080	250.15445	41.21518	1.951	CONFIRMED
S25	11342848	250.56541	41.14204	1.593	UNCERTAIN
S26	11343104	248.60474	40.69806	1.70055	UNCHALLENGED
S27	11343360	248.87952	41.00767	1.1525	CONFIRMED
S28	11343616	248.9735	41.34896	1.25684	VERIFIED
S29	11343872	249.23256	40.98629	2.5918	ROBUST
S30	11344384	249.41373	40.94553	1.426	VERIFIED
S31	11344640	249.41437	41.73003	1.41679	ROBUST
S32	11344896	249.69757	42.19501	1.77597	CONFIRMED
S33	11345408	249.9702	41.06256	1.60462	UNCHALLENGED
S34	11345664	250.0423	41.08961	1.099	CONFIRMED
S35	11345920	250.06699	41.35041	1.75639	UNCHALLENGED
S36	11346176	240.7123	54.84946	1.19801	CONFIRMED
S37	11346432	241.65781	53.8357	2.94765	UNCHALLENGED
S38	11346688	242.52946	53.97067	2.0321	UNCHALLENGED
S39	11346944	243.86093	54.50182	1.367	CONFIRMED
S40	11347200	243.93134	54.80809	1.692	UNCHALLENGED
S41	11347456	242.80267	55.14004	0.8785	ROBUST
S42	11347968	243.12054	54.47557	2.024	UNCHALLENGED
S43	11348224	243.22986	54.1235	0.907	CONFIRMED
S44	11348480	243.24695	54.25108	1.17813	VERIFIED
S45	11348736	243.38683	54.80869	0.827	ROBUST
S46	11348992	243.43243	54.20575	1.593	CONFIRMED
S47	11349248	243.45782	54.44146	1.154	CONFIRMED
S48	11350272	243.96378	55.12316	1.1	CONFIRMED
S49	11350528	244.34351	54.35839	1.578	UNCERTAIN

Source ID	AORkey	RA (deg)	DEC (deg)	redshift	$z_{verification}$
S50	11351296	241.15753	53.83279	0.956	CONFIRMED
S51	11351552	241.2854	54.79168	0.838	CONFIRMED
S52	11352064	241.89177	53.79678	0.60879	PROBABLE
S53	11352320	242.56477	54.10448	1.019	ROBUST
S54	11352576	7.35764	-43.8221	3.094	CONFIRMED
S55	11352832	7.49671	-43.8098	2.039	CONFIRMED
S56	11353088	7.56249	-43.0593	1.564	UNCHALLENGED
S57	11353344	7.74852	-44.3592	2.101	UNCHALLENGED
S58	11353600	8.05468	-43.76488	1.707	CONFIRMED
S59	11353856	8.14316	-43.32727	1.637	UNCHALLENGED
S60	11354112	8.53721	-43.17013	1.065	CONFIRMED
S61	11354368	9.16849	-43.6573	1.181	CONFIRMED
S62	11354624	9.31502	-42.58731	2.19	UNCHALLENGED
S63	11354880	9.55853	-43.55415	1.4	CONFIRMED
S64	11355136	9.62455	-43.74841	1.567	ROBUST
S65	11355392	10.2316	-44.21375	1.38	CONFIRMED
S66	11860224	260.85141	59.41552	1.92	UNCERTAIN
S67	11861760	259.84348	60.08345	2.23	UNCERTAIN
S68	11866112	259.61136	58.71174	1.77	VERIFIED
S69	11867392	258.90906	59.42794	2.31497	ROBUST
S70	11867904	259.685	59.3335	2.03877	ROBUST
S71	11869440	259.49377	59.47148	1.96819	ROBUST
S72	12502784	159.73723	58.87898	1.89926	VERIFIED
S73	12503040	162.16364	59.36354	1.924	VERIFIED
S74	12503296	161.5844	59.55124	1.84	UNCERTAIN

Source ID	AORkey	RA (deg)	DEC (deg)	redshift	$z_{verification}$
S75	12503808	159.43497	58.4976	1.85039	ROBUST
S76	12504064	159.65454	58.37061	1.66568	ROBUST
S77	12504576	160.57199	57.91602	1.91088	CONFIRMED
S78	12504832	160.81223	58.93493	2.25	UNCERTAIN
S79	12505088	163.52231	58.23336	1.82485	VERIFIED
S80	12505600	261.41724	58.83154	1.80375	VERIFIED
S81	12505856	257.73901	60.12931	2.33993	UNCERTAIN
S82	12506624	259.86356	59.26024	2.25	UNCERTAIN
S83	12506880	258.42813	59.6557	2.022	UNCERTAIN
S84	12507136	261.20255	60.2443	2.22	UNCERTAIN
S85	12507392	258.64371	60.47464	2.13	UNCERTAIN
S86	12507648	257.96228	58.85117	1.97562	VERIFIED
S87	12508416	257.41333	59.4579	2.53052	ROBUST
S88	12508672	258.02097	59.25242	2.38871	ROBUST
S89	12508928	258.66965	58.6847	1.97116	CONFIRMED
S90	12509440	260.00595	60.42917	2.15	UNCERTAIN
S91	12509696	260.19986	59.72251	2.20256	CONFIRMED
S92	12509952	261.7851	59.62447	1.96	UNCERTAIN
S93	12513280	218.54539	33.29253	2.656	UNCHALLENGED
S94	12513536	217.10034	35.43866	1.325	CONFIRMED
S95	12517120	216.59174	34.88046	2.0	UNCERTAIN
S96	12517632	217.61877	34.53936	2.178	ROBUST
S97	12518144	217.79074	34.46745	2.08778	CONFIRMED
S98	12518400	217.40276	32.64915	2.4	UNCERTAIN
S99	12518912	219.35481	34.25076	2.01004	VERIFIED

Source ID	AORkey	RA (deg)	DEC (deg)	redshift	$z_{verification}$
S100	12519168	217.75914	32.86451	2.0	UNCERTAIN
S101	12519936	217.89705	32.91567	1.46813	CONFIRMED
S102	12520192	219.53459	34.17104	2.5	UNCHALLENGED
S103	12520448	217.60847	33.2545	1.9	UNCERTAIN
S104	12520704	218.93793	34.4754	2.41592	ROBUST
S105	12520960	216.5473	35.20498	1.6	UNCERTAIN
S106	12521216	218.30293	34.33636	2.114	CONFIRMED
S107	12521472	218.35779	33.62695	1.85752	VERIFIED
S108	12521728	217.61877	34.53932	2.178	CONFIRMED
S109	12524800	161.36806	59.22403	2.34494	ROBUST
S110	12525056	161.04164	58.87347	2.54	UNCERTAIN
S111	12525568	161.77927	59.33643	1.73452	VERIFIED
S112	12526336	161.2213	58.91464	1.89	UNCERTAIN
S113	12526592	161.02632	58.66494	2.43	UNCERTAIN
S114	12526848	161.55656	58.99471	2.1	UNCERTAIN
S115	12527360	219.53302	34.27012	2.2	UNCERTAIN
S116	12527616	217.60719	34.49925	2.545	CONFIRMED
S117	12527872	219.18422	35.10751	1.84	UNCERTAIN
S118	12528384	216.95197	34.81422	2.2	UNCHALLENGED
S119	12529408	218.78539	33.79438	2.0	UNCERTAIN
S120	12529920	216.7039	33.49084	1.85324	ROBUST
S121	13010432	53.08774	-27.59171	0.70912	CONFIRMED
S122	13011200	53.205	-27.68074	1.222	CONFIRMED
S123	13011712	53.11029	-27.67654	1.031	CONFIRMED
S124	14014208	257.82339	58.69	0.61587	CONFIRMED

Source ID	AORkey	RA (deg)	DEC (deg)	redshift	$z_{verification}$
S125	14014464	259.57587	58.81805	0.63382	CONFIRMED
S126	14015232	259.45187	59.80573	0.76332	CONFIRMED
S127	14015488	258.39185	59.84125	0.61479	CONFIRMED
S128	14016000	257.94775	58.97766	0.79975	CONFIRMED
S129	14016256	258.35074	58.93027	0.60958	CONFIRMED
S130	14016512	259.63211	59.88802	0.7	VERIFIED
S131	15499264	259.23239	59.42778	1.46459	CONFIRMED
S132	15501824	260.07034	59.45924	2.35	UNCERTAIN
S133	15505920	258.51389	60.28236	2.0	UNCERTAIN
S134	15510528	259.46121	58.79596	2.34494	ROBUST
S135	15523584	258.70337	59.47996	3.49	UNCERTAIN
S136	15526400	260.39093	59.84636	1.64	UNCERTAIN
S137	15527680	260.40341	59.26885	1.58173	VERIFIED
S138	15528192	260.02493	59.2959	1.82062	ROBUST
S139	15533312	258.35614	60.12231	2.74508	ROBUST
S140	15534080	258.03687	59.50692	1.69	ROBUST
S141	15534336	260.75201	59.18549	1.67369	VERIFIED
S142	15536128	260.0549	60.17471	2.72	UNCERTAIN
S143	15722240	189.25699	62.19613	1.73	UNCERTAIN
S144	15738368	189.20667	62.12731	1.54	PROBABLE
S145	16157184	217.71004	33.64915	2.75821	UNCERTAIN
S146	16160768	241.38635	53.87397	2.75	UNCERTAIN
S147	16161280	243.02003	54.69704	1.87472	VERIFIED
S148	16161792	244.43573	54.00877	1.80515	VERIFIED
S149	16162048	251.00572	40.95405	1.98307	CONFIRMED

Source ID	AORkey	RA (deg)	DEC (deg)	redshift	$z_{verification}$
S150	16162304	242.71384	53.39081	2.22506	UNCERTAIN
S151	16162560	250.57051	41.02459	2.4	UNCERTAIN
S152	16162816	244.72058	54.56016	1.87759	UNCERTAIN
S153	16163584	248.79759	41.38251	2.95287	ROBUST
S154	16163840	244.10107	55.27049	2.27543	UNCERTAIN
S155	16164096	250.24408	41.9089	1.74137	ROBUST
S156	16164864	247.59247	40.83263	1.68306	VERIFIED
S157	16165120	249.95718	41.43884	2.14858	UNCERTAIN
S158	16166400	219.31305	34.88994	2.00102	UNCERTAIN
S159	16166656	219.64549	34.64422	2.59644	CONFIRMED
S160	16167168	218.25612	34.39499	2.12193	ROBUST
S161	16168448	216.5374	33.55105	2.00553	UNCERTAIN
S162	16168960	217.70146	32.42561	1.70461	CONFIRMED
S163	16169472	160.67001	32.52531	0.633	CONFIRMED
S164	16175616	341.79199	-2.09932	1.161	CONFIRMED
S165	16347392	217.88399	34.23819	1.03957	CONFIRMED
S166	16348160	217.99144	34.28064	0.71569	CONFIRMED
S167	17412352	163.51802	56.64607	1.66701	ROBUST
S168	17412864	162.1963	57.39372	1.55476	VERIFIED
S169	17413888	159.46727	57.84687	1.55	UNCERTAIN
S170	17539584	218.29292	33.76796	2.4	CONFIRMED
S171	17540352	138.75703	24.30346	0.84441	CONFIRMED
S172	17542912	197.61938	32.34541	0.99801	PROBABLE
S173	17543936	222.47375	44.69731	0.66525	VERIFIED
S174	17644288	260.21063	59.25337	1.44	CONFIRMED

Source ID	AORkey	RA (deg)	DEC (deg)	redshift	$z_{verification}$
S175	18980096	338.15173	11.73088	1.037	VERIFIED
S176	18983168	338.15161	11.73081	1.037	CONFIRMED
S177	19715840	343.49072	16.14822	0.859	VERIFIED
S178	21649408	261.76947	59.62681	1.1284	CONFIRMED
S179	21651968	258.25989	59.60305	0.668	CONFIRMED
S180	21655552	218.08406	33.25351	1.20433	CONFIRMED
S181	21758720	217.46112	35.14523	2.1017	UNCERTAIN
S182	21767936	14.18816	-27.63754	1.776	ROBUST
S183	21768960	239.14073	35.29943	1.45214	VERIFIED
S184	21824512	34.53953	-4.99613	1.094	PROBABLE
S185	23002112	161.04143	58.87361	2.57136	UNCERTAIN
S186	24143104_3	162.77562	59.27365	0.76921	CONFIRMED
S187	24143104_4	162.99397	59.11444	1.82178	UNCHALLENGED
S188	24143360_1	250.08995	41.65699	0.60236	VERIFIED
S189	24145920_2	158.31271	58.13803	0.85	CONFIRMED
S190	24146176_1	164.02039	57.70828	0.81208	ROBUST
S191	24147712	240.36874	54.75589	0.72953	CONFIRMED
S192	24150272	36.27277	-3.35486	2.24284	UNCERTAIN
S193	24151296_1	158.80727	57.57905	1.537	CONFIRMED
S194	24152064_1	36.1316	-5.47192	2.068	UNCHALLENGED
S195	24154624_2	249.28886	41.67521	0.76082	VERIFIED
S196	24160256_1	160.7319	57.93058	1.47253	CONFIRMED
S197	24163072	260.66147	58.85196	1.6237	CONFIRMED
S198	24165888_2	35.75824	-5.39324	0.70059	CONFIRMED
S199	24166656_1	158.86336	58.62013	0.885	CONFIRMED

Source ID	AORkey	RA (deg)	DEC (deg)	redshift	$z_{verification}$
S200	24167168	243.21231	55.59644	1.545	UNCERTAIN
S201	24167936_2	160.76456	58.9551	0.63964	ROBUST
S202	24168960	160.85641	58.31461	0.6862	VERIFIED
S203	24169984	159.51401	57.45053	1.2855	ROBUST
S204	24172032_2	261.58249	60.26673	0.92391	CONFIRMED
S206	24172800_2	159.66306	58.22383	0.67779	VERIFIED
S205	24172800_3	159.90567	58.13262	0.85238	CONFIRMED
S207	24173312	159.35332	58.08696	1.52253	CONFIRMED
S208	24175360_2	243.52164	53.77547	3.4346	UNCERTAIN
S209	24175872_1	260.61688	60.25725	0.74195	CONFIRMED
S210	24176128	34.42933	-4.60704	0.784	CONFIRMED
S211	24176640	260.18683	58.48997	1.697	UNCHALLENGED
S212	24178176_2	162.41751	55.96793	0.96299	VERIFIED
S213	24179456_2	35.02469	-3.26254	1.56	UNCHALLENGED
S214	24180224_1	34.58801	-4.64462	1.16402	UNCERTAIN
S215	24180224_4	34.87605	-4.59378	2.35738	UNCERTAIN
S216	24180736_2	245.45241	55.28201	0.96398	ROBUST
S217	24182272	34.1697	-4.7348	0.87464	VERIFIED
S218	24182528_1	243.93251	55.82845	1.33255	UNCERTAIN
S219	24182528_2	244.18616	55.77746	0.98173	VERIFIED
S220	24185088_1	2.04789	35.21	2.04789	UNCERTAIN
S221	24186368	241.41486	56.41769	2.55	UNCERTAIN
S222	24188160_2	259.47754	60.15374	4.27	VERIFIED
S223	24188416	160.3826	59.38285	1.06054	VERIFIED
S224	24190464_1	241.62747	54.33543	0.8205	CONFIRMED

Source ID	AORkey	RA (deg)	DEC (deg)	redshift	$z_{verification}$
S225	24190464_3	242.14841	54.39159	1.3	UNCHALLENGED
S226	24191744	258.58322	60.4568	2.99	CONFIRMED
S227	24192000	164.96545	58.30088	2.3352	UNCHALLENGED
S228	24193536_2	258.13916	58.60289	1.663	CONFIRMED
S229	24194304_1	34.53428	-4.97924	0.712	VERIFIED
S230	24194304_2	34.62741	-4.93968	1.401	CONFIRMED
S231	24194560_1	162.73192	57.93369	0.95	UNCERTAIN
S232	24194560_2	163.51709	57.67222	1.10531	VERIFIED
S233	24792064	343.49051	16.1482	0.859	VERIFIED
S234	25272064	217.50745	32.836	0.64786	PROBABLE
S235	25273089	218.92181	33.70784	2.85528	UNCERTAIN
S236	25273600	216.78407	34.35507	2.92333	UNCERTAIN
S237	25273857	219.24454	34.54168	3.79193	UNCERTAIN
S238	25274881	218.08733	35.51348	0.67193	PROBABLE
S239	25275137	218.39864	35.71191	1.297	ROBUST
S240	25276160	164.06546	57.39614	0.64951	CONFIRMED
S241	25276416	161.97221	58.35186	0.8898	VERIFIED
S242	25277440	161.07773	56.33541	1.845	ROBUST
S243	25278208	161.71875	57.19864	0.99865	VERIFIED
S244	25278464	163.49675	59.35092	0.83763	VERIFIED
S245	25278976	159.29688	58.98022	0.93184	VERIFIED
S246	25387264	163.69693	58.31932	1.65997	UNCHALLENGED
S247	25388032	162.97391	56.83498	1.98306	VERIFIED
S248	25388288	240.0179	55.07499	1.99871	UNCHALLENGED
S249	25388544	159.87968	58.28598	1.83621	VERIFIED

Source ID	AORkey	RA (deg)	DEC (deg)	redshift	$z_{verification}$
S250	25388800	160.47987	57.26747	1.72347	UNCHALLENGED
S251	25389056	160.3102	57.84002	1.91	UNCHALLENGED
S252	25389312	160.98119	56.46585	1.95692	CONFIRMED
S253	25389568	162.50435	59.18667	2.16909	VERIFIED
S254	25389824	216.87598	32.68522	1.79512	UNCHALLENGED
S255	25390080	217.47791	33.02629	2.07945	CONFIRMED
S256	25390336	217.76225	32.65788	1.64743	UNCHALLENGED
S257	25390592	219.02115	33.71188	1.9917	CONFIRMED
S258	25390848	242.46124	53.48604	1.71655	UNCHALLENGED
S259	25391104	261.34189	59.8807	1.89547	ROBUST
S260	25976832	151.00523	42.52312	1.66574	CONFIRMED
S261	25977088	228.28233	60.9992	1.83061	ROBUST
S262	25977344	200.33549	57.71642	1.77894	ROBUST
S263	25977600	147.69812	48.01321	1.742	ROBUST
S264	25977856	164.96277	9.15153	1.68975	ROBUST
S265	26415104	324.45831	-20.70879	0.63634	CONFIRMED
S266	26419712	62.20211	-75.12185	0.693	CONFIRMED
S267	26680576	160.39905	58.65382	1.95487	VERIFIED
S268	26701056	25.28831	13.89109	0.621	CONFIRMED
S269	26702848	115.29462	31.20007	0.63196	PROBABLE
S270	26703360	152.00018	7.50453	0.877	VERIFIED
S271	26705408	275.33701	39.71241	0.798	CONFIRMED
S272	26705664	277.81171	29.11952	0.842	CONFIRMED
S273	26706432	356.01578	82.44466	0.735	CONFIRMED
S274	26904832	35.27285	35.9371	0.68466	VERIFIED

Source ID	AORkey	RA (deg)	DEC (deg)	redshift	$z_{verification}$
S275	27426048	343.49069	16.14824	0.859	VERIFIED
S276	27428352	343.4906	16.14819	0.859	VERIFIED
S277	27428864	82.73514	13.53204	2.06	CONFIRMED
S278	27430912	82.73505	13.53193	2.06	VERIFIED
S279	27435008	343.49069	16.14825	0.859	VERIFIED
S280	27440384	343.49069	16.14823	0.859	VERIFIED
S281	3732736	156.14397	47.15271	2.2856	VERIFIED
S282	3732992	213.94258	11.49561	2.55109	CONFIRMED
S283	4670976	37.16294	-10.18611	2.256	CONFIRMED
S284	4671232	337.1265	-5.31519	1.981	CONFIRMED
S285	4732160	194.24969	4.45949	1.02558	ROBUST
S286	4732416	231.47449	51.61357	2.88409	ROBUST
S287	4733184	131.411	34.34543	2.13781	CONFIRMED
S288	4733440	192.30779	-5.9887	2.247	VERIFIED
S289	4733952	239.7299	33.38858	1.65348	CONFIRMED
S290	4738560	151.4693	49.58019	1.12	ROBUST
S291	4964352	12.54092	-0.65025	0.7293	CONFIRMED
S292	4965632	24.86317	1.26304	0.612	CONFIRMED
S293	4967424	41.48018	1.39107	0.798	ROBUST
S294	4974592	160.66995	32.52536	0.633	CONFIRMED
S295	4981760	224.02507	19.64443	0.64	VERIFIED
S296	4983552	233.18338	32.71297	0.9257	CONFIRMED
S297	4984832	243.59215	32.56766	0.71	CONFIRMED
S298	4986880	261.28085	37.15897	0.689	CONFIRMED
S299	4990720	322.97278	-1.69538	0.72802	VERIFIED

Source ID	AORkey	RA (deg)	DEC (deg)	redshift	$z_{verification}$
S300	5072640	160.45354	59.37569	2.84	UNCERTAIN
S301	9819904	219.1844	35.10748	1.84043	VERIFIED
S302	9820672	217.50801	33.76071	2.46	UNCERTAIN
S303	9820928	218.91412	33.69982	2.62	UNCERTAIN
S304	9821440	217.49316	32.43773	2.64	UNCERTAIN
S305	9821696	218.49193	33.43549	1.9416	VERIFIED
S306	9821952	218.76709	35.79549	2.01004	VERIFIED
S307	9822208	217.01724	33.35992	2.34	UNCERTAIN
S308	9822464	218.32755	33.35767	2.69117	UNCERTAIN
S309	9822720	217.41321	35.59957	2.498	UNCHALLENGED
S310	9822976	218.69887	33.04171	1.85467	VERIFIED
S311	9823232	217.35367	35.55577	2.65445	ROBUST
S312	9823488	217.38095	32.30783	2.2	UNCHALLENGED
S313	9824000	216.69054	35.31704	1.7703	VERIFIED
S314	9824512	216.61057	34.79195	2.10481	VERIFIED
S315	9824768	217.4202	34.68014	1.98606	ROBUST
S316	9825024	218.17734	34.37549	2.2	UNCERTAIN
S317	9825280	218.62325	34.6092	2.00402	CONFIRMED
S318	9825536	218.83667	34.0716	2.10947	ROBUST
S319	9825792	217.11653	33.76401	2.772	UNCHALLENGED
S320	9826048	218.60214	33.76217	2.263	UNCHALLENGED
S321	9826816	218.21613	33.5936	1.80655	ROBUST
S322	9827072	216.68469	33.51435	3.312	CONFIRMED
S323	9827328	218.85008	33.11877	2.59	UNCERTAIN
S324	9827584	216.72182	33.03922	1.87328	CONFIRMED

Table 6: The IRAC photometry of the 221 sources in the sample, which have been observed in all 4 IRAC channels. The second row includes the names of the columns as they are provided by the SEIP.

Source ID	$\mathbf{f}_{3.6\mu m}$ (μJ)	$\mathbf{err}_{3.6\mu m}$ (μJ)	$\mathbf{f}_{4.5\mu m}$ (μJ)	$\mathbf{err}_{4.5\mu m}$ (μJ)	$\mathbf{f}_{5.8\mu m}$ (μJ)	$\mathbf{err}_{5.8\mu m}$ (μJ)	$\mathbf{f}_{8.0\mu m}$ (μJ)	$\mathbf{err}_{8.0\mu m}$ (μJ)
	i1_f_ap1	**i1_df_ap1**	**i2_f_ap1**	**i2_df_ap1**	**i3_f_ap1**	**i3_df_ap1**	**i4_f_ap1**	**i4_df_ap1**
S1	66.8	0.1	79.8	0.1	156.5	0.8	376.5	0.8
S2	420.8	0.2	460.1	0.2	583.5	0.7	668.9	0.7
S3	140.4	0.1	199.4	0.2	341.3	0.7	671.4	1.0
S4	484.7	0.2	719.8	0.3	1078.2	0.9	1534.6	0.8
S5	502.3	0.2	823.8	0.3	1316.6	1.0	1983.4	0.9
S6	192.2	1.5	206.1	1.8	247.1	4.9	471.3	7.0
S9	1580.7	4.5	2289.5	6.0	3576.0	16.4	5826.0	16.9
S10	113.6	1.2	109.3	1.5	151.5	4.4	393.8	7.4
S11	305.2	1.8	402.9	2.4	544.4	6.6	836.0	8.2
S19	76.4	0.7	188.5	1.2	435.0	3.6	946.8	4.9
S21	32.8	0.6	68.1	0.9	188.7	3.8	564.9	5.6
S22	99.4	0.5	82.4	0.4	110.1	2.7	127.9	2.9
S23	48.2	0.6	83.4	1.0	172.1	3.7	517.6	5.7
S24	101.0	0.7	200.8	1.0	406.0	3.6	722.5	4.5
S25	178.5	0.9	334.5	1.6	553.4	4.5	906.8	5.7
S28	163.1	0.8	216.1	1.1	339.8	3.5	778.1	6.0
S29	27.8	0.2	52.2	0.3	133.9	1.3	397.3	1.7
S30	191.8	1.0	374.0	1.6	574.2	3.3	1085.8	4.9
S31	159.4	0.8	259.4	1.1	400.5	3.8	666.9	4.4
S32	203.7	1.0	249.7	1.3	593.3	4.7	951.2	6.1
S33	238.8	1.0	396.5	1.4	594.8	4.5	948.1	5.1
S34	1683.0	2.4	2650.8	3.2	4005.8	9.1	5707.2	7.9
S35	320.2	1.1	441.0	1.5	733.2	4.8	1269.7	6.2
S36	242.1	0.9	372.6	1.4	657.6	5.1	1071.5	5.5
S37	112.9	0.8	170.1	1.2	307.8	4.5	655.7	5.7
S38	174.9	0.9	260.6	1.5	506.7	5.6	940.8	5.4
S39	207.5	0.9	343.8	1.4	531.8	6.3	825.2	6.3
S40	287.0	1.0	402.3	1.9	645.8	6.1	1111.2	6.5
S41	149.6	0.8	155.9	1.1	280.4	5.2	573.7	6.2
S42	25.3	0.5	42.9	0.9	97.9	4.2	240.5	5.4

Source ID	$\mathbf{f}_{3.6\mu m}$ (μJ)	$\mathbf{err}_{3.6\mu m}$ (μJ)	$\mathbf{f}_{4.5\mu m}$ (μJ)	$\mathbf{err}_{4.5\mu m}$ (μJ)	$\mathbf{f}_{5.8\mu m}$ (μJ)	$\mathbf{err}_{5.8\mu m}$ (μJ)	$\mathbf{f}_{8.0\mu m}$ (μJ)	$\mathbf{err}_{8.0\mu m}$ (μJ)
	i1_f_ap1	**i1_df_ap1**	**i2_f_ap1**	**i2_df_ap1**	**i3_f_ap1**	**i3_df_ap1**	**i4_f_ap1**	**i4_df_ap1**
S43	247.3	1.0	321.1	1.4	475.1	5.6	674.2	6.3
S44	400.2	1.6	589.2	2.2	818.4	7.4	1097.6	6.6
S45	231.1	1.0	237.6	1.1	286.1	5.1	354.0	4.5
S46	196.5	1.1	329.6	1.6	492.0	6.8	752.2	5.4
S48	252.8	1.0	362.9	1.8	535.2	5.7	822.9	6.5
S49	174.0	0.8	391.6	1.3	860.5	5.2	1524.1	5.2
S51	62.1	0.6	68.9	1.0	118.4	3.8	277.2	5.1
S52	94.7	0.7	73.9	1.0	95.1	4.9	153.3	6.0
S55	526.7	1.3	771.8	1.9	1431.4	6.2	2496.7	7.8
S56	193.8	0.9	370.0	1.4	656.6	4.9	1393.2	6.8
S57	515.1	1.5	642.7	1.9	1045.3	6.5	1837.8	8.1
S58	913.9	1.8	1568.2	2.6	2595.3	10.9	4411.9	8.8
S59	151.3	0.9	241.2	1.3	443.8	5.0	738.3	7.1
S61	335.3	0.9	526.6	1.2	729.5	4.6	1081.8	5.2
S62	195.4	1.0	313.3	1.5	640.5	5.2	1372.1	7.6
S63	423.8	1.7	655.3	1.8	811.1	5.5	1372.6	7.4
S64	710.6	1.9	1187.1	2.2	1993.0	7.0	3288.5	7.3
S65	338.5	1.1	597.2	1.8	994.5	5.4	1698.2	7.5
S66	19.4	1.1	40.0	1.5	90.1	7.0	197.7	7.0
S67	16.1	1.0	23.9	1.2	48.2	6.9	199.5	7.4
S69	18.1	1.1	37.4	0.9	73.9	3.8	286.3	5.7
S70	24.5	0.7	45.3	1.0	134.6	4.4	511.1	6.1
S71	23.6	0.8	46.7	0.6	188.4	2.7	708.8	4.4
S73	74.8	0.6	96.1	1.0	122.8	2.9	118.0	5.5
S78	10.0	0.3	20.8	0.5	57.0	1.8	111.7	4.2
S79	36.2	0.5	47.6	0.7	56.6	3.8	42.4	4.7
S82	41.4	0.3	79.2	0.5	171.8	1.9	302.5	4.1
S83	32.9	0.2	59.5	0.3	127.3	1.1	342.4	1.5
S85	41.9	1.1	70.3	1.6	194.3	6.7	350.4	8.4
S86	60.0	1.1	104.4	0.9	187.3	4.4	379.5	4.7
S88	53.4	0.9	92.9	0.9	192.9	5.7	371.6	8.2

Source ID	$\mathbf{f}_{3.6\mu m}$ (μJ)	$\mathbf{err}_{3.6\mu m}$ (μJ)	$\mathbf{f}_{4.5\mu m}$ (μJ)	$\mathbf{err}_{4.5\mu m}$ (μJ)	$\mathbf{f}_{5.8\mu m}$ (μJ)	$\mathbf{err}_{5.8\mu m}$ (μJ)	$\mathbf{f}_{8.0\mu m}$ (μJ)	$\mathbf{err}_{8.0\mu m}$ (μJ)
	i1_f_ap1	**i1_df_ap1**	**i2_f_ap1**	**i2_df_ap1**	**i3_f_ap1**	**i3_df_ap1**	**i4_f_ap1**	**i4_df_ap1**
S90	37.8	1.1	82.3	1.6	190.9	7.2	415.9	7.9
S91	8.4	0.6	21.1	1.2	77.1	3.1	290.5	6.5
S93	18.0	0.3	24.3	0.4	35.8	1.5	84.7	3.3
S94	232.4	0.7	291.7	0.8	253.6	2.3	228.7	3.4
S95	3.9	0.3	4.5	0.4	8.6	1.7	40.5	3.3
S96	27.2	0.2	46.6	0.3	112.9	1.3	299.7	1.9
S97	7.3	0.2	9.1	0.4	31.0	1.4	68.9	3.3
S98	14.1	0.3	21.2	0.5	36.6	1.9	134.1	3.4
S99	51.9	0.4	87.2	0.7	163.6	2.1	278.7	3.6
S101	65.3	0.4	133.9	0.7	252.6	2.3	504.3	3.2
S103	69.4	0.4	137.6	0.6	299.9	1.9	577.7	3.3
S105	45.6	0.2	75.1	0.4	157.5	1.8	400.5	3.2
S106	26.4	0.3	33.8	0.5	64.0	2.0	102.6	3.3
S107	60.4	0.3	80.3	0.5	110.5	1.7	141.3	3.3
S109	30.2	0.3	44.3	0.5	87.5	1.6	198.8	4.0
S110	62.3	0.4	145.0	0.6	404.8	2.2	1058.0	4.0
S111	138.0	0.7	136.1	0.9	130.7	2.2	167.7	5.1
S112	69.0	0.4	144.6	0.6	284.9	2.1	495.8	2.7
S113	45.4	0.6	64.9	0.7	128.2	2.3	242.1	3.9
S114	26.6	0.3	33.1	0.4	55.9	1.4	125.8	2.3
S115	19.0	0.2	32.0	0.3	68.8	1.4	180.2	2.5
S116	19.2	0.2	49.5	0.5	150.7	1.9	530.1	2.6
S117	35.6	0.3	99.3	0.6	298.7	2.2	743.8	3.9
S118	13.7	0.3	47.8	0.5	163.6	1.7	479.7	4.0
S120	54.0	0.4	178.9	0.7	470.9	2.7	959.6	3.9
S121	147.3	0.8	143.7	1.1	172.9	3.7	307.5	6.2
S122	130.1	0.7	220.6	1.1	349.3	3.7	606.6	4.9
S123	180.2	0.8	255.8	1.0	358.9	3.3	548.8	4.1
S124	1148.7	3.6	1479.4	3.7	1948.7	10.2	2432.8	10.0
S125	658.2	2.2	865.4	3.0	1145.7	9.6	1560.9	9.5
S126	605.2	1.0	876.3	0.9	1272.1	3.3	1681.0	2.7

Source ID	$\mathbf{f}_{3.6\mu m}$ (μJ)	$\mathbf{err}_{3.6\mu m}$ (μJ)	$\mathbf{f}_{4.5\mu m}$ (μJ)	$\mathbf{err}_{4.5\mu m}$ (μJ)	$\mathbf{f}_{5.8\mu m}$ (μJ)	$\mathbf{err}_{5.8\mu m}$ (μJ)	$\mathbf{f}_{8.0\mu m}$ (μJ)	$\mathbf{err}_{8.0\mu m}$ (μJ)
	i1_f_ap1	**i1_df_ap1**	**i2_f_ap1**	**i2_df_ap1**	**i3_f_ap1**	**i3_df_ap1**	**i4_f_ap1**	**i4_df_ap1**
S127	737.6	1.4	1017.5	1.7	1306.6	5.2	1718.7	5.9
S128	478.6	1.4	787.8	1.7	1212.3	5.4	1877.9	7.2
S129	176.8	0.8	332.5	1.1	694.7	4.6	1349.2	4.7
S130	149.6	0.8	243.1	1.2	517.7	3.8	1203.8	4.2
S131	129.5	1.4	242.3	1.0	292.3	4.3	455.9	5.1
S132	133.8	0.7	226.6	1.5	396.8	3.4	612.9	6.6
S134	38.0	0.9	107.4	1.7	301.9	6.2	943.5	8.8
S136	87.0	0.7	205.8	1.4	424.0	4.5	728.4	8.3
S139	158.1	0.8	251.6	1.7	510.8	3.4	1022.4	6.6
S140	52.4	0.4	106.5	0.6	184.5	2.1	351.4	3.6
S141	58.7	1.2	107.9	1.6	160.1	7.5	346.1	7.9
S142	61.1	0.8	115.3	1.6	180.6	5.0	276.3	8.3
S143	49.6	0.0	67.3	0.0	68.7	0.1	54.0	0.1
S144	30.6	0.0	52.0	0.1	95.1	0.2	220.4	0.3
S145	36.3	0.2	56.5	0.4	100.1	1.5	215.9	2.6
S147	33.9	0.5	46.7	0.7	48.0	4.2	54.9	3.8
S149	37.5	0.9	55.4	0.8	74.1	4.0	139.9	4.3
S151	64.3	0.7	174.0	1.4	432.2	4.2	1143.0	6.9
S152	61.7	0.6	76.5	1.0	95.8	5.0	67.8	5.8
S153	14.3	0.5	18.6	0.8	37.7	2.8	111.1	5.2
S157	19.0	0.6	31.9	0.8	61.7	3.3	90.5	5.6
S158	162.5	0.6	274.6	0.7	546.7	2.5	1016.7	3.5
S159	49.1	0.4	96.8	0.7	242.7	2.8	573.2	4.0
S160	96.2	0.4	164.4	0.6	331.7	2.0	633.2	3.0
S161	48.9	0.3	67.4	0.5	107.0	1.8	194.6	2.4
S162	119.1	0.5	217.6	0.7	401.0	2.7	713.4	3.3
S164	130.7	0.8	127.2	1.1	107.0	2.7	92.3	5.6
S165	1234.2	1.0	1775.2	1.3	2539.0	3.7	3615.6	3.3
S166	1202.9	1.0	1672.5	1.3	2491.6	3.6	3853.6	3.4
S168	157.0	0.9	279.6	1.2	448.3	3.9	778.2	6.1
S170	631.5	0.9	896.0	1.0	1661.8	3.5	3428.6	4.0
S174	234.9	0.5	678.5	1.6	1559.6	2.5	3716.8	4.7

Source ID	$\mathbf{f}_{3.6\mu m}$ (μJ)	$\mathbf{err}_{3.6\mu m}$ (μJ)	$\mathbf{f}_{4.5\mu m}$ (μJ)	$\mathbf{err}_{4.5\mu m}$ (μJ)	$\mathbf{f}_{5.8\mu m}$ (μJ)	$\mathbf{err}_{5.8\mu m}$ (μJ)	$\mathbf{f}_{8.0\mu m}$ (μJ)	$\mathbf{err}_{8.0\mu m}$ (μJ)
	i1_f_ap1	**i1_df_ap1**	**i2_f_ap1**	**i2_df_ap1**	**i3_f_ap1**	**i3_df_ap1**	**i4_f_ap1**	**i4_df_ap1**
S176	3074.9	18.6	4230.8	21.1	6866.9	62.7	11244.2	49.2
S179	103.9	0.5	254.4	0.7	645.1	3.0	2505.8	5.3
S180	415.3	0.6	716.3	1.0	1118.8	2.6	1822.2	3.9
S181	512.9	0.8	693.9	1.0	940.3	2.6	1577.5	2.5
S184	81.9	0.2	132.3	0.3	314.1	1.1	909.2	1.7
S185	62.3	0.4	145.0	0.6	404.8	2.2	1058.0	4.0
S186	934.3	1.8	1206.0	2.3	1537.1	6.8	2024.6	6.6
S187	347.0	1.1	552.1	1.6	956.9	5.2	1575.1	6.3
S188	668.7	2.1	1009.3	2.1	1463.2	6.1	2009.4	7.7
S189	323.3	1.1	464.8	1.5	726.1	4.7	1138.9	5.7
S190	58.9	0.4	88.1	0.6	150.3	1.8	419.8	3.1
S191	1184.0	2.0	1836.1	2.7	2662.5	8.3	3886.3	7.3
S192	36.0	0.7	82.0	1.2	285.8	5.5	901.9	8.7
S193	54.0	0.6	81.6	1.0	120.3	4.2	326.0	6.1
S194	797.1	1.7	1209.8	2.3	2327.5	7.9	4126.4	9.7
S196	655.2	1.5	1106.4	2.2	1761.8	6.4	2837.2	7.0
S198	789.9	1.6	1318.9	2.3	1982.1	7.0	3504.5	8.8
S199	203.9	1.2	311.4	1.8	501.3	4.3	1057.8	6.8
S200	729.6	1.6	1150.3	2.2	2251.3	7.6	3775.6	7.0
S201	291.6	1.1	347.0	1.3	594.1	3.8	1112.0	5.1
S202	203.2	0.9	192.0	1.0	332.1	3.6	1167.9	5.2
S203	600.2	1.5	1173.9	2.3	1990.0	7.1	3478.0	8.3
S204	1015.9	2.7	1521.5	3.7	2116.8	10.4	2955.6	10.3
S206	896.0	1.7	1291.9	2.3	1728.8	6.5	2541.6	7.8
S205	253.8	1.0	363.6	1.4	585.3	4.8	931.3	6.0
S207	771.8	1.5	1349.5	2.3	1975.0	6.4	3598.3	8.2
S208	476.7	1.3	629.1	1.8	879.1	6.0	1322.5	6.8
S210	540.0	0.4	805.2	0.6	1182.3	2.1	1742.6	1.7
S211	90.5	0.4	181.1	0.5	370.7	1.9	821.3	3.9
S212	200.8	0.9	455.1	2.1	957.3	6.6	1767.8	8.0
S213	248.6	1.1	405.3	1.6	678.7	6.0	1300.3	8.6
S214	286.5	0.3	526.5	0.5	887.5	1.5	1457.3	1.5

Source ID	$\mathbf{f}_{3.6\mu m}$ (μJ)	$\mathbf{err}_{3.6\mu m}$ (μJ)	$\mathbf{f}_{4.5\mu m}$ (μJ)	$\mathbf{err}_{4.5\mu m}$ (μJ)	$\mathbf{f}_{5.8\mu m}$ (μJ)	$\mathbf{err}_{5.8\mu m}$ (μJ)	$\mathbf{f}_{8.0\mu m}$ (μJ)	$\mathbf{err}_{8.0\mu m}$ (μJ)
	i1_f_ap1	**i1_df_ap1**	**i2_f_ap1**	**i2_df_ap1**	**i3_f_ap1**	**i3_df_ap1**	**i4_f_ap1**	**i4_df_ap1**
S215	56.7	0.3	161.4	0.5	463.8	5.6	1134.6	7.1
S216	600.8	1.5	931.2	2.1	1387.9	7.1	2143.4	8.3
S217	1956.8	0.8	2831.9	1.0	4154.6	3.7	6362.4	2.9
S218	199.7	0.5	376.7	1.0	843.9	2.7	1880.3	5.4
S219	764.3	1.0	1189.5	1.3	1828.5	3.7	2641.9	2.8
S222	502.3	1.3	458.0	1.2	626.5	3.3	1443.2	9.5
S224	709.6	1.5	1023.6	2.0	1539.0	7.9	2241.8	6.7
S225	897.3	1.7	1530.5	2.5	2147.7	8.0	3248.3	6.8
S226	166.6	1.5	251.1	1.8	465.5	7.6	1062.4	7.5
S227	289.6	1.1	427.1	2.0	854.1	5.2	1750.4	7.3
S228	425.9	2.5	659.8	2.7	1015.6	9.1	1611.8	9.3
S229	1439.4	0.7	2086.4	0.9	3041.3	2.8	4108.8	2.1
S230	645.0	0.4	1224.0	0.7	2039.4	2.2	3338.9	2.2
S231	402.1	1.2	627.7	1.7	981.0	5.6	1647.9	6.5
S232	747.8	1.0	1142.5	1.4	1932.6	4.0	2737.9	3.7
S234	181.6	0.5	274.9	0.9	522.7	3.2	1014.1	3.5
S235	237.0	0.6	494.5	1.0	927.6	3.0	1935.5	3.9
S236	173.8	0.4	266.8	0.8	541.7	3.0	1363.4	4.5
S237	355.3	0.9	504.4	0.9	820.0	2.9	1321.9	3.7
S238	99.6	0.4	78.8	0.6	96.9	1.6	289.3	3.3
S239	225.6	0.6	435.0	1.0	801.3	3.1	1598.1	4.2
S240	404.1	0.9	719.1	1.3	1110.6	3.9	1866.8	6.4
S241	426.9	1.2	639.0	2.2	726.6	5.1	1574.4	6.8
S243	171.1	0.8	312.1	1.3	689.2	4.8	1518.6	6.3
S245	90.3	0.7	172.9	1.1	355.2	4.4	849.2	6.0
S246	540.9	0.9	967.6	1.4	1653.2	6.1	2860.4	6.5
S247	254.5	1.0	409.1	1.5	769.0	4.9	1283.5	6.3
S248	189.6	1.1	319.6	1.4	579.1	5.9	1029.3	5.8
S249	247.3	1.0	384.9	1.5	674.8	5.0	1037.9	7.3
S250	414.6	1.3	662.9	1.8	1117.7	5.8	1794.5	6.9
S252	559.0	1.4	754.9	2.1	1378.2	6.3	2439.1	10.2
S253	190.5	1.1	331.8	1.3	677.4	3.6	1162.8	6.8

Source ID	$\mathbf{f}_{3.6\mu m}$ (μJ)	$\mathbf{err}_{3.6\mu m}$ (μJ)	$\mathbf{f}_{4.5\mu m}$ (μJ)	$\mathbf{err}_{4.5\mu m}$ (μJ)	$\mathbf{f}_{5.8\mu m}$ (μJ)	$\mathbf{err}_{5.8\mu m}$ (μJ)	$\mathbf{f}_{8.0\mu m}$ (μJ)	$\mathbf{err}_{8.0\mu m}$ (μJ)
	i1_f_ap1	**i1_df_ap1**	**i2_f_ap1**	**i2_df_ap1**	**i3_f_ap1**	**i3_df_ap1**	**i4_f_ap1**	**i4_df_ap1**
S254	199.8	0.5	370.4	0.8	718.0	2.8	1335.7	3.7
S255	291.8	0.8	443.6	0.9	855.1	3.5	1546.4	4.0
S256	326.4	0.6	515.8	1.2	809.1	3.5	1302.8	3.9
S257	255.0	0.6	398.1	0.9	731.6	2.8	1264.5	3.9
S258	540.1	1.4	956.2	2.1	1648.5	7.3	2925.9	7.4
S259	187.2	1.4	322.4	2.1	578.6	7.2	1044.4	9.0
S269	3755.3	1.2	4985.7	1.5	6754.3	3.9	9264.1	3.3
S277	1729.1	6.8	2373.1	8.6	3541.8	26.7	5688.4	21.3
S281	262.7	1.9	291.3	2.8	420.4	11.0	919.8	9.7
S285	4760.7	7.8	7292.8	10.6	11349.0	29.9	16738.5	25.0
S291	277.8	2.5	415.1	3.0	980.5	12.1	3215.7	15.9
S292	288.8	2.2	488.7	3.4	1109.3	13.2	3285.1	18.4
S293	187.3	1.8	319.2	2.8	810.1	11.0	3189.7	15.0
S300	5.0	0.5	12.0	0.9	39.0	3.0	112.1	6.6
S303	13.3	0.3	22.0	0.5	58.9	1.6	251.6	3.5
S304	26.9	0.3	46.9	0.5	106.6	1.9	210.3	3.4
S305	15.9	0.2	22.4	0.4	38.4	1.2	102.1	2.1
S308	3.6	0.2	7.0	0.4	28.9	1.1	83.7	3.0
S309	40.3	0.3	85.2	0.6	179.7	2.0	417.9	3.5
S310	19.5	0.3	31.2	0.5	46.6	2.1	84.5	3.3
S311	5.5	0.3	11.0	0.5	23.0	1.7	73.2	3.6
S312	8.8	0.3	13.4	0.5	19.0	1.9	64.0	3.5
S313	32.3	0.2	52.4	0.4	83.5	1.7	157.4	2.7
S314	17.3	0.3	26.0	0.5	38.9	1.8	38.7	3.0
S315	9.3	0.2	18.1	0.4	52.6	1.7	116.4	2.8
S316	35.2	0.3	57.5	0.5	122.0	1.9	228.3	3.6
S317	7.0	0.3	11.8	0.5	16.8	1.5	107.9	3.2
S319	49.8	0.3	79.1	0.5	147.1	2.0	298.1	3.4
S320	13.9	0.3	22.9	0.5	58.8	1.7	158.4	3.3
S321	40.1	0.3	56.9	0.3	65.4	2.2	102.6	1.6
S322	60.0	0.4	91.3	0.5	153.0	2.3	383.7	3.5
S323	16.5	0.3	35.2	0.5	92.0	1.7	263.7	3.4
S324	18.1	0.3	29.1	0.5	31.0	2.2	61.0	3.1

Figure 28: The 324 IRS spectra included in the thesis sample. For the sources with available IRAC photometry, the photometric points are depicted by the red dots. The red and brown vertical dashed lines correspond to the wavelengths where the 3.3, 6.2, 7.7, 8.6, 11.3 and 12.7 μm PAH lines, respectively, are expected to be. With different colors are indicated the bands of the 5.340 FeII (orange), the 5.511 H2 S(7), 6.909 H2 S(5) and H2 S(3) (blue) and 10.511 SIV (yellow). The gray shaded area shows flux error that is the aggregation of the statistical (RMS) error, which is poissonian or gaussian (for very faint sources), plus the systematic (SYS) error that comes from the combination of the two nod spectra.

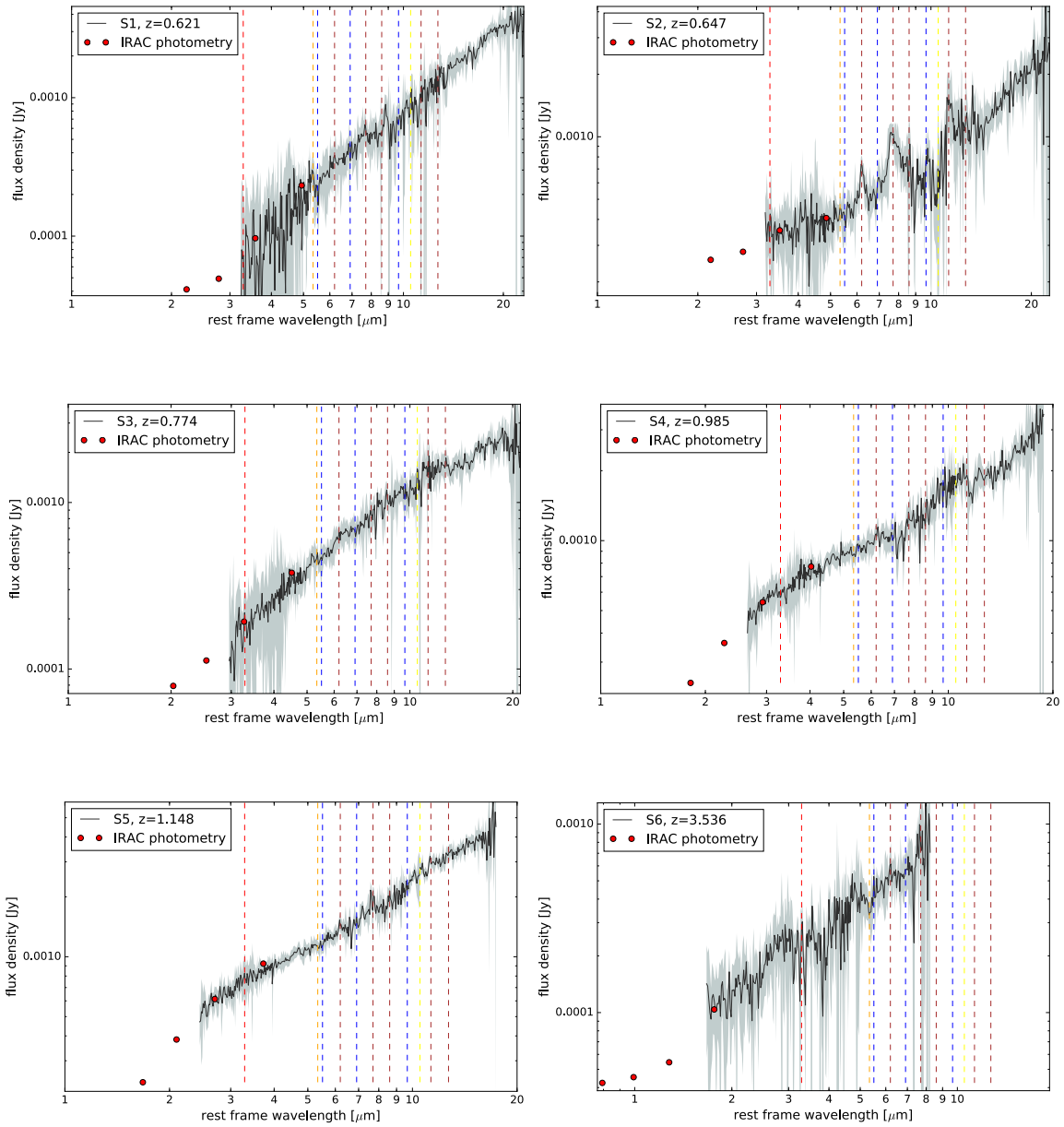

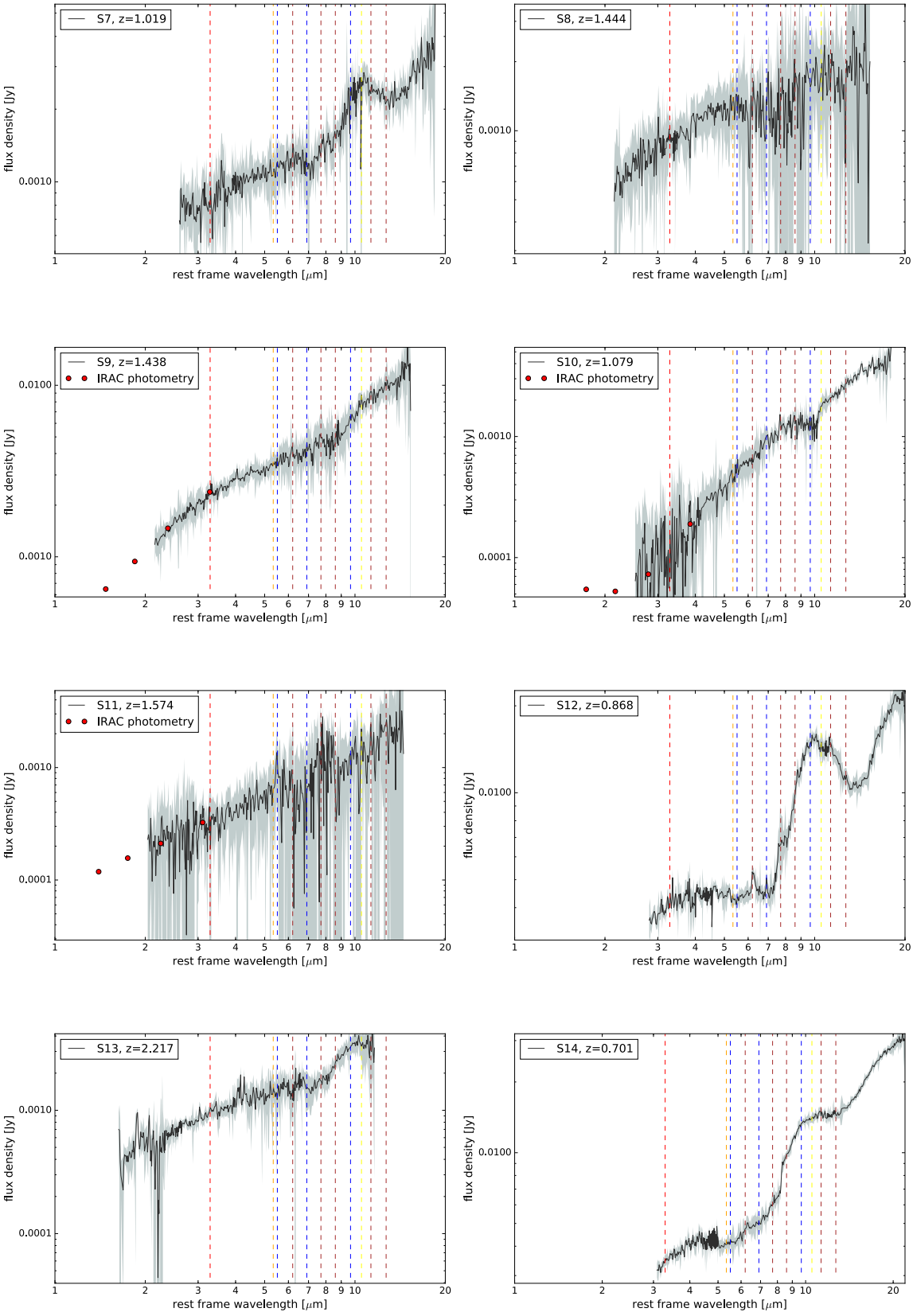
S7, z=1.019
S8, z=1.444
S9, z=1.438
IRAC photometry
S10, z=1.079
IRAC photometry
S11, z=1.574
IRAC photometry
S12, z=0.868
S13, z=2.217
S14, z=0.701
flux density [Jy]
rest frame wavelength [μm]

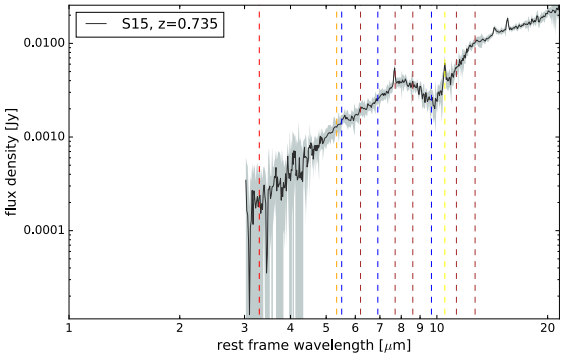
S15, z=0.735
flux density [Jy]
rest frame wavelength [μm]

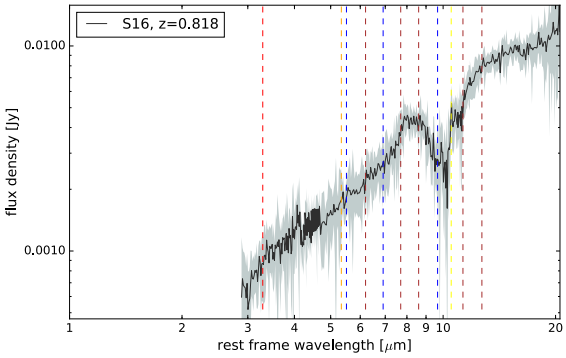
S16, z=0.818
flux density [Jy]
rest frame wavelength [μm]

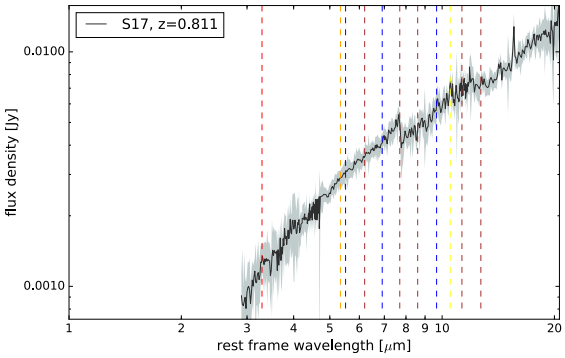
S17, z=0.811
flux density [Jy]
rest frame wavelength [μm]

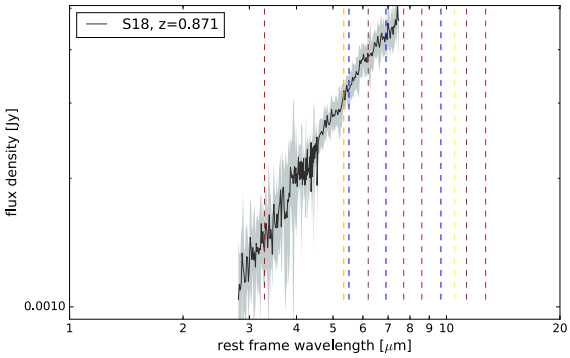
S18, z=0.871
flux density [Jy]
rest frame wavelength [μm]

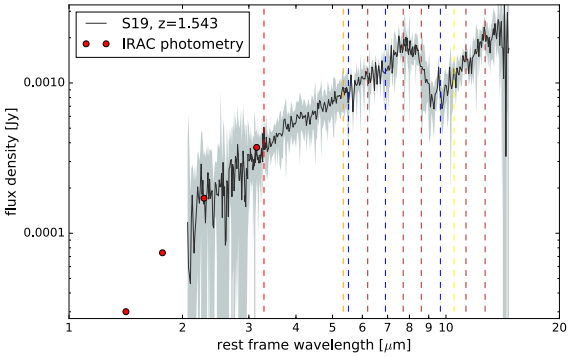
S19, z=1.543
IRAC photometry
flux density [Jy]
rest frame wavelength [μm]

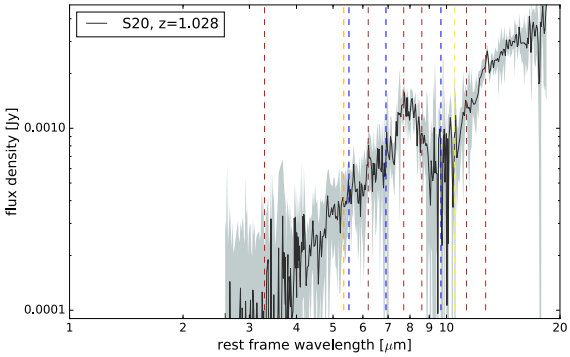
S20, z=1.028
flux density [Jy]
rest frame wavelength [μm]

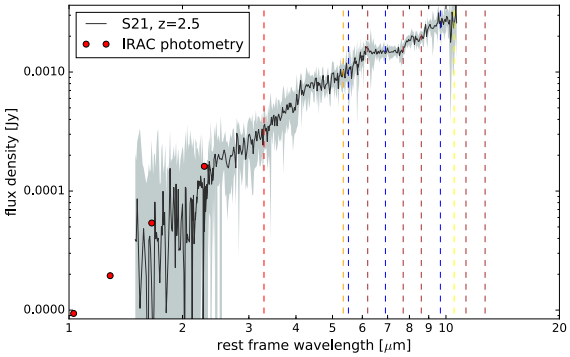
S21, z=2.5
IRAC photometry
flux density [Jy]
rest frame wavelength [μm]

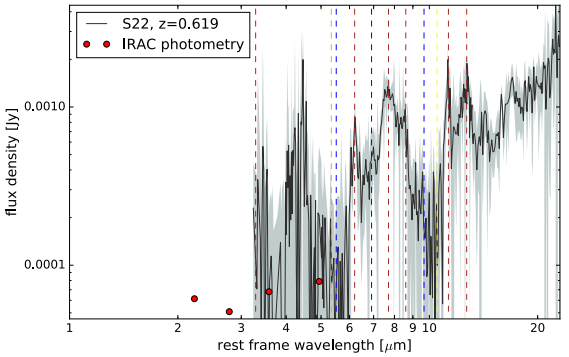
S22, z=0.619
IRAC photometry
flux density [Jy]
rest frame wavelength [μm]

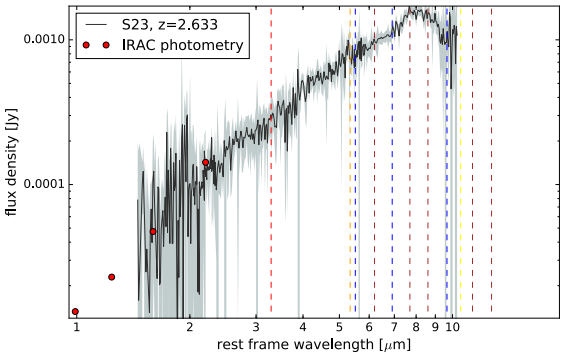
S23, z=2.633
IRAC photometry
flux density [Jy]
rest frame wavelength [μm]

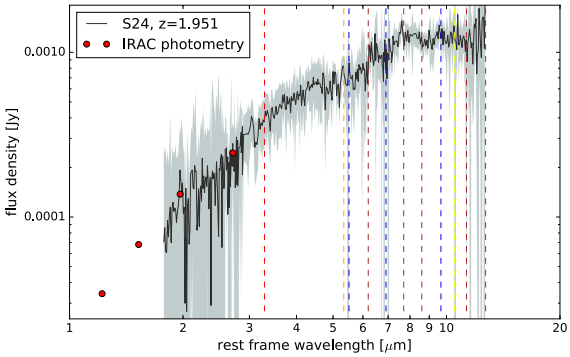
S24, z=1.951
IRAC photometry
flux density [Jy]
rest frame wavelength [μm]

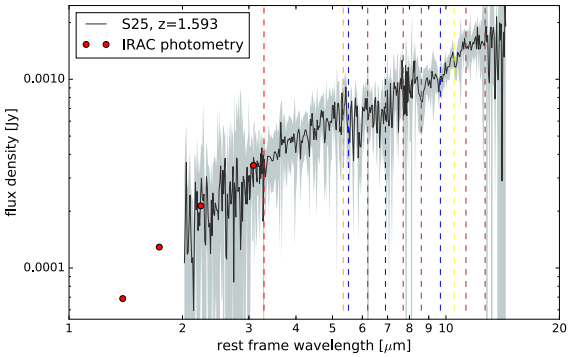
S25, z=1.593
IRAC photometry
flux density [Jy]
rest frame wavelength [μm]

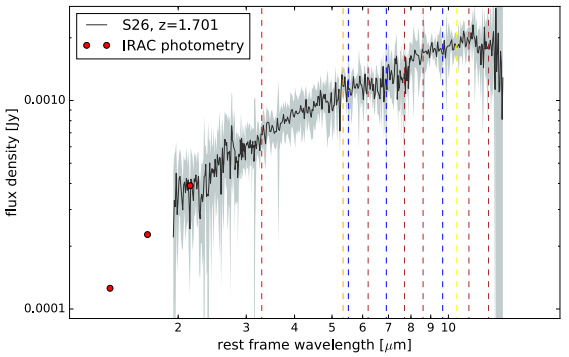
S26, z=1.701
IRAC photometry
flux density [Jy]
rest frame wavelength [μm]

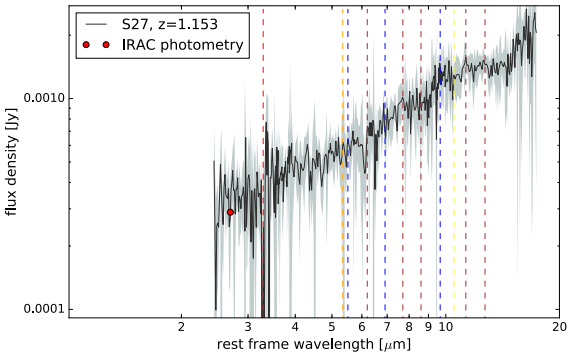
S27, z=1.153
IRAC photometry
flux density [Jy]
rest frame wavelength [μm]

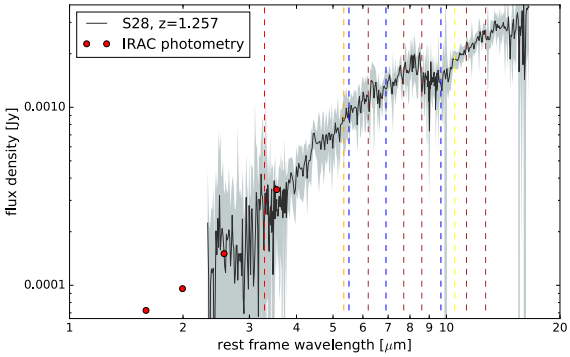
S28, z=1.257
IRAC photometry
flux density [Jy]
rest frame wavelength [μm]

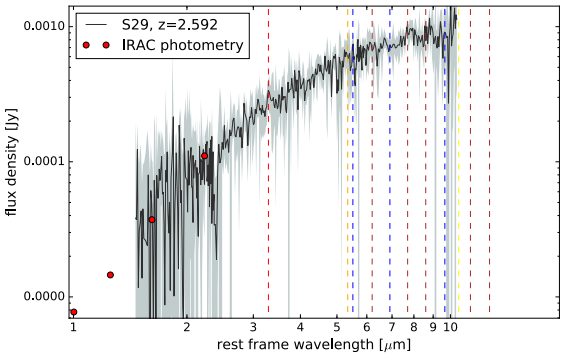
S29, z=2.592
IRAC photometry
flux density [Jy]
rest frame wavelength [μm]

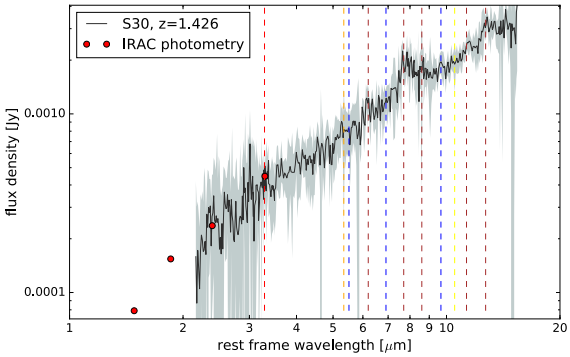
S30, z=1.426
IRAC photometry
flux density [Jy]
rest frame wavelength [μm]

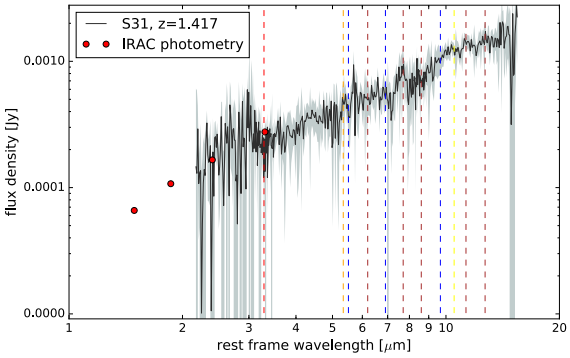
S31, z=1.417
IRAC photometry
flux density [Jy]
rest frame wavelength [μm]

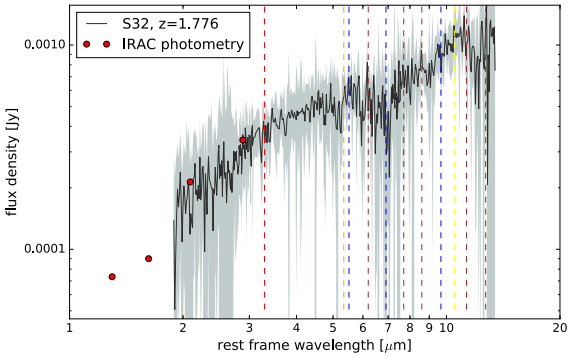
S32, z=1.776
IRAC photometry
flux density [Jy]
rest frame wavelength [μm]

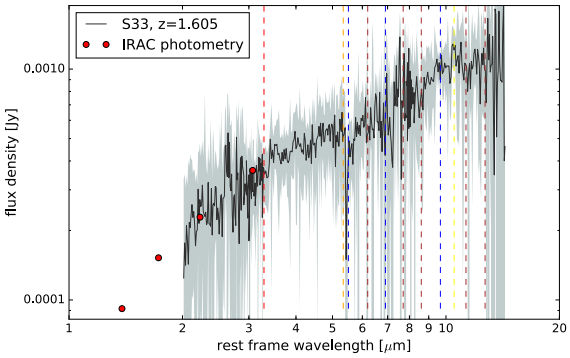
S33, z=1.605
IRAC photometry
flux density [Jy]
rest frame wavelength [μm]

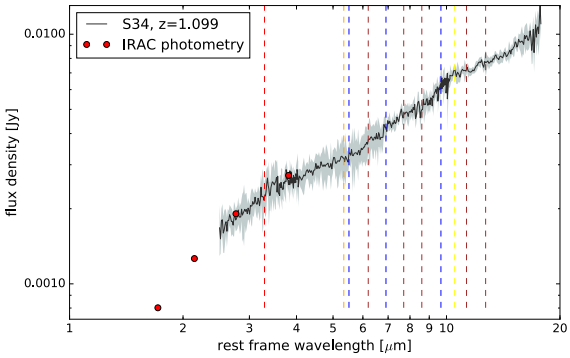
S34, z=1.099
IRAC photometry
flux density [Jy]
rest frame wavelength [μm]

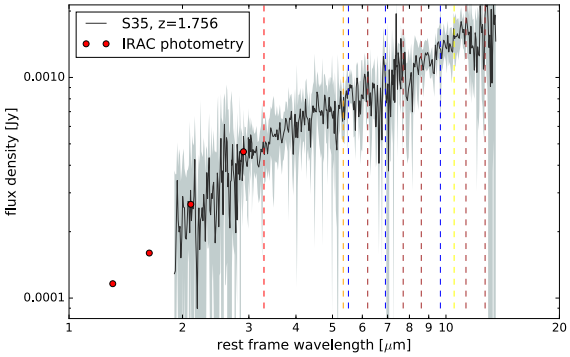
S35, z=1.756
IRAC photometry
flux density [Jy]
rest frame wavelength [μm]

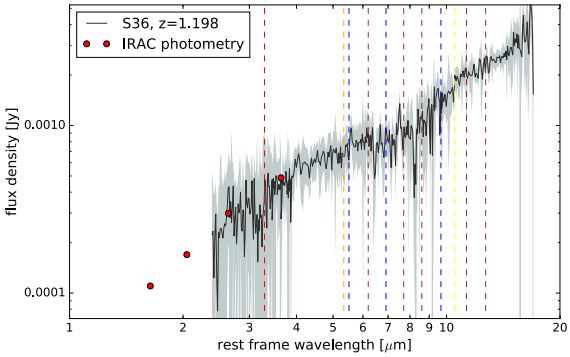
S36, z=1.198
IRAC photometry
flux density [Jy]
rest frame wavelength [μm]

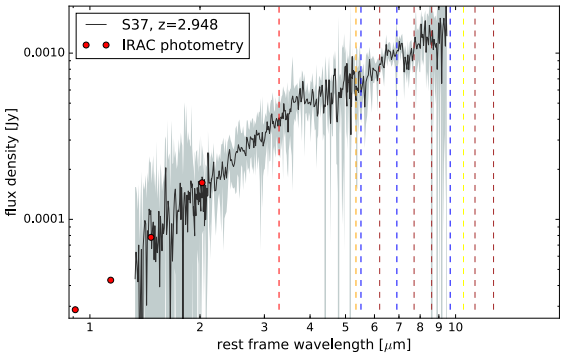
S37, z=2.948
IRAC photometry
flux density [Jy]
rest frame wavelength [μm]

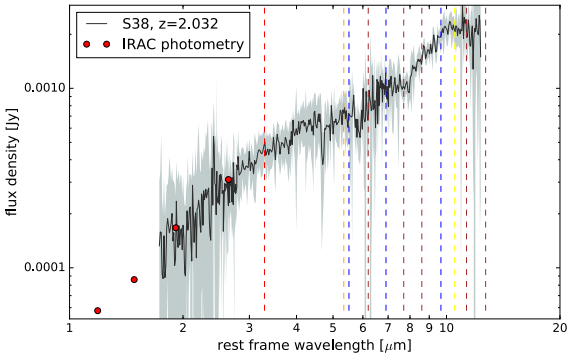
S38, z=2.032
IRAC photometry
flux density [Jy]
rest frame wavelength [μm]

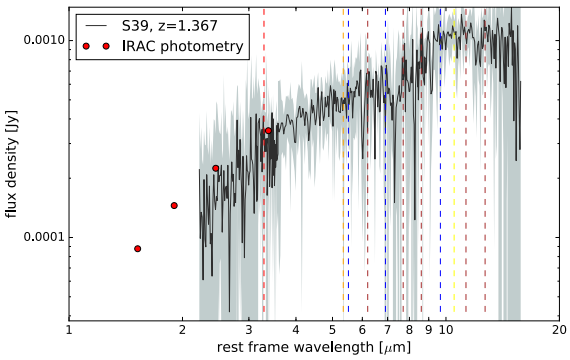
S39, z=1.367
IRAC photometry
flux density [Jy]
rest frame wavelength [μm]

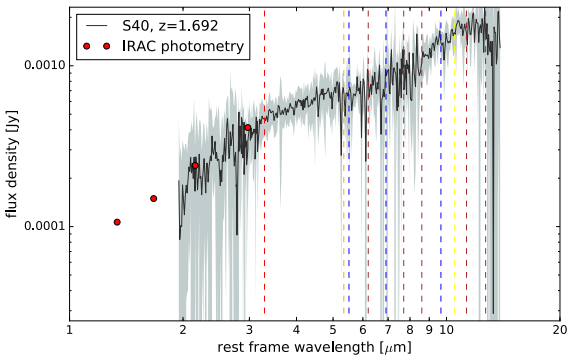
S40, z=1.692
IRAC photometry
flux density [Jy]
rest frame wavelength [μm]

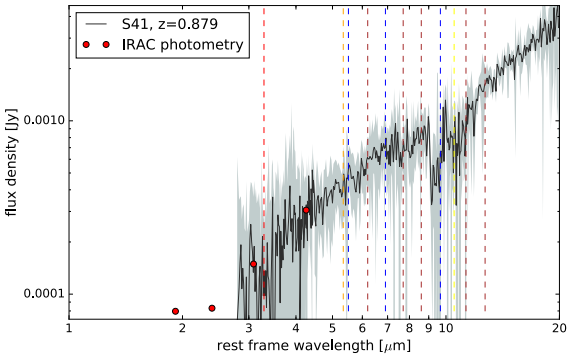
S41, z=0.879
IRAC photometry
flux density [Jy]
rest frame wavelength [μm]

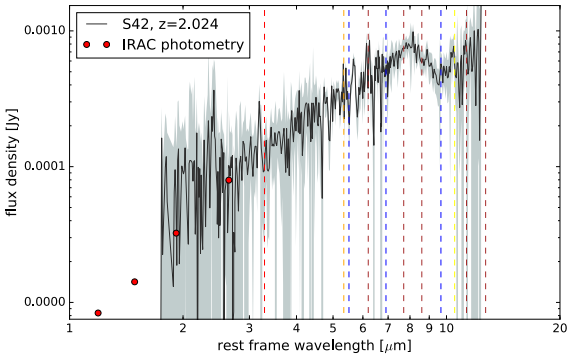
S42, z=2.024
IRAC photometry
flux density [Jy]
rest frame wavelength [μm]

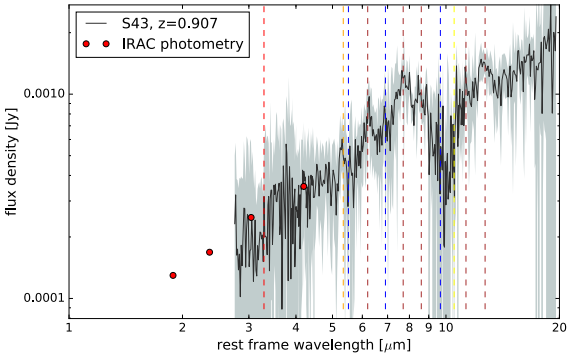
S43, z=0.907
IRAC photometry
flux density [Jy]
rest frame wavelength [μm]

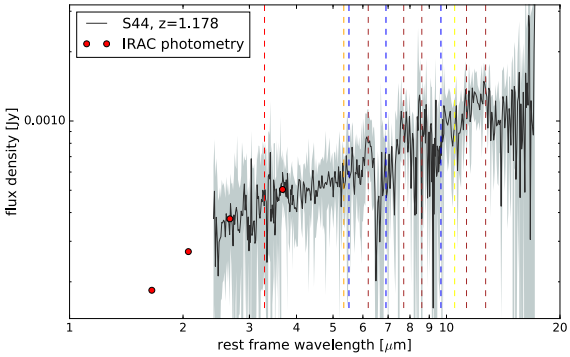
S44, z=1.178
IRAC photometry
flux density [Jy]
rest frame wavelength [μm]

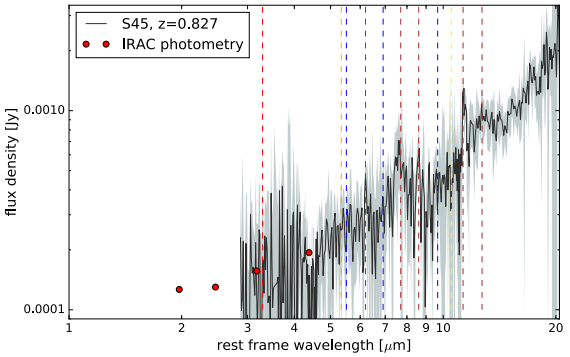
S45, z=0.827
IRAC photometry
flux density [Jy]
rest frame wavelength [μm]

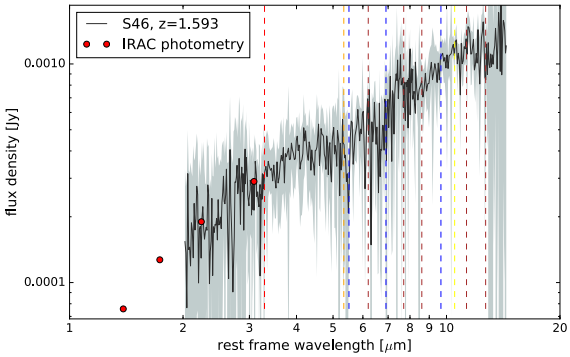
S46, z=1.593
IRAC photometry
flux density [Jy]
rest frame wavelength [μm]

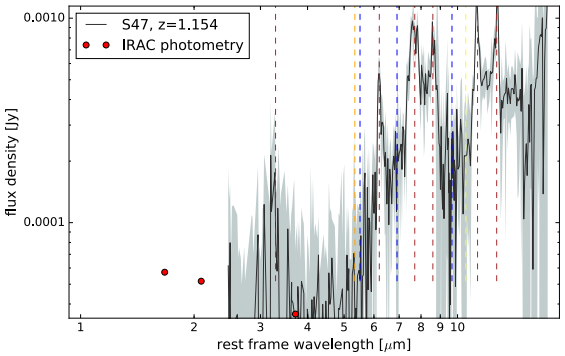
S47, z=1.154
IRAC photometry
flux density [Jy]
rest frame wavelength [μm]

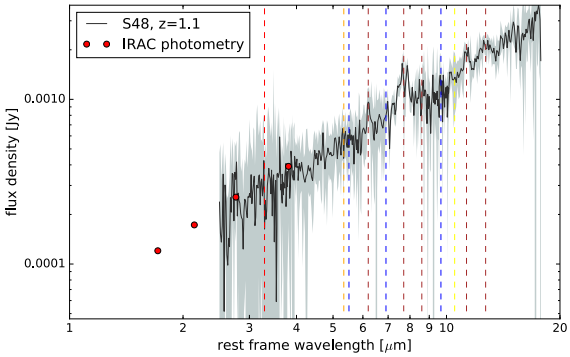
S48, z=1.1
IRAC photometry
flux density [Jy]
rest frame wavelength [μm]

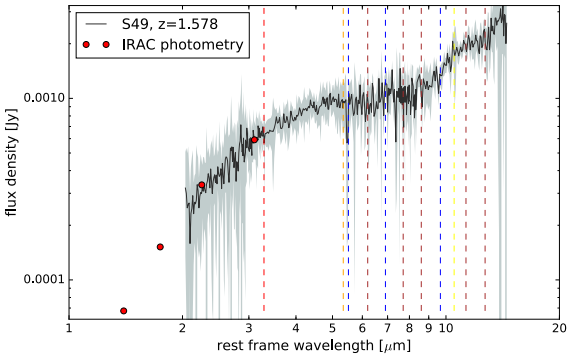
S49, z=1.578
IRAC photometry
flux density [Jy]
rest frame wavelength [μm]

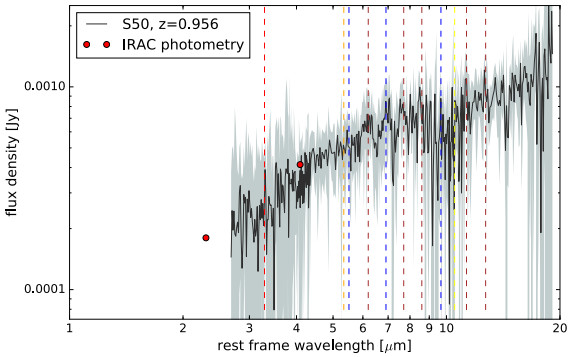
S50, z=0.956
IRAC photometry
flux density [Jy]
rest frame wavelength [μm]

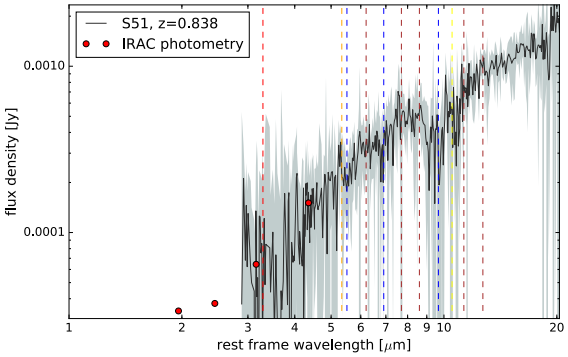
S51, z=0.838
IRAC photometry
flux density [Jy]
rest frame wavelength [μm]

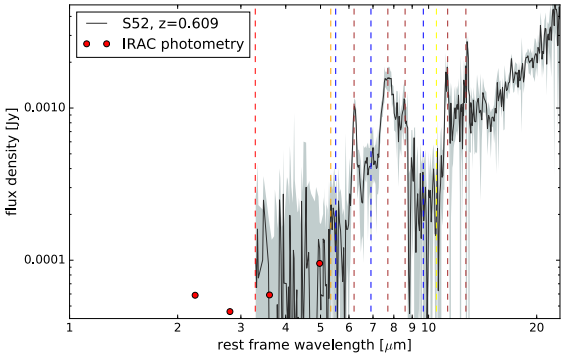
S52, z=0.609
IRAC photometry
flux density [Jy]
rest frame wavelength [μm]

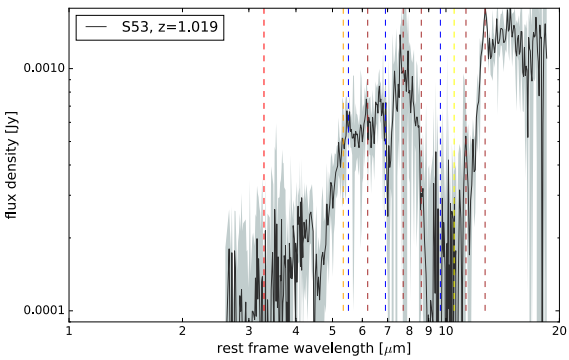
S53, z=1.019
flux density [Jy]
rest frame wavelength [μm]

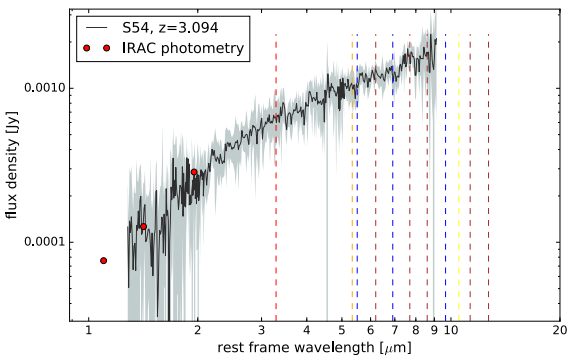
S54, z=3.094
IRAC photometry
flux density [Jy]
rest frame wavelength [μm]

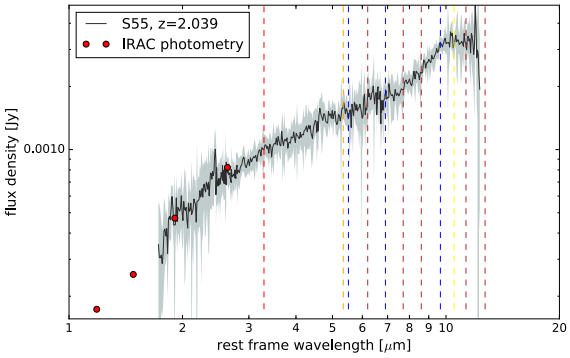
S55, z=2.039
IRAC photometry
flux density [Jy]
0.0010
rest frame wavelength [μm]

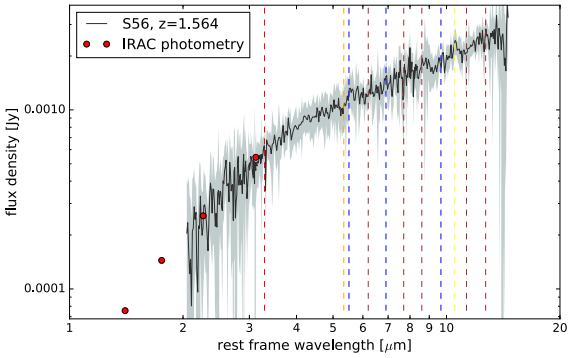
S56, z=1.564
IRAC photometry
flux density [Jy]
0.0010
0.0001
rest frame wavelength [μm]

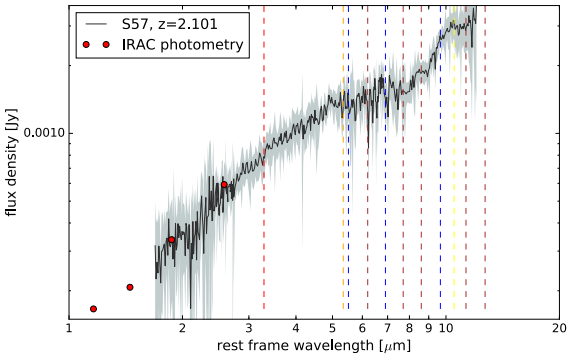
S57, z=2.101
IRAC photometry
flux density [Jy]
0.0010
rest frame wavelength [μm]

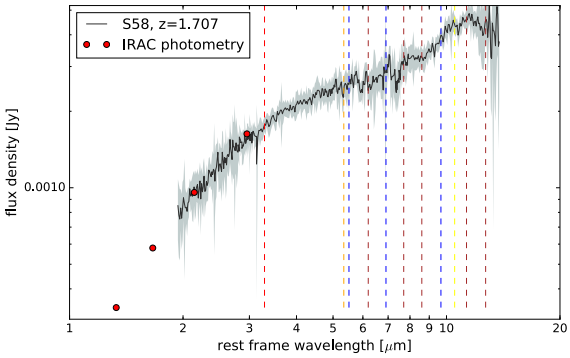
S58, z=1.707
IRAC photometry
flux density [Jy]
0.0010
rest frame wavelength [μm]

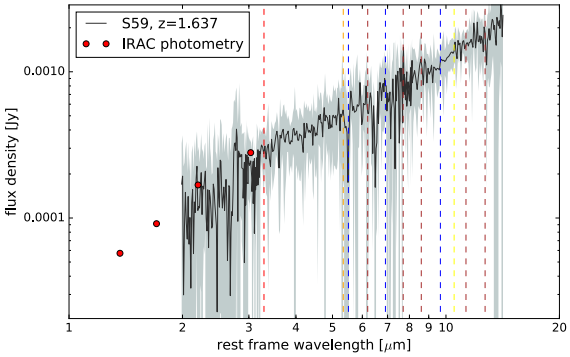
S59, z=1.637
IRAC photometry
flux density [Jy]
0.0010
0.0001
rest frame wavelength [μm]

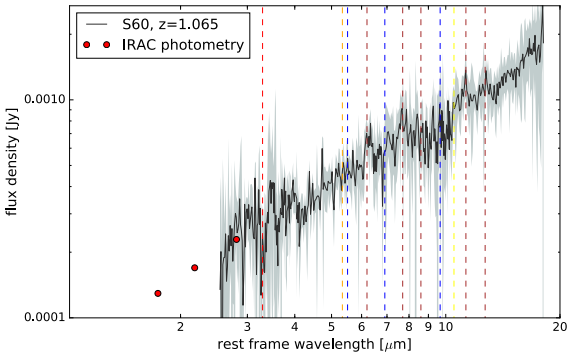
S60, z=1.065
IRAC photometry
flux density [Jy]
0.0010
0.0001
rest frame wavelength [μm]

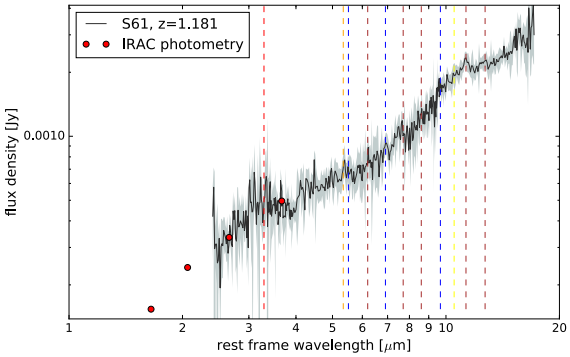
S61, z=1.181
IRAC photometry
flux density [Jy]
0.0010
rest frame wavelength [μm]

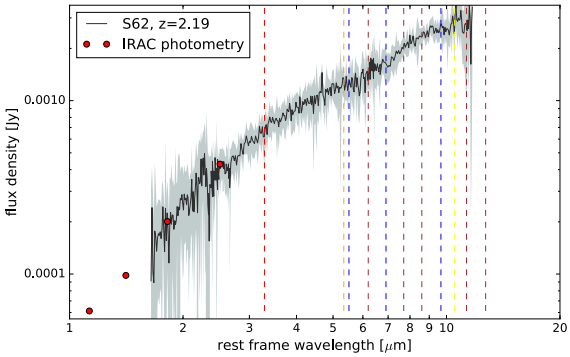
S62, z=2.19
IRAC photometry
flux density [Jy]
0.0010
0.0001
rest frame wavelength [μm]

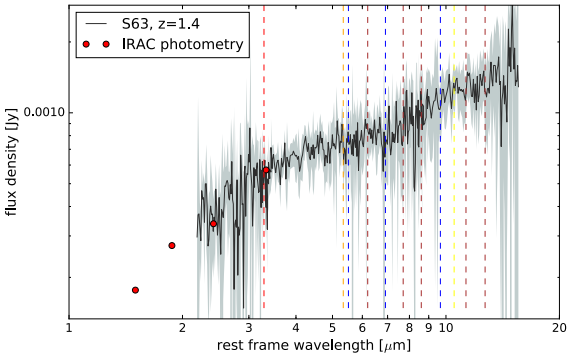
S63, z=1.4
IRAC photometry
flux density [Jy]
0.0010
rest frame wavelength [μm]

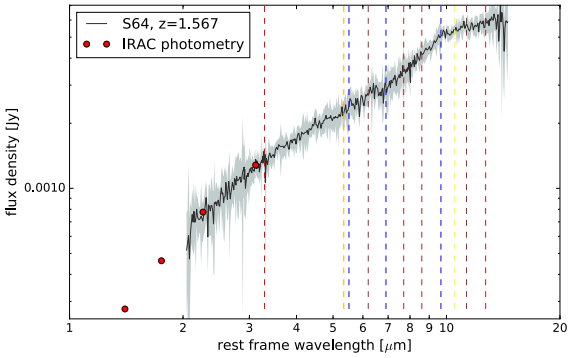
S64, z=1.567
IRAC photometry
flux density [Jy]
0.0010
rest frame wavelength [μm]

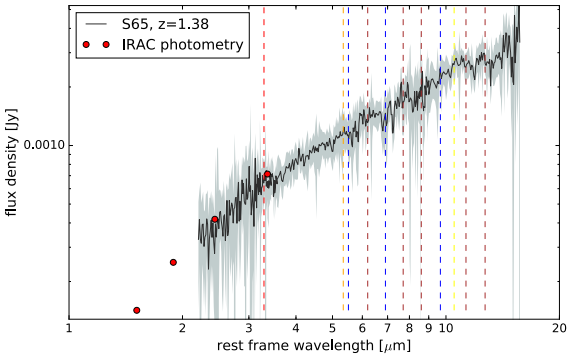
S65, z=1.38
IRAC photometry
flux density [Jy]
0.0010
rest frame wavelength [μm]

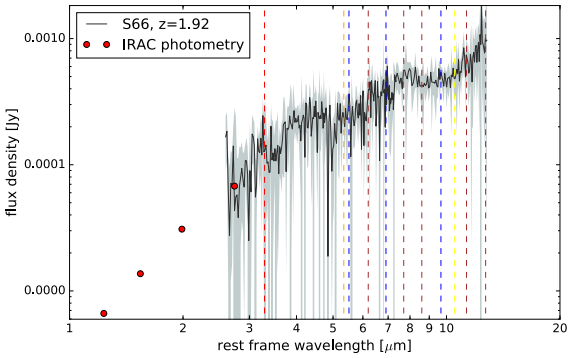
S66, z=1.92
IRAC photometry
flux density [Jy]
0.0010
0.0001
0.0000
rest frame wavelength [μm]

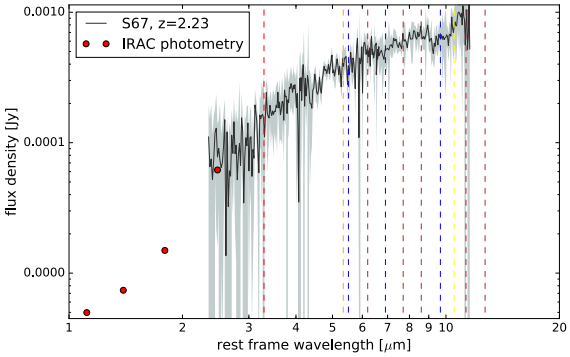
S67, z=2.23
IRAC photometry
flux density [Jy]
0.0010
0.0001
0.0000
rest frame wavelength [μm]

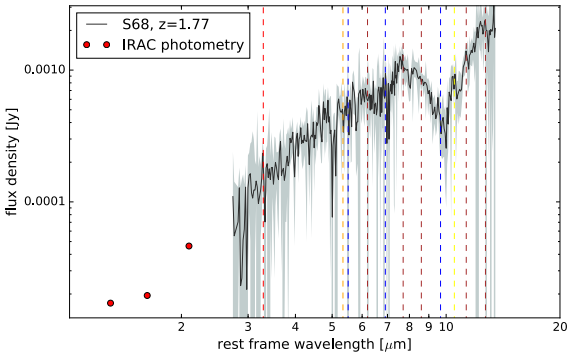
S68, z=1.77
IRAC photometry
flux density [Jy]
0.0010
0.0001
rest frame wavelength [μm]

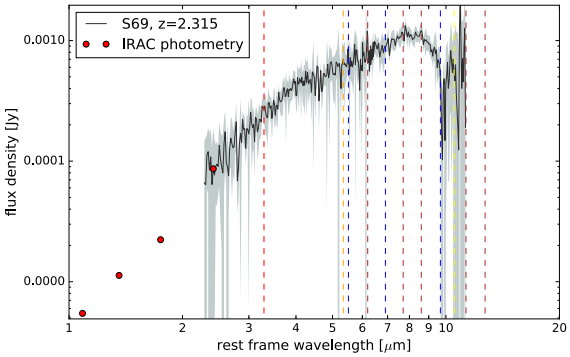
S69, z=2.315
IRAC photometry
flux density [Jy]
0.0010
0.0001
0.0000
rest frame wavelength [μm]

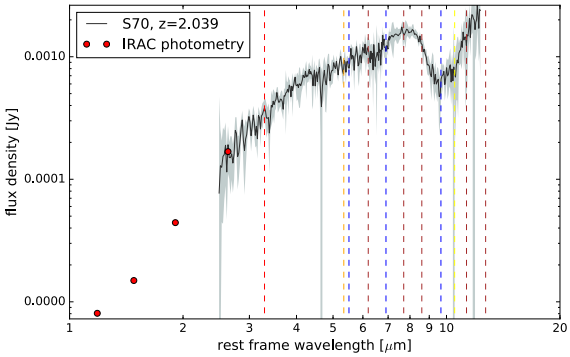
S70, z=2.039
IRAC photometry
flux density [Jy]
0.0010
0.0001
0.0000
rest frame wavelength [μm]

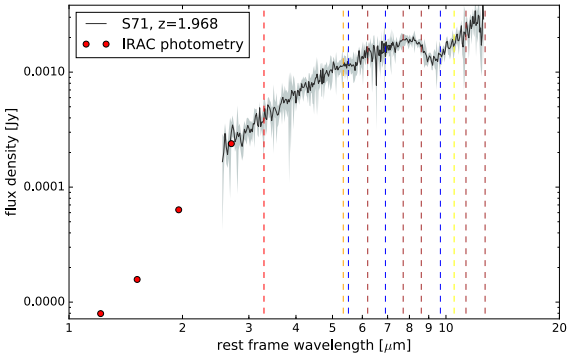
S71, z=1.968
IRAC photometry
flux density [Jy]
rest frame wavelength [μm]

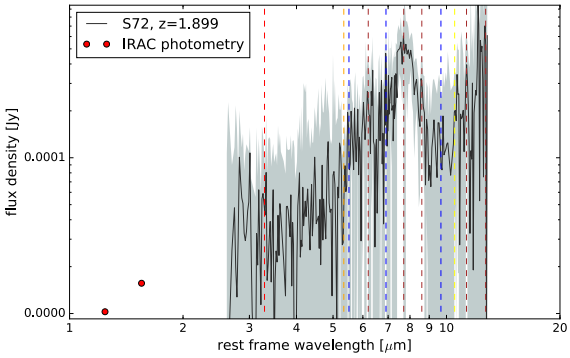
S72, z=1.899
IRAC photometry
flux density [Jy]
rest frame wavelength [μm]

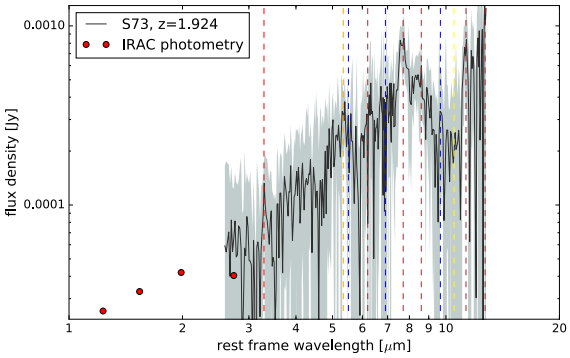
S73, z=1.924
IRAC photometry
flux density [Jy]
rest frame wavelength [μm]

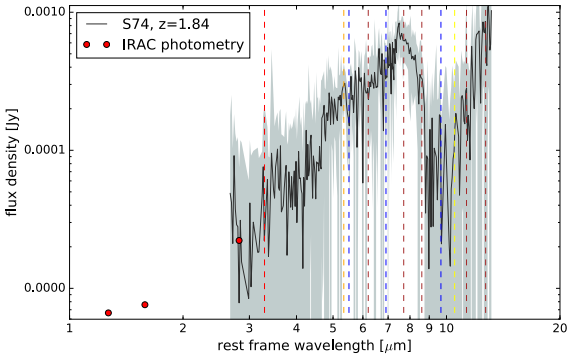
S74, z=1.84
IRAC photometry
flux density [Jy]
rest frame wavelength [μm]

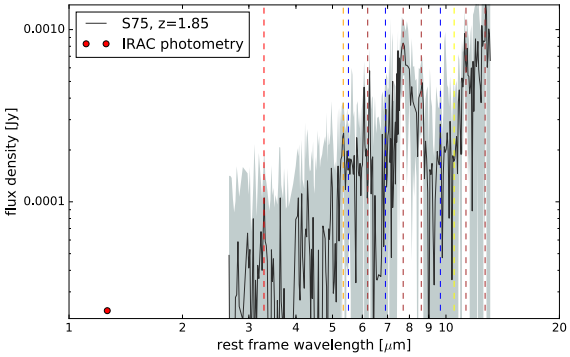
S75, z=1.85
IRAC photometry
flux density [Jy]
rest frame wavelength [μm]

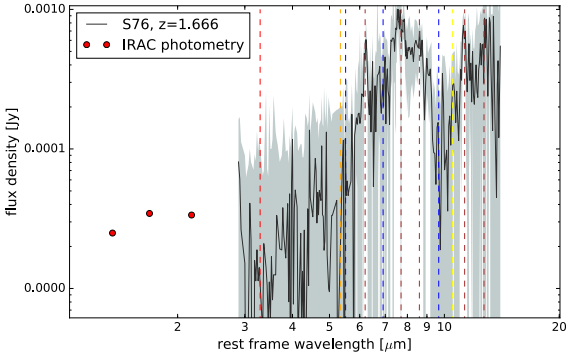
S76, z=1.666
IRAC photometry
flux density [Jy]
rest frame wavelength [μm]

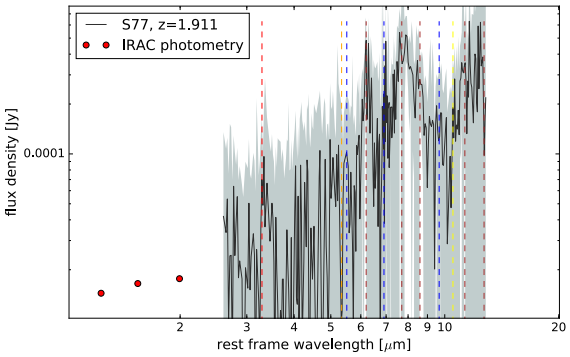
S77, z=1.911
IRAC photometry
flux density [Jy]
rest frame wavelength [μm]

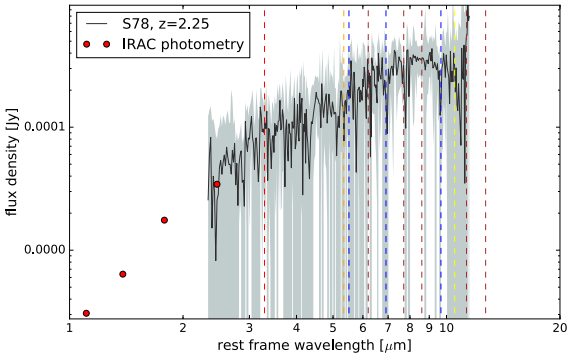
S78, z=2.25
IRAC photometry
flux density [Jy]
rest frame wavelength [μm]

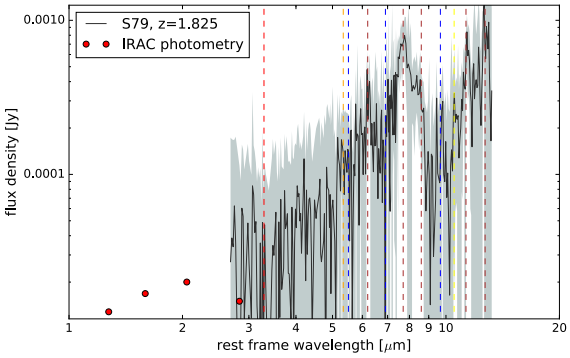
S79, z=1.825
IRAC photometry
flux density [Jy]
rest frame wavelength [μm]

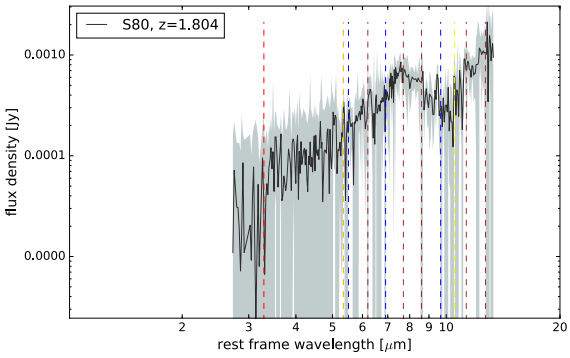
S80, z=1.804
flux density [Jy]
rest frame wavelength [μm]

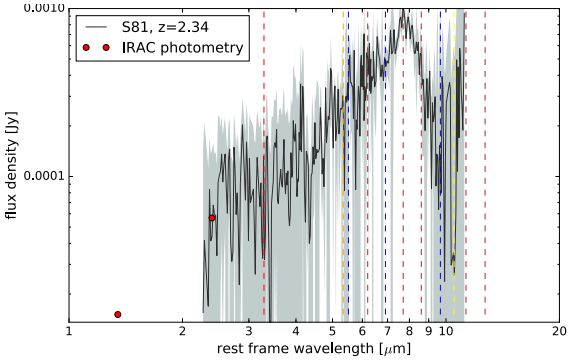
S81, z=2.34
IRAC photometry
flux density [Jy]
rest frame wavelength [μm]

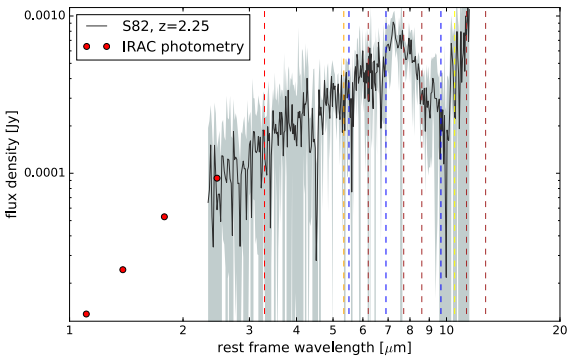
S82, z=2.25
IRAC photometry
flux density [Jy]
rest frame wavelength [μm]

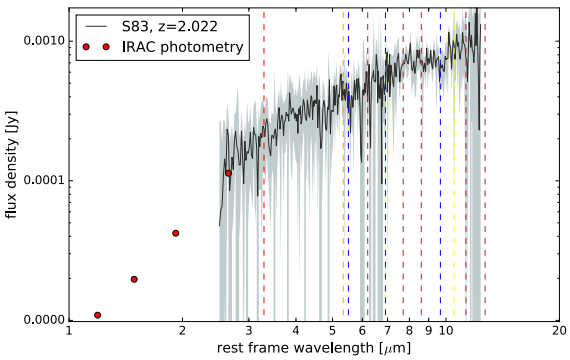
S83, z=2.022
IRAC photometry
flux density [Jy]
rest frame wavelength [μm]

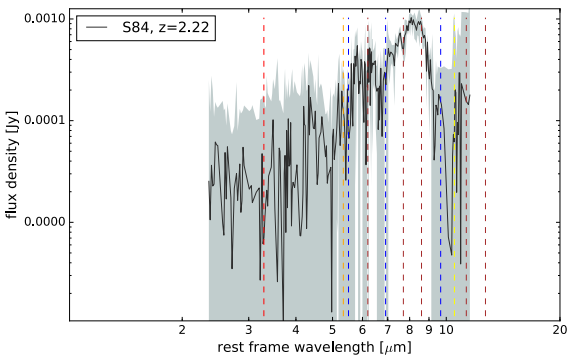
S84, z=2.22
flux density [Jy]
rest frame wavelength [μm]

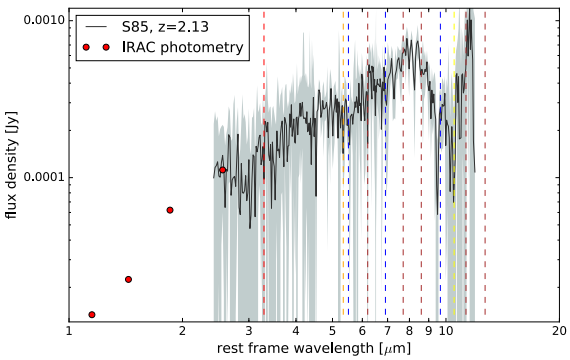
S85, z=2.13
IRAC photometry
flux density [Jy]
rest frame wavelength [μm]

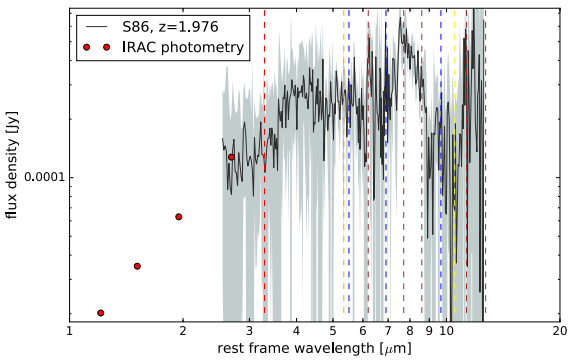
S86, z=1.976
IRAC photometry
flux density [Jy]
rest frame wavelength [μm]

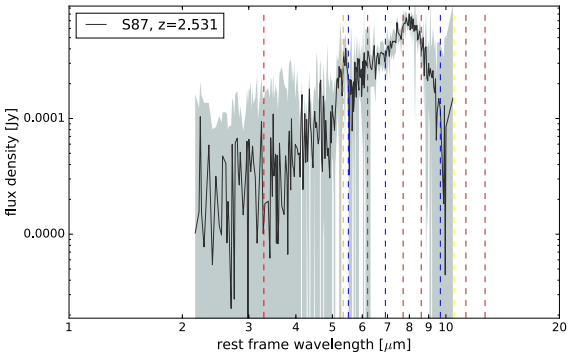
S87, z=2.531
flux density [Jy]
rest frame wavelength [μm]

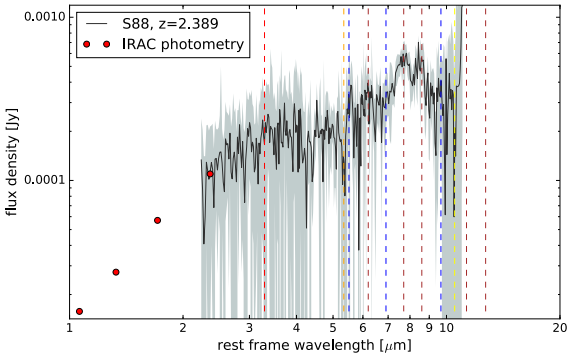
S88, z=2.389
IRAC photometry
flux density [Jy]
rest frame wavelength [μm]

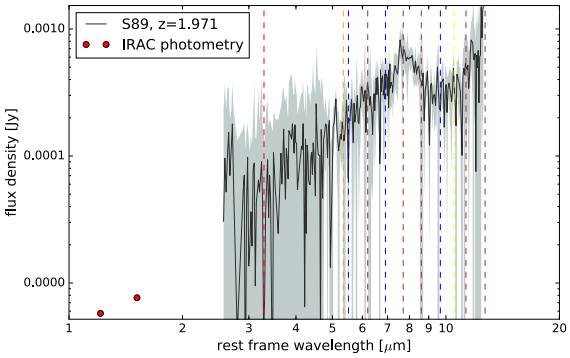
S89, z=1.971
IRAC photometry
flux density [Jy]
rest frame wavelength [μm]

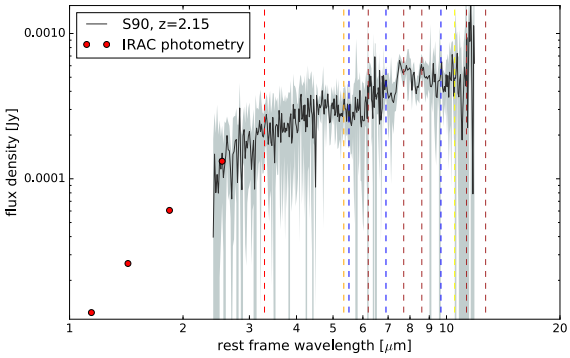
S90, z=2.15
IRAC photometry
flux density [Jy]
rest frame wavelength [μm]

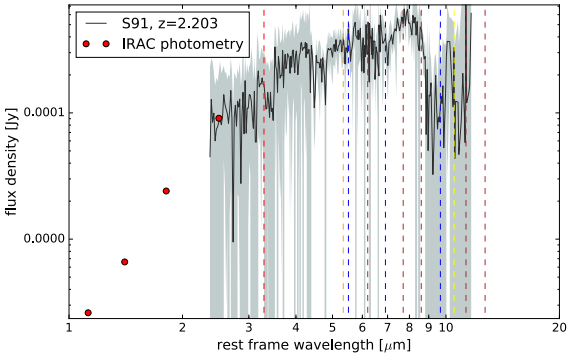
S91, z=2.203
IRAC photometry
flux density [Jy]
rest frame wavelength [μm]

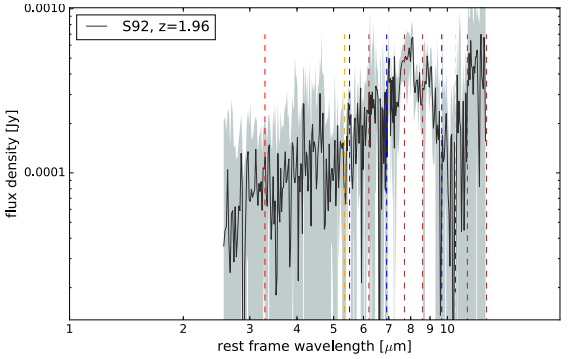
S92, z=1.96
flux density [Jy]
rest frame wavelength [μm]

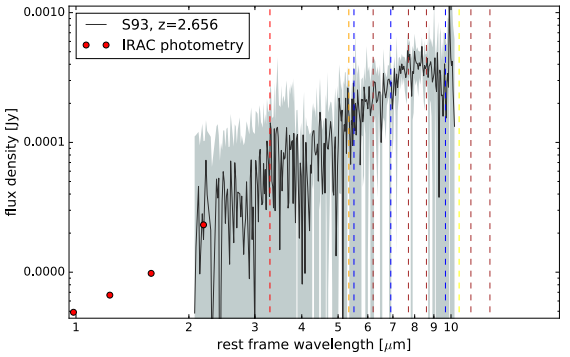
S93, z=2.656
IRAC photometry
flux density [Jy]
rest frame wavelength [μm]

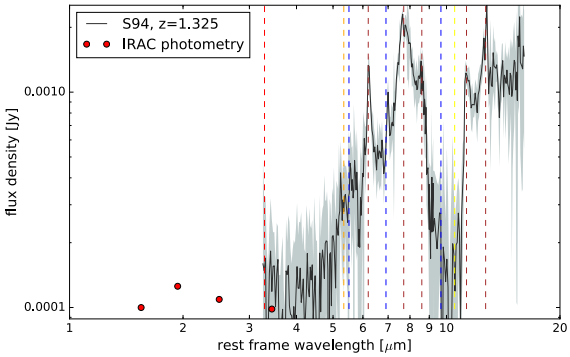
S94, z=1.325
IRAC photometry
flux density [Jy]
rest frame wavelength [μm]

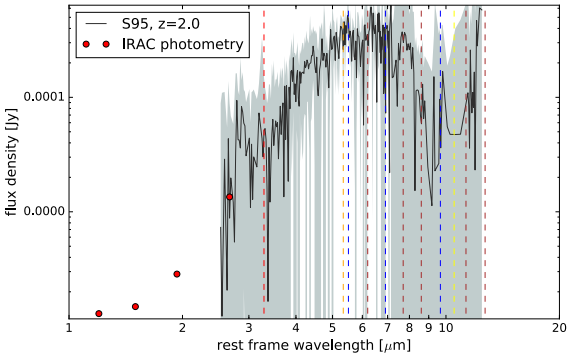
S95, z=2.0
IRAC photometry
flux density [Jy]
0.0001
0.0000
1
2
3
4
5
6
7
8
9
10
20
rest frame wavelength [μm]

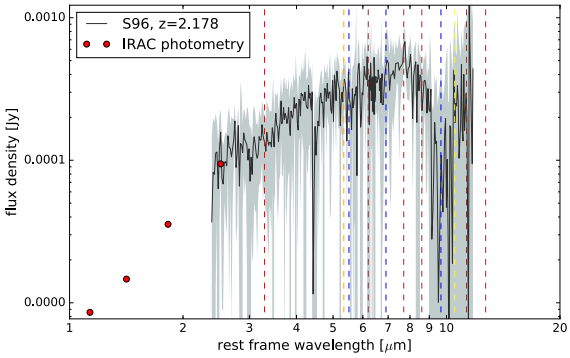
S96, z=2.178
IRAC photometry
flux density [Jy]
0.0010
0.0001
0.0000
1
2
3
4
5
6
7
8
9
10
20
rest frame wavelength [μm]

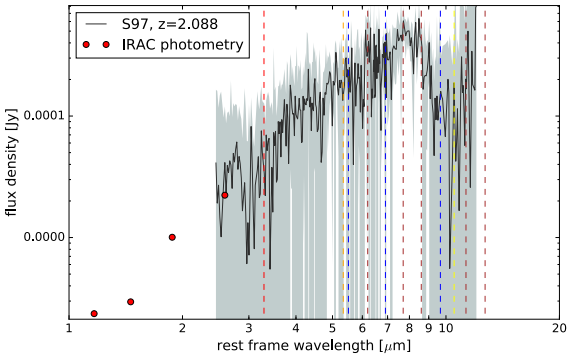
S97, z=2.088
IRAC photometry
flux density [Jy]
0.0001
0.0000
1
2
3
4
5
6
7
8
9
10
20
rest frame wavelength [μm]

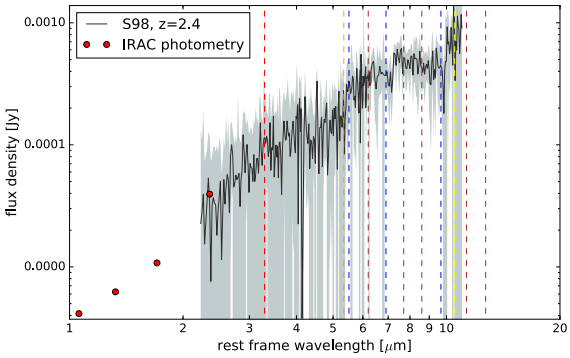
S98, z=2.4
IRAC photometry
flux density [Jy]
0.0010
0.0001
0.0000
1
2
3
4
5
6
7
8
9
10
20
rest frame wavelength [μm]

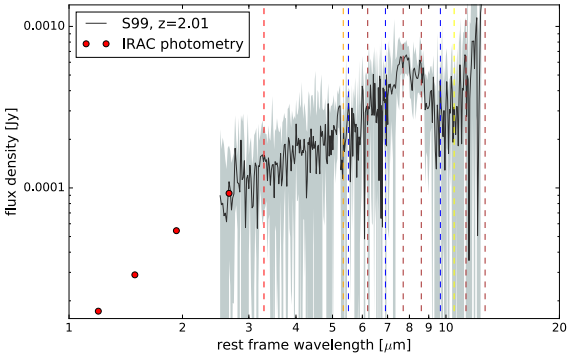
S99, z=2.01
IRAC photometry
flux density [Jy]
0.0010
0.0001
1
2
3
4
5
6
7
8
9
10
20
rest frame wavelength [μm]

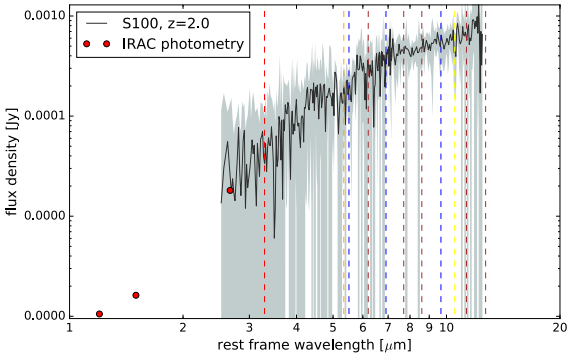
S100, z=2.0
IRAC photometry
flux density [Jy]
0.0010
0.0001
0.0000
1
2
3
4
5
6
7
8
9
10
20
rest frame wavelength [μm]

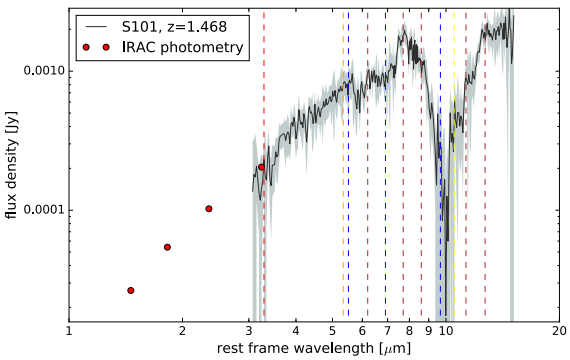
S101, z=1.468
IRAC photometry
flux density [Jy]
0.0010
0.0001
1
2
3
4
5
6
7
8
9
10
20
rest frame wavelength [μm]

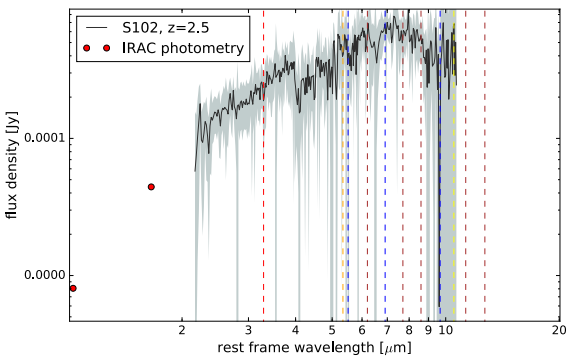
S102, z=2.5
IRAC photometry
flux density [Jy]
0.0001
0.0000
2
3
4
5
6
7
8
9
10
20
rest frame wavelength [μm]

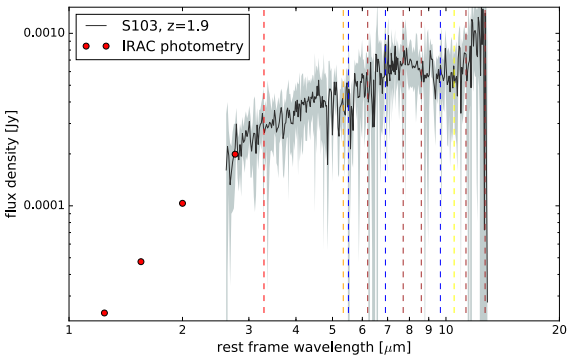
S103, z=1.9
IRAC photometry
flux density [Jy]
rest frame wavelength [μm]

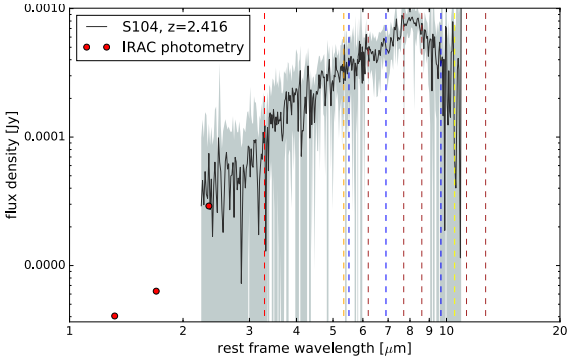
S104, z=2.416
IRAC photometry
flux density [Jy]
rest frame wavelength [μm]

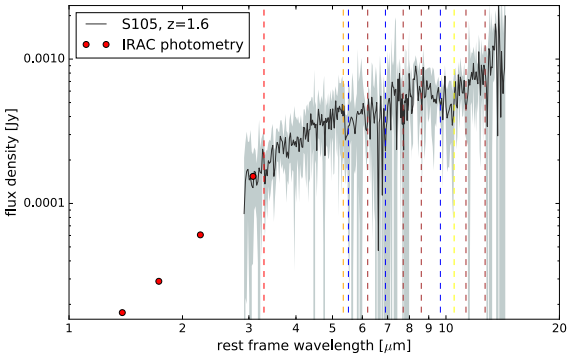
S105, z=1.6
IRAC photometry
flux density [Jy]
rest frame wavelength [μm]

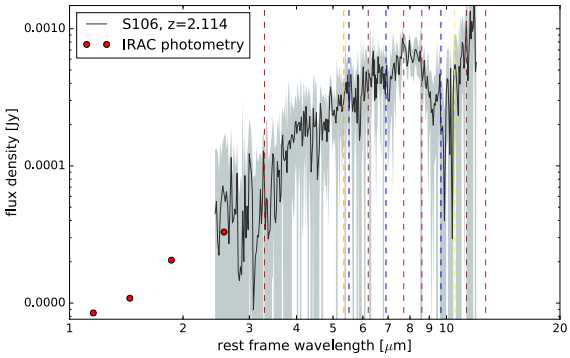
S106, z=2.114
IRAC photometry
flux density [Jy]
rest frame wavelength [μm]

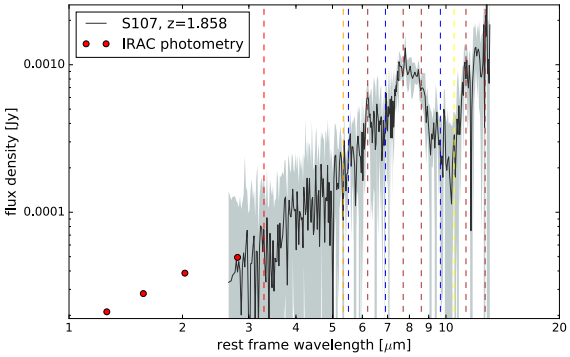
S107, z=1.858
IRAC photometry
flux density [Jy]
rest frame wavelength [μm]

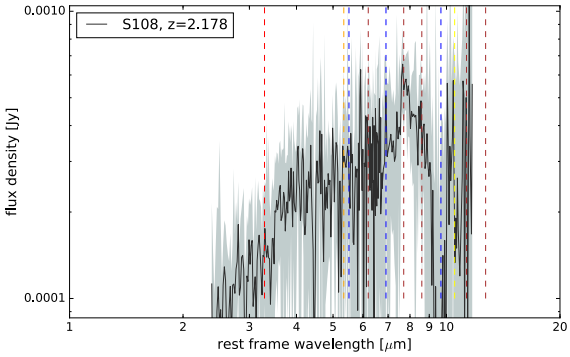
S108, z=2.178
flux density [Jy]
rest frame wavelength [μm]

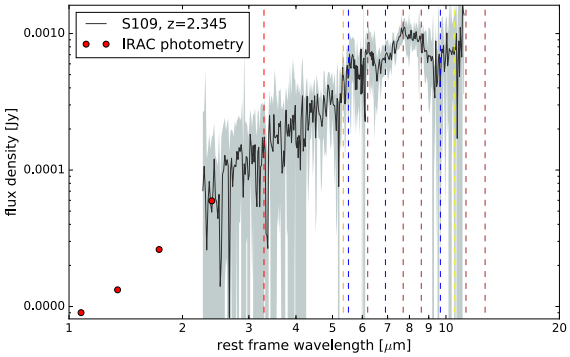
S109, z=2.345
IRAC photometry
flux density [Jy]
rest frame wavelength [μm]

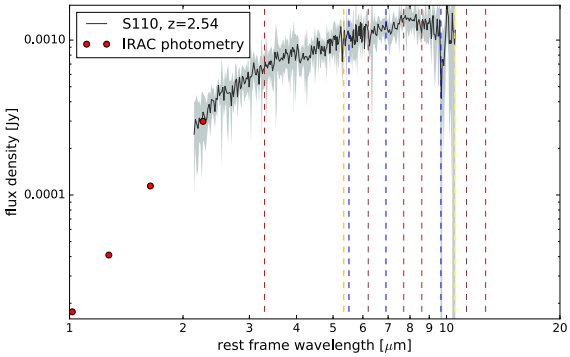
S110, z=2.54
IRAC photometry
flux density [Jy]
rest frame wavelength [μm]

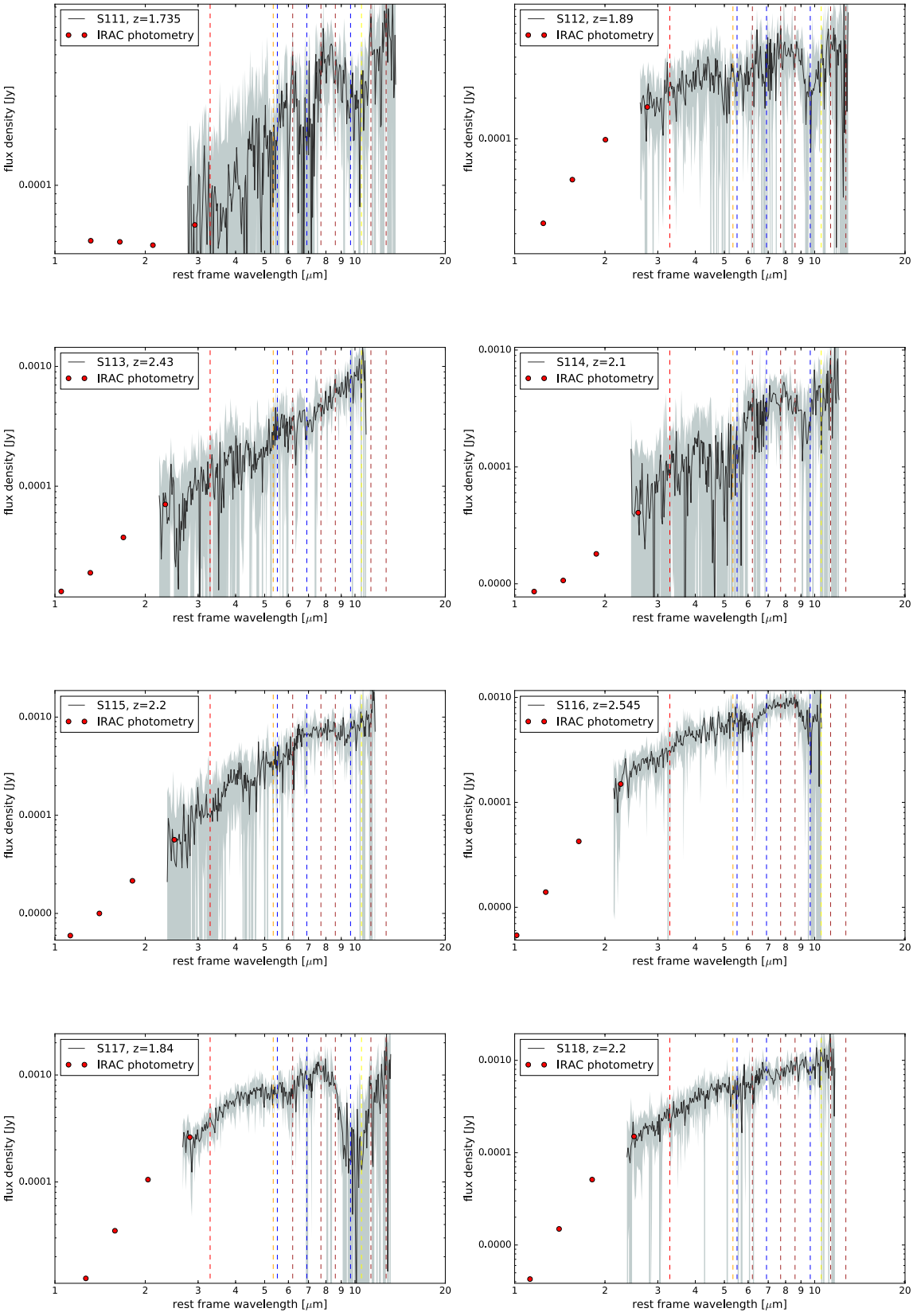
S111, z=1.735
IRAC photometry
S112, z=1.89
IRAC photometry
S113, z=2.43
IRAC photometry
S114, z=2.1
IRAC photometry
S115, z=2.2
IRAC photometry
S116, z=2.545
IRAC photometry
S117, z=1.84
IRAC photometry
S118, z=2.2
IRAC photometry
flux density [Jy]
rest frame wavelength [μm]

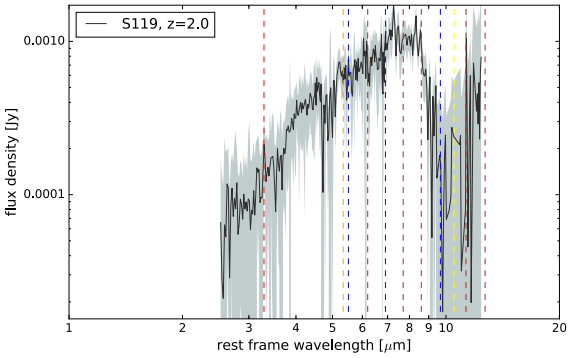
S119, z=2.0
flux density [Jy]
rest frame wavelength [μm]

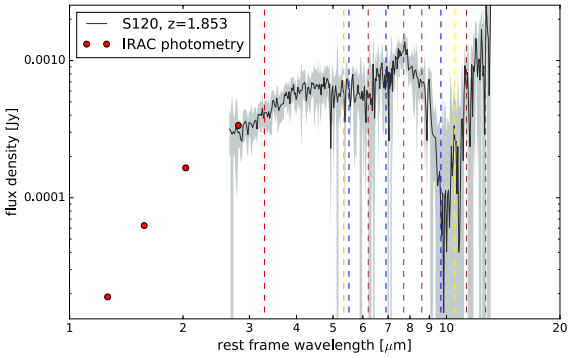
S120, z=1.853
IRAC photometry
flux density [Jy]
rest frame wavelength [μm]

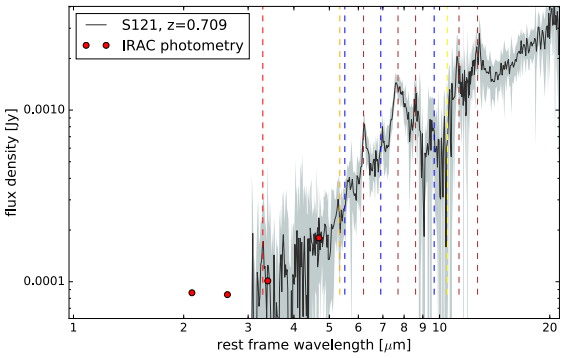
S121, z=0.709
IRAC photometry
flux density [Jy]
rest frame wavelength [μm]

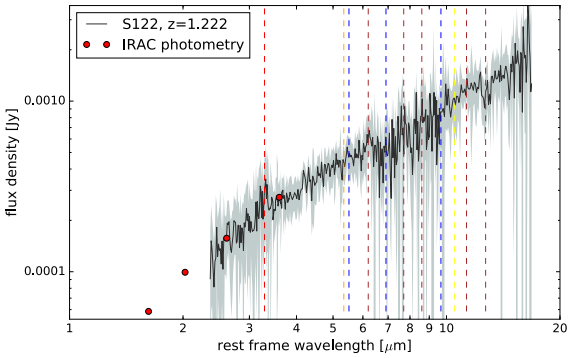
S122, z=1.222
IRAC photometry
flux density [Jy]
rest frame wavelength [μm]

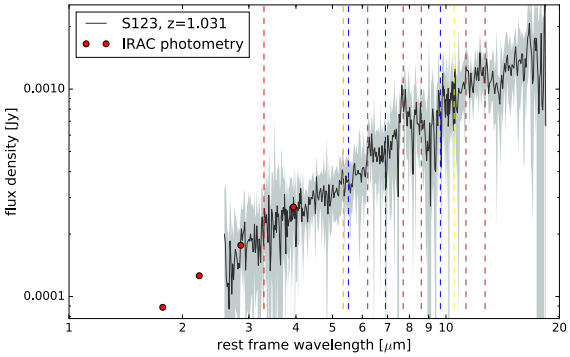
S123, z=1.031
IRAC photometry
flux density [Jy]
rest frame wavelength [μm]

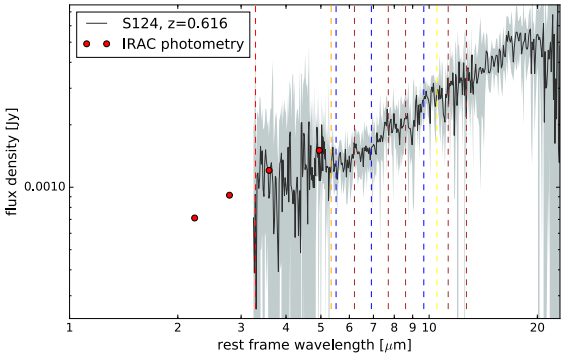
S124, z=0.616
IRAC photometry
flux density [Jy]
rest frame wavelength [μm]

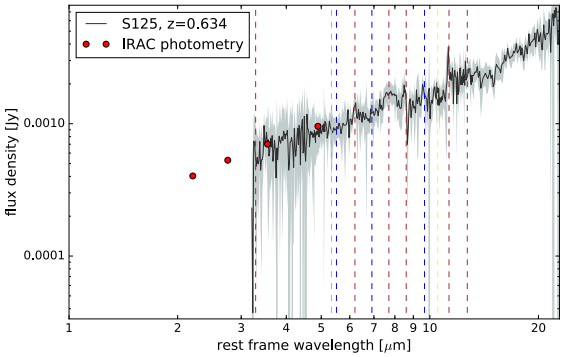
S125, z=0.634
IRAC photometry
flux density [Jy]
rest frame wavelength [μm]

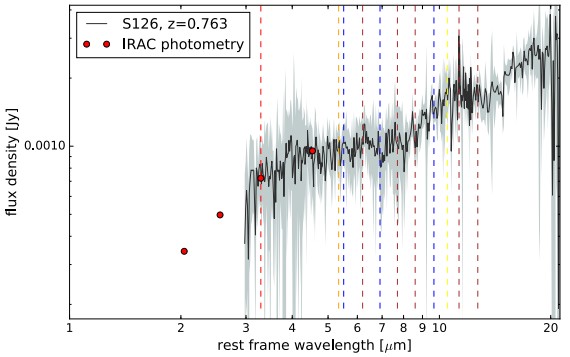
S126, z=0.763
IRAC photometry
flux density [Jy]
rest frame wavelength [μm]

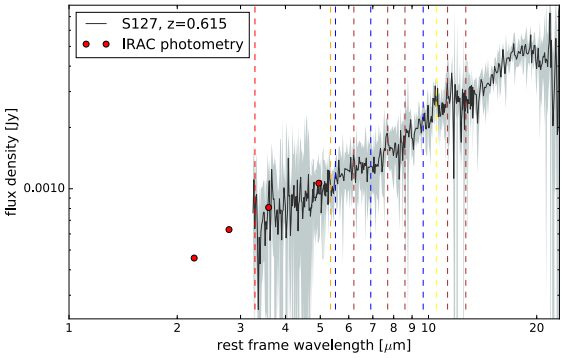
S127, z=0.615
IRAC photometry
flux density [Jy]
0.0010
rest frame wavelength [μm]

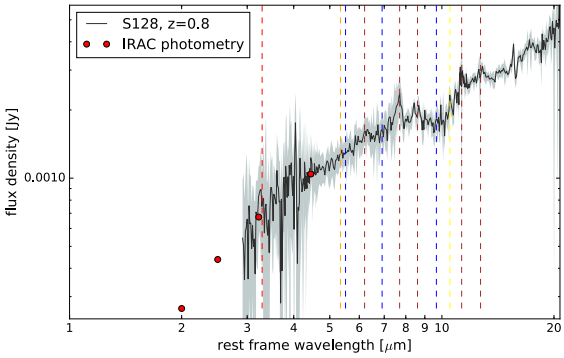
S128, z=0.8
IRAC photometry
flux density [Jy]
0.0010
rest frame wavelength [μm]

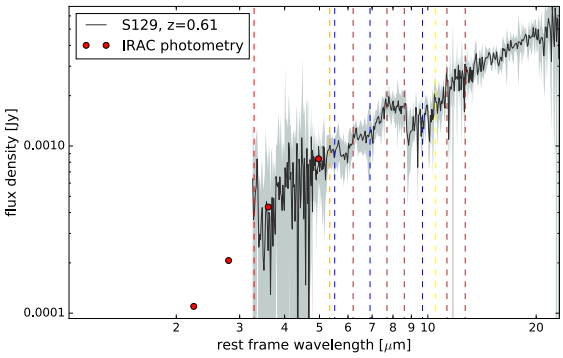
S129, z=0.61
IRAC photometry
flux density [Jy]
0.0010
0.0001
rest frame wavelength [μm]

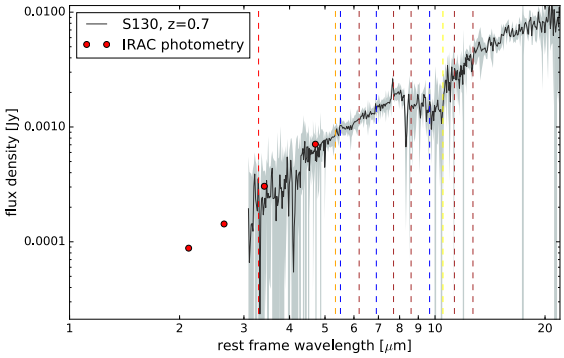
S130, z=0.7
IRAC photometry
flux density [Jy]
0.0100
0.0010
0.0001
rest frame wavelength [μm]

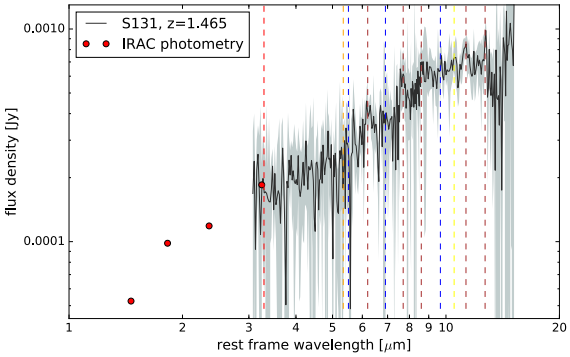
S131, z=1.465
IRAC photometry
flux density [Jy]
0.0010
0.0001
rest frame wavelength [μm]

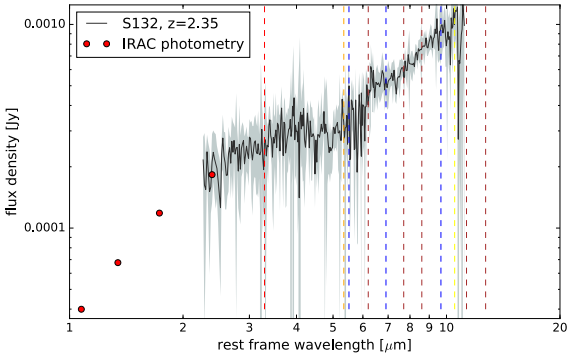
S132, z=2.35
IRAC photometry
flux density [Jy]
0.0010
0.0001
rest frame wavelength [μm]

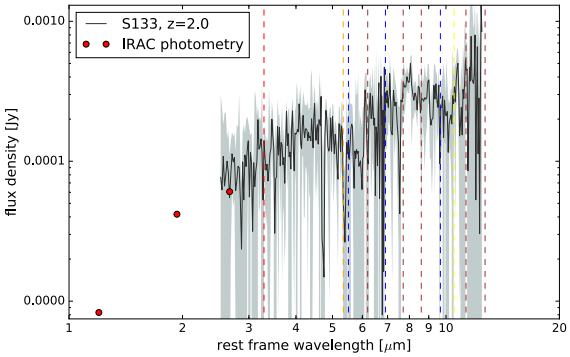
S133, z=2.0
IRAC photometry
flux density [Jy]
0.0010
0.0001
0.0000
rest frame wavelength [μm]

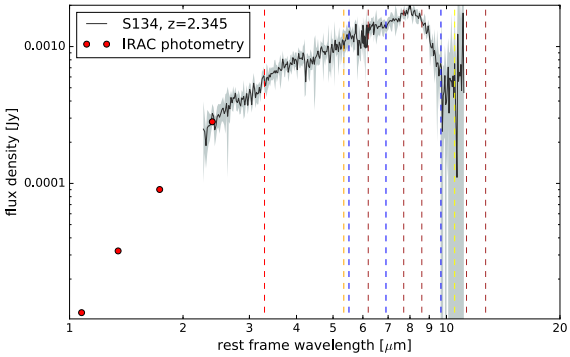
S134, z=2.345
IRAC photometry
flux density [Jy]
0.0010
0.0001
rest frame wavelength [μm]

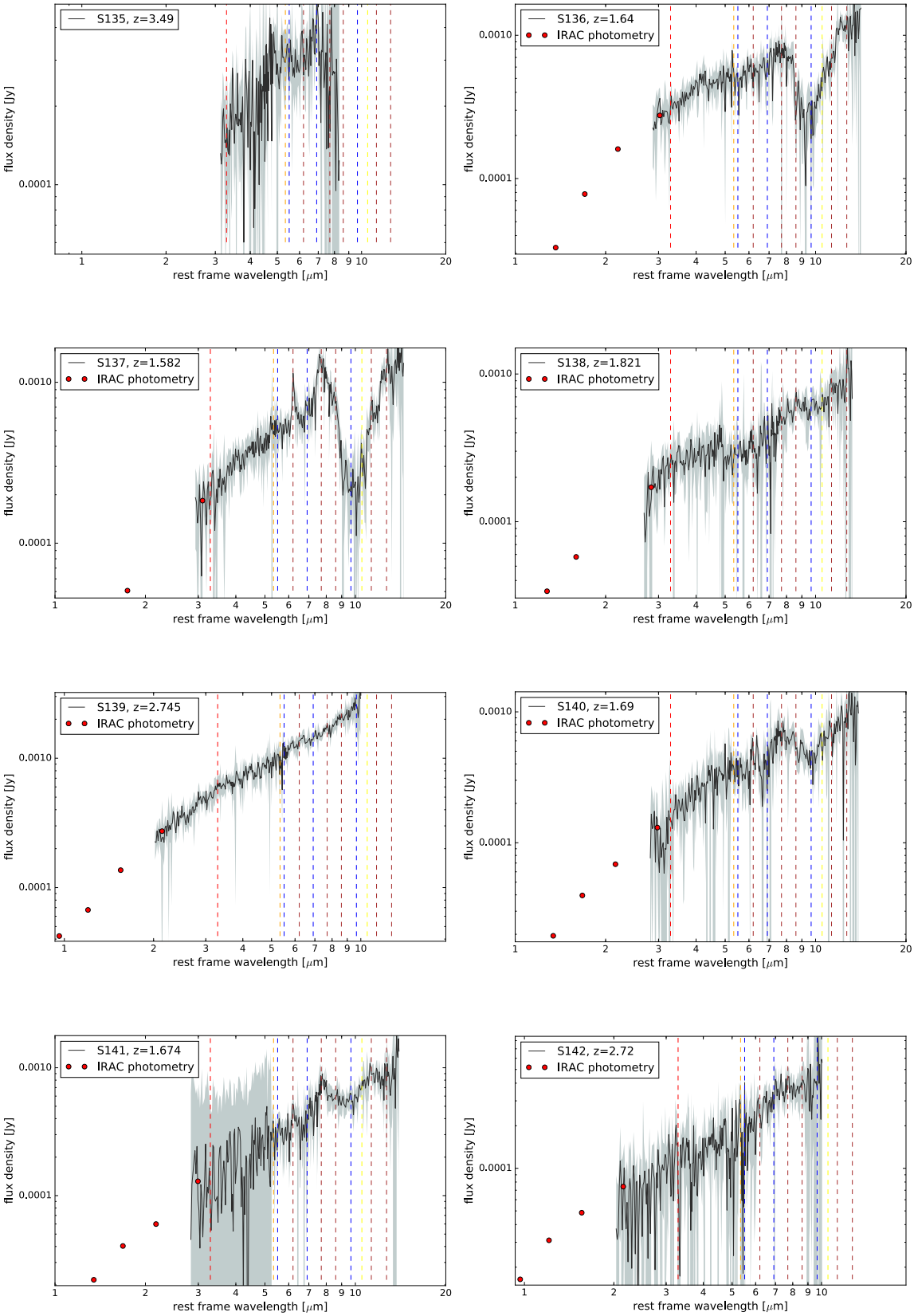
S135, z=3.49
S136, z=1.64
IRAC photometry
S137, z=1.582
IRAC photometry
S138, z=1.821
IRAC photometry
S139, z=2.745
IRAC photometry
S140, z=1.69
IRAC photometry
S141, z=1.674
IRAC photometry
S142, z=2.72
IRAC photometry
flux density [Jy]
rest frame wavelength [μm]

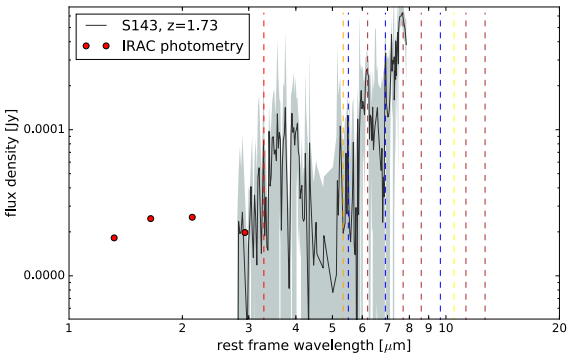
S143, z=1.73
IRAC photometry
flux density [Jy]
rest frame wavelength [μm]

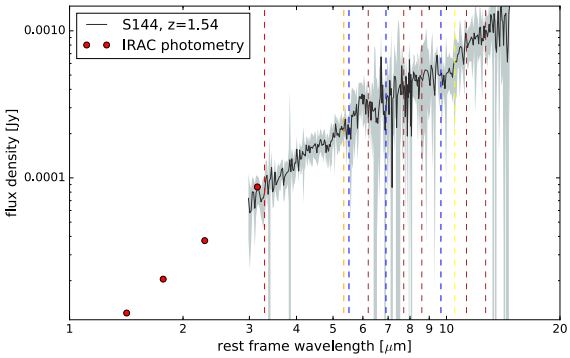
S144, z=1.54
IRAC photometry
flux density [Jy]
rest frame wavelength [μm]

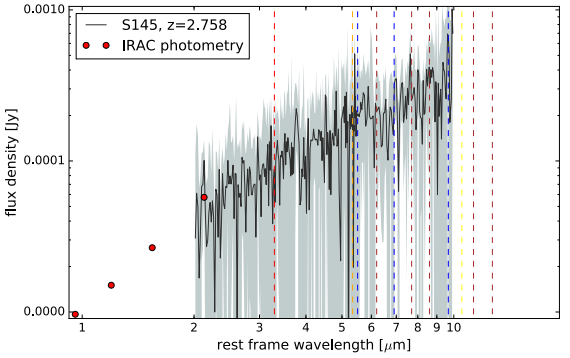
S145, z=2.758
IRAC photometry
flux density [Jy]
rest frame wavelength [μm]

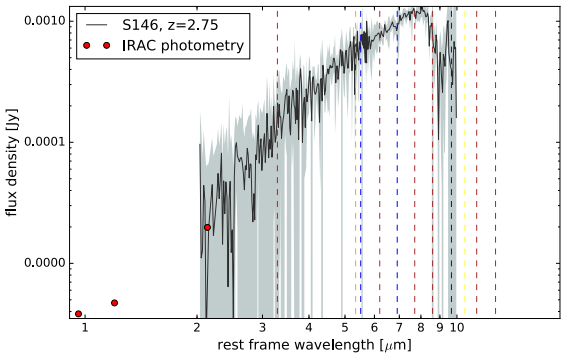
S146, z=2.75
IRAC photometry
flux density [Jy]
rest frame wavelength [μm]

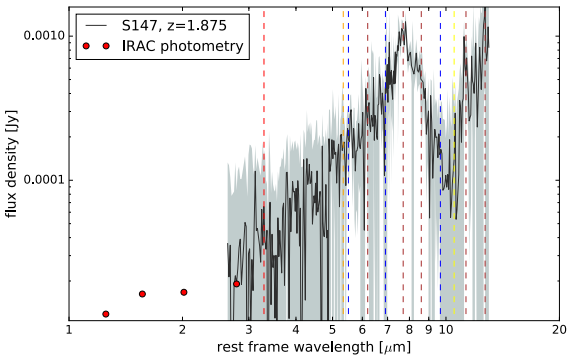
S147, z=1.875
IRAC photometry
flux density [Jy]
rest frame wavelength [μm]

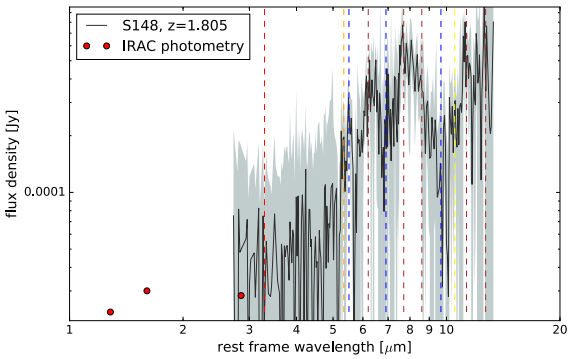
S148, z=1.805
IRAC photometry
flux density [Jy]
rest frame wavelength [μm]

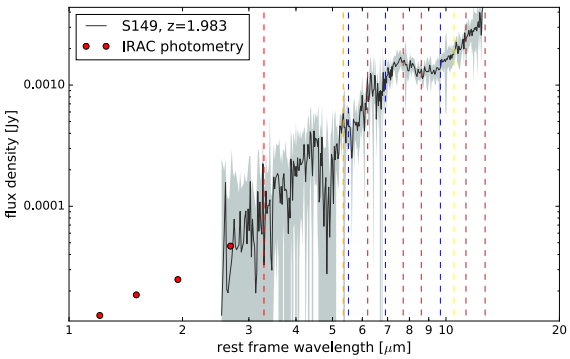
S149, z=1.983
IRAC photometry
flux density [Jy]
rest frame wavelength [μm]

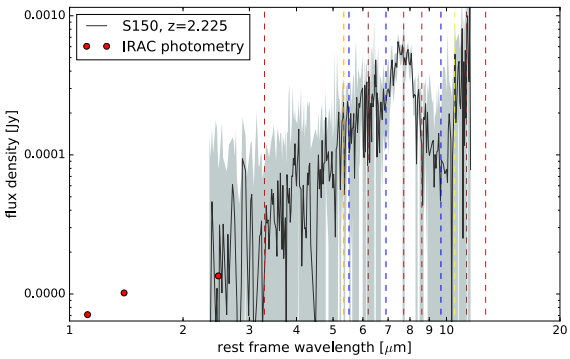
S150, z=2.225
IRAC photometry
flux density [Jy]
rest frame wavelength [μm]

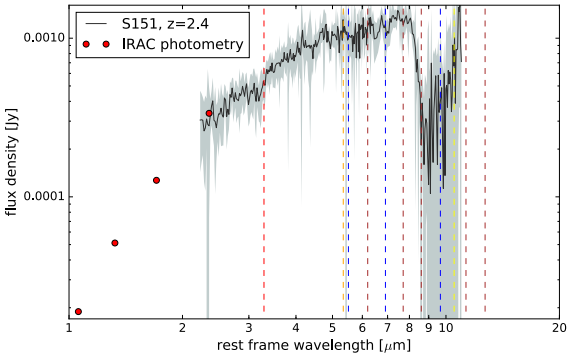
S151, z=2.4
IRAC photometry
flux density [Jy]
0.0010
0.0001
rest frame wavelength [μm]

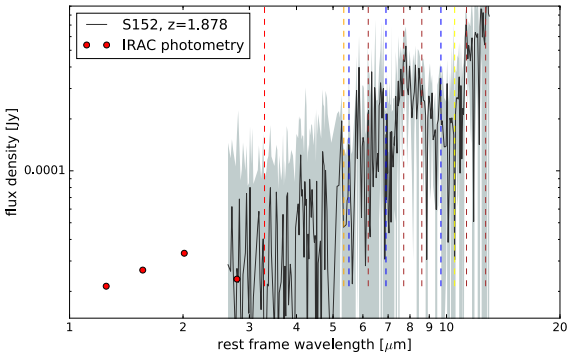
S152, z=1.878
IRAC photometry
flux density [Jy]
0.0001
rest frame wavelength [μm]

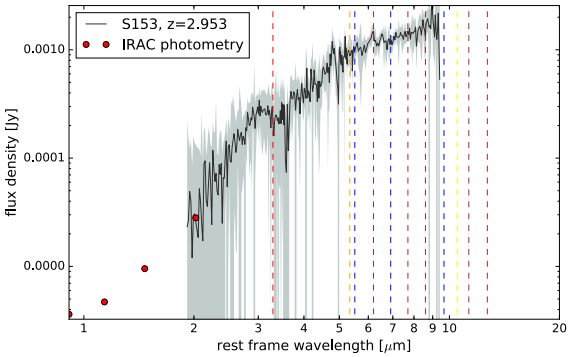
S153, z=2.953
IRAC photometry
flux density [Jy]
0.0010
0.0001
0.0000
rest frame wavelength [μm]

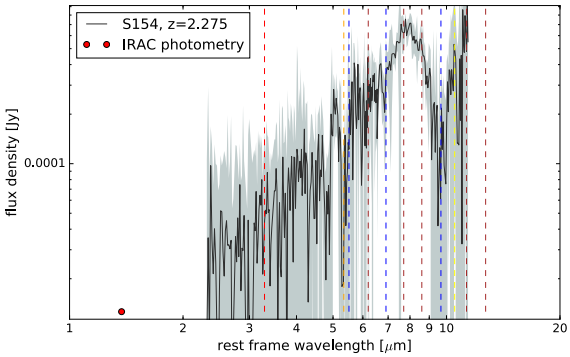
S154, z=2.275
IRAC photometry
flux density [Jy]
0.0001
rest frame wavelength [μm]

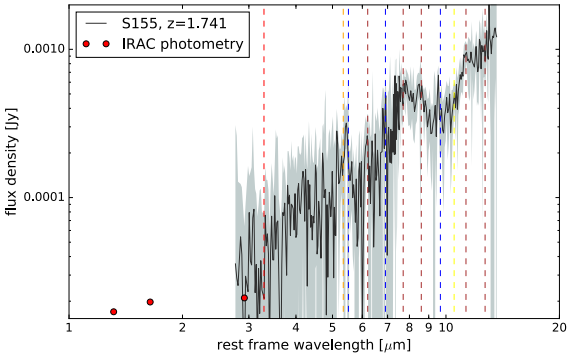
S155, z=1.741
IRAC photometry
flux density [Jy]
0.0010
0.0001
rest frame wavelength [μm]

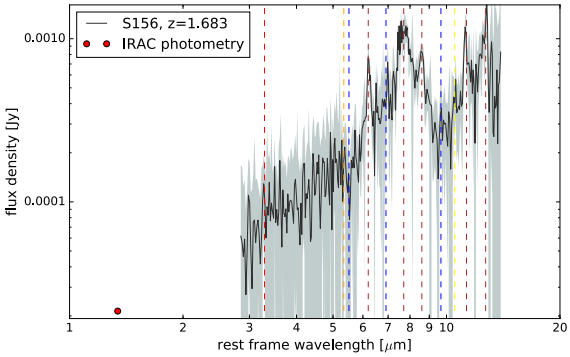
S156, z=1.683
IRAC photometry
flux density [Jy]
0.0010
0.0001
rest frame wavelength [μm]

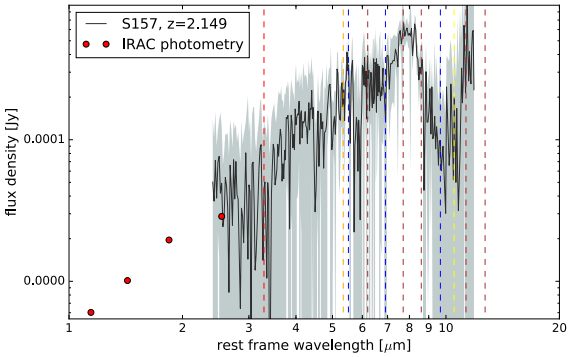
S157, z=2.149
IRAC photometry
flux density [Jy]
0.0001
0.0000
rest frame wavelength [μm]

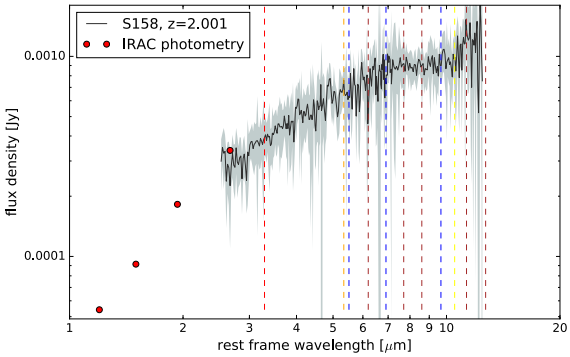
S158, z=2.001
IRAC photometry
flux density [Jy]
0.0010
0.0001
rest frame wavelength [μm]

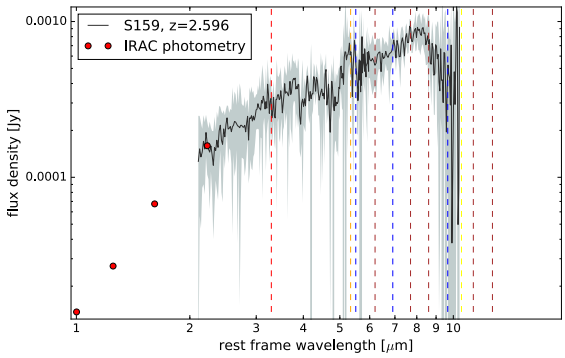
S159, z=2.596
IRAC photometry
flux density [Jy]
rest frame wavelength [μm]

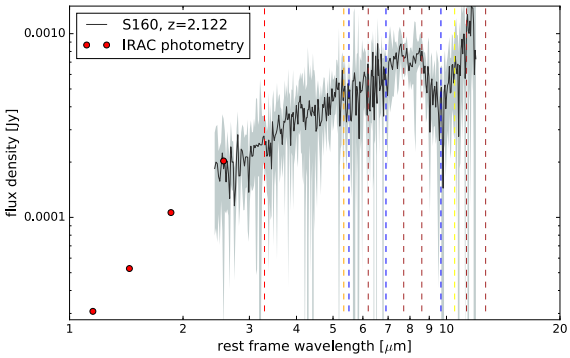
S160, z=2.122
IRAC photometry
flux density [Jy]
rest frame wavelength [μm]

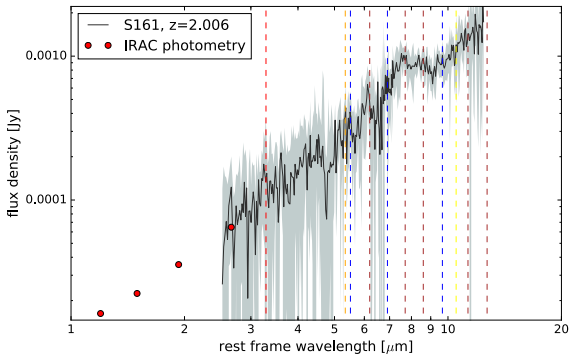
S161, z=2.006
IRAC photometry
flux density [Jy]
rest frame wavelength [μm]

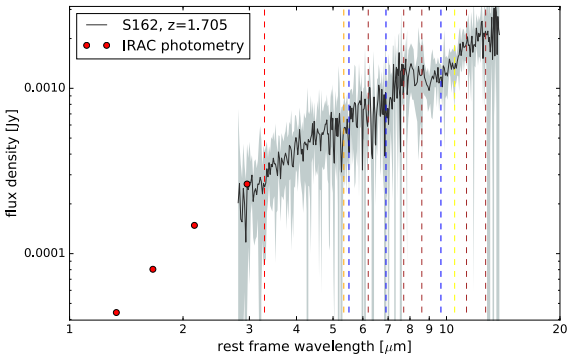
S162, z=1.705
IRAC photometry
flux density [Jy]
rest frame wavelength [μm]

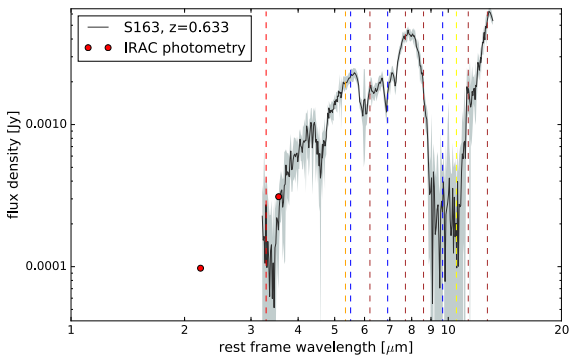
S163, z=0.633
IRAC photometry
flux density [Jy]
rest frame wavelength [μm]

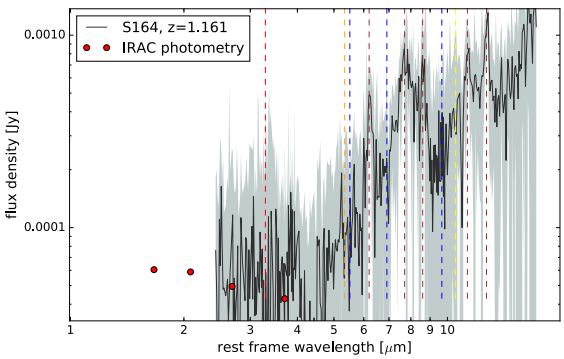
S164, z=1.161
IRAC photometry
flux density [Jy]
rest frame wavelength [μm]

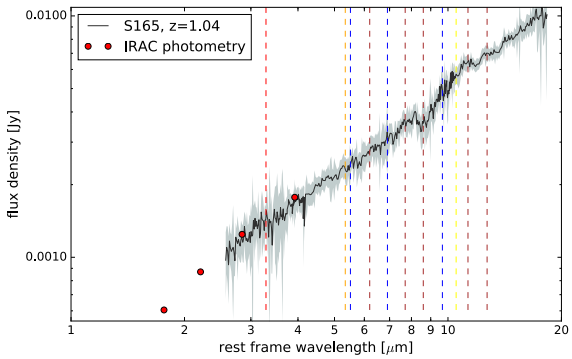
S165, z=1.04
IRAC photometry
flux density [Jy]
rest frame wavelength [μm]

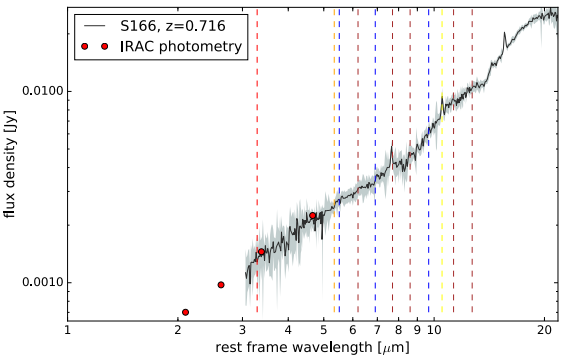
S166, z=0.716
IRAC photometry
flux density [Jy]
rest frame wavelength [μm]

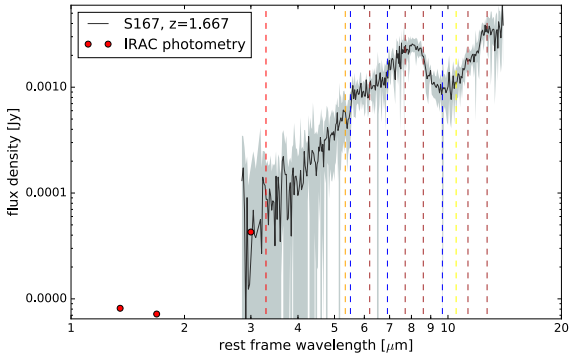
S167, z=1.667
IRAC photometry
flux density [Jy]
rest frame wavelength [μm]

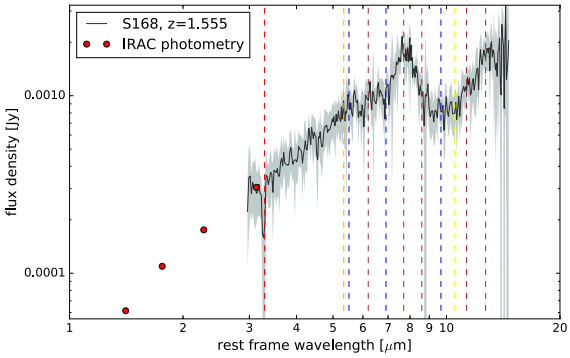
S168, z=1.555
IRAC photometry
flux density [Jy]
rest frame wavelength [μm]

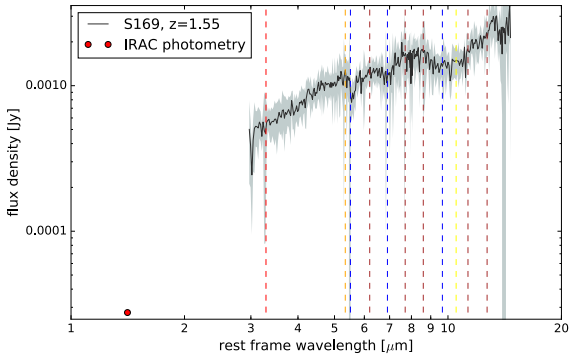
S169, z=1.55
IRAC photometry
flux density [Jy]
rest frame wavelength [μm]

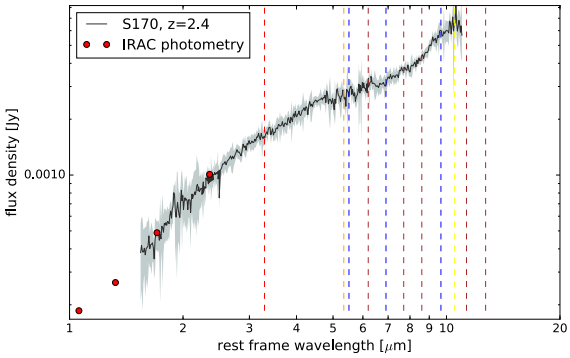
S170, z=2.4
IRAC photometry
flux density [Jy]
rest frame wavelength [μm]

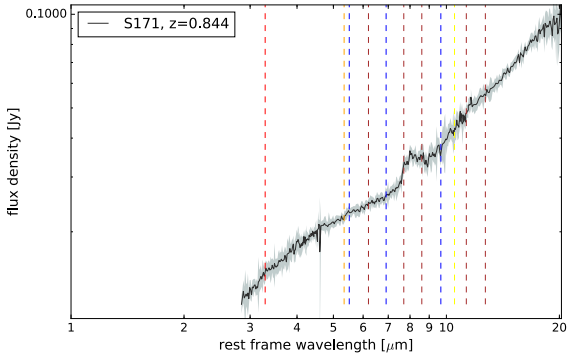
S171, z=0.844
flux density [Jy]
rest frame wavelength [μm]

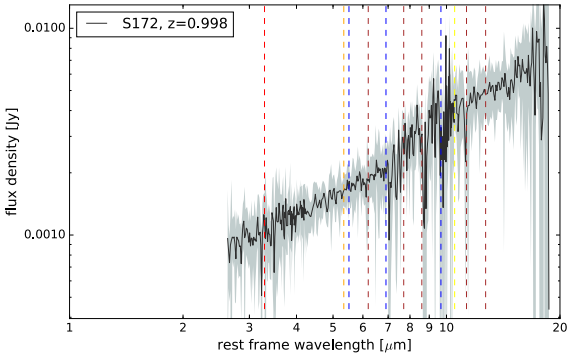
S172, z=0.998
flux density [Jy]
rest frame wavelength [μm]

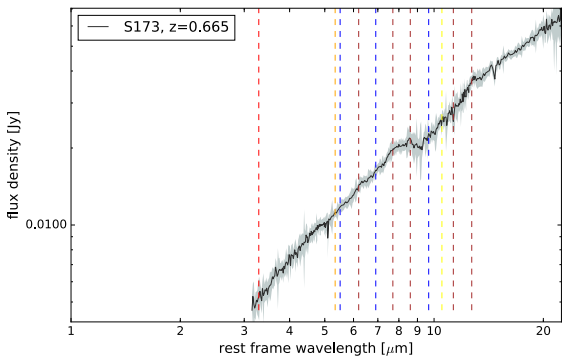
S173, z=0.665
flux density [Jy]
rest frame wavelength [μm]

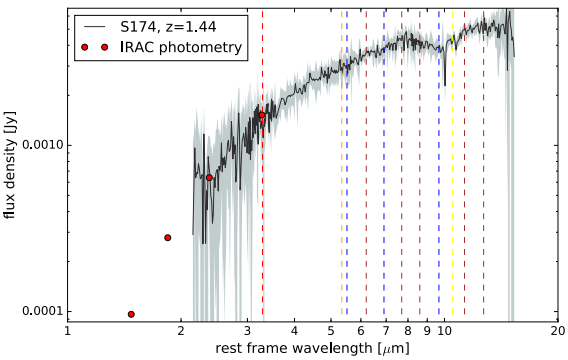
S174, z=1.44
IRAC photometry
flux density [Jy]
rest frame wavelength [μm]

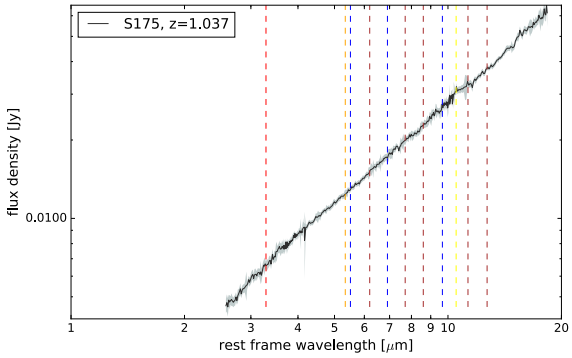
S175, z=1.037
flux density [Jy]
0.0100
rest frame wavelength [μm]

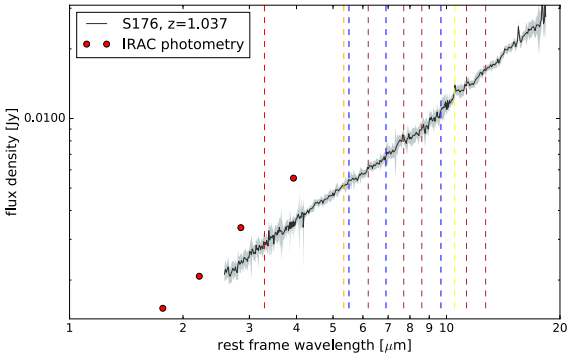
S176, z=1.037
IRAC photometry
flux density [Jy]
0.0100
rest frame wavelength [μm]

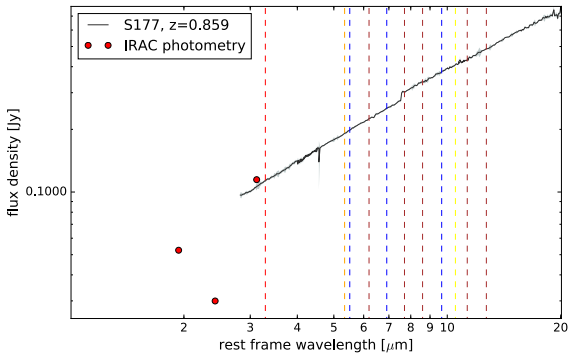
S177, z=0.859
IRAC photometry
flux density [Jy]
0.1000
rest frame wavelength [μm]

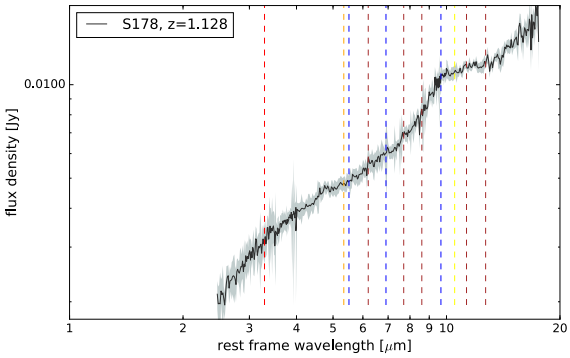
S178, z=1.128
flux density [Jy]
0.0100
rest frame wavelength [μm]

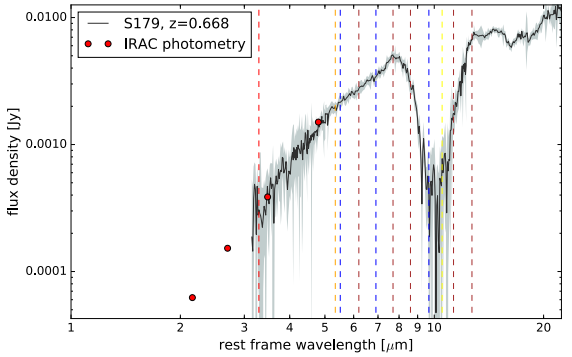
S179, z=0.668
IRAC photometry
flux density [Jy]
0.0100
0.0010
0.0001
rest frame wavelength [μm]

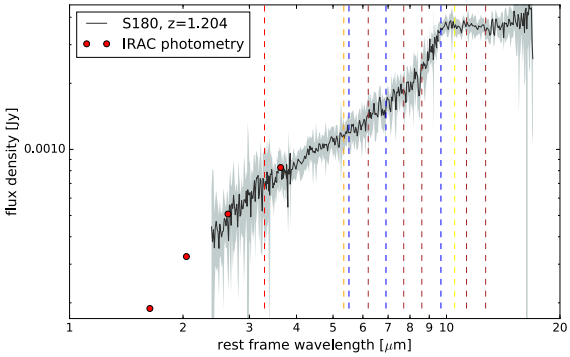
S180, z=1.204
IRAC photometry
flux density [Jy]
0.0010
rest frame wavelength [μm]

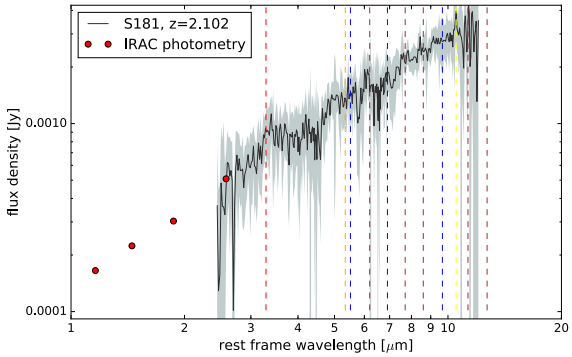
S181, z=2.102
IRAC photometry
flux density [Jy]
0.0010
0.0001
rest frame wavelength [μm]

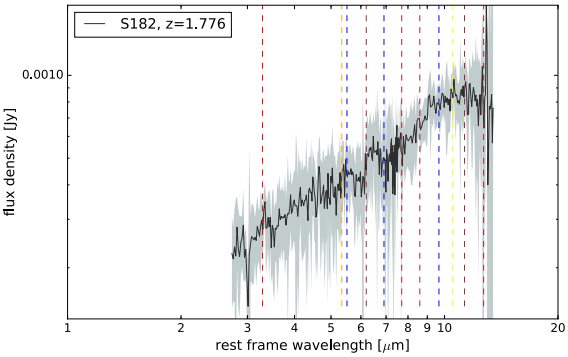
S182, z=1.776
flux density [Jy]
0.0010
rest frame wavelength [μm]

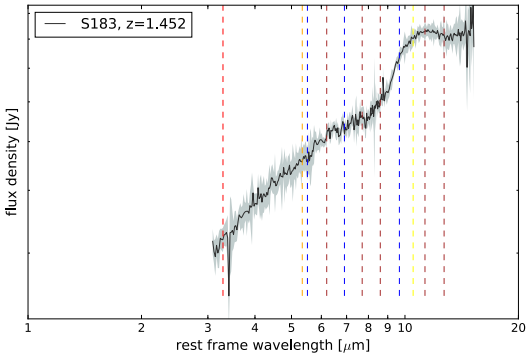
S183, z=1.452
flux density [Jy]
rest frame wavelength [μm]

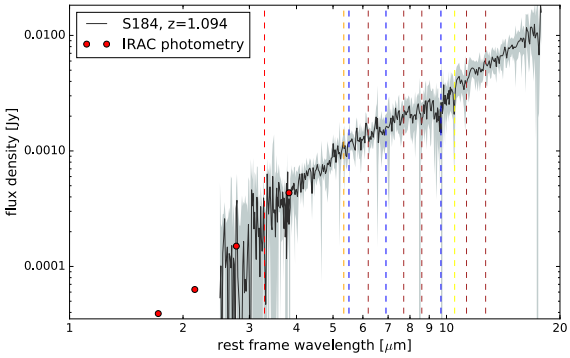
S184, z=1.094
IRAC photometry
0.0100
0.0010
0.0001
flux density [Jy]
rest frame wavelength [μm]

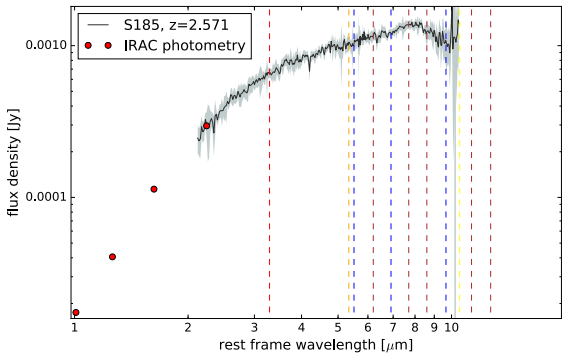
S185, z=2.571
IRAC photometry
0.0010
0.0001
flux density [Jy]
rest frame wavelength [μm]

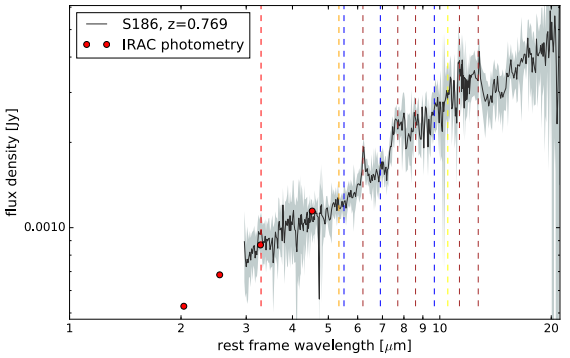
S186, z=0.769
IRAC photometry
0.0010
flux density [Jy]
rest frame wavelength [μm]

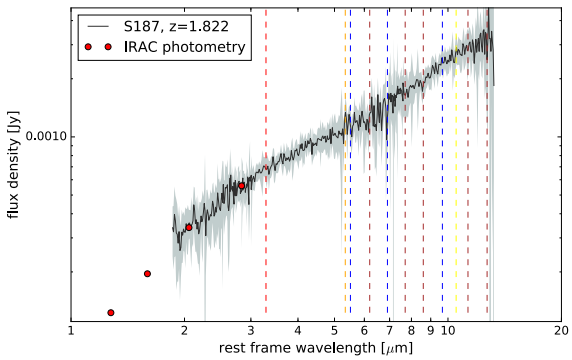
S187, z=1.822
IRAC photometry
0.0010
flux density [Jy]
rest frame wavelength [μm]

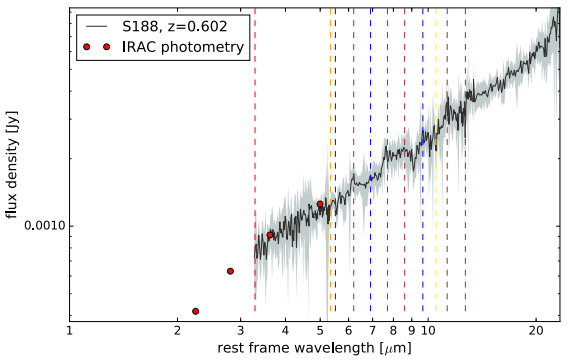
S188, z=0.602
IRAC photometry
0.0010
flux density [Jy]
rest frame wavelength [μm]

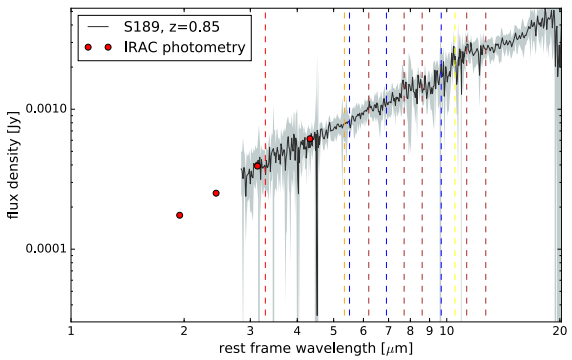
S189, z=0.85
IRAC photometry
0.0010
0.0001
flux density [Jy]
rest frame wavelength [μm]

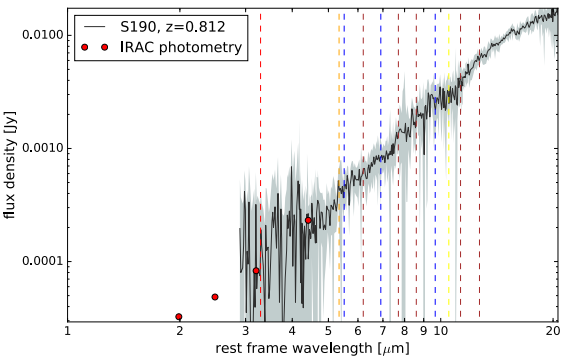
S190, z=0.812
IRAC photometry
0.0100
0.0010
0.0001
flux density [Jy]
rest frame wavelength [μm]

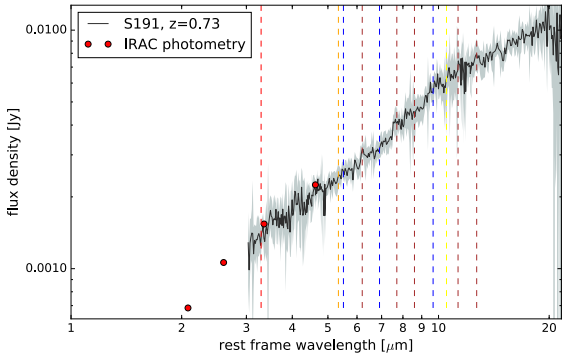
S191, z=0.73
IRAC photometry
flux density [Jy]
rest frame wavelength [μm]

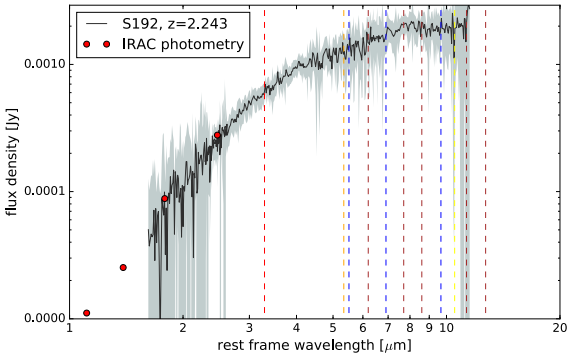
S192, z=2.243
IRAC photometry
flux density [Jy]
rest frame wavelength [μm]

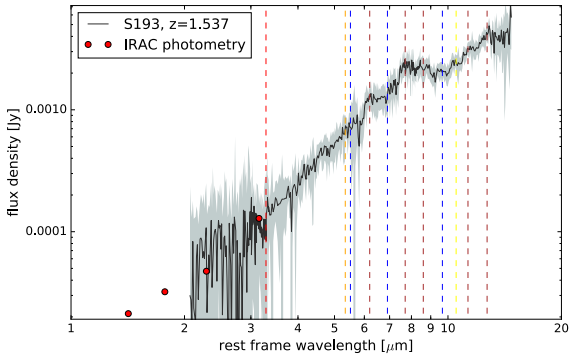
S193, z=1.537
IRAC photometry
flux density [Jy]
rest frame wavelength [μm]

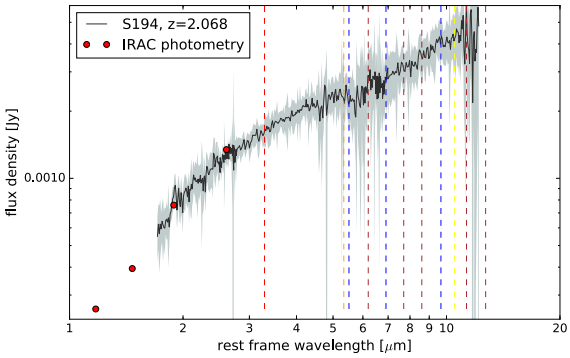
S194, z=2.068
IRAC photometry
flux density [Jy]
rest frame wavelength [μm]

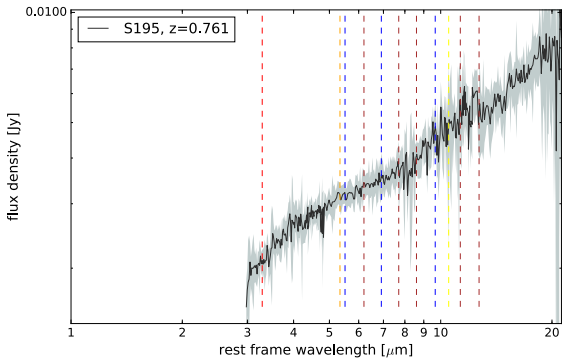
S195, z=0.761
flux density [Jy]
rest frame wavelength [μm]

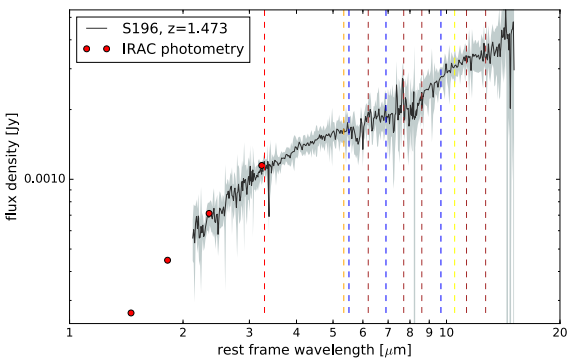
S196, z=1.473
IRAC photometry
flux density [Jy]
rest frame wavelength [μm]

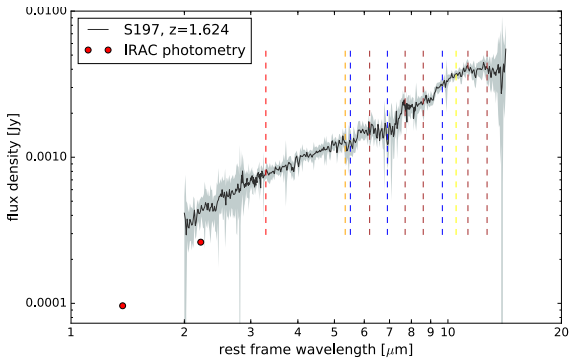
S197, z=1.624
IRAC photometry
flux density [Jy]
rest frame wavelength [μm]

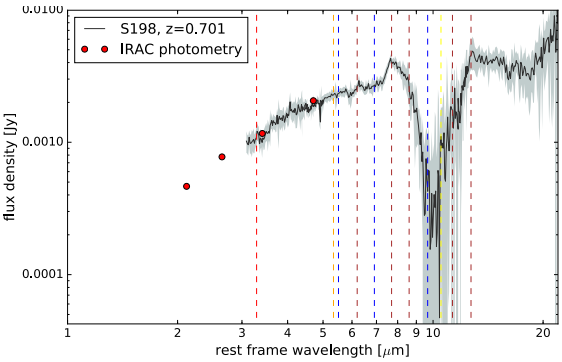
S198, z=0.701
IRAC photometry
flux density [Jy]
rest frame wavelength [μm]

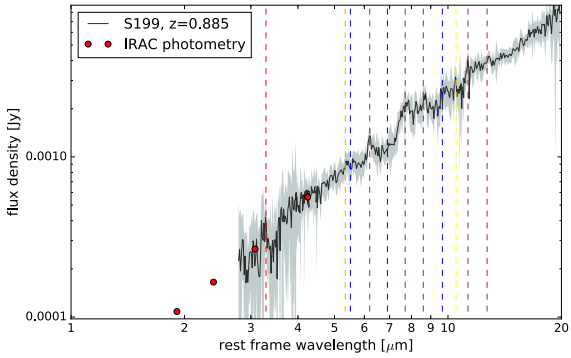
S199, z=0.885
IRAC photometry
flux density [Jy]
0.0010
0.0001
1
2
3
4
5
6
7
8
9
10
20
rest frame wavelength [μm]

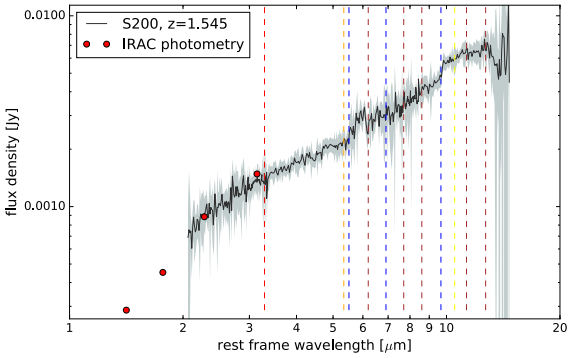
S200, z=1.545
IRAC photometry
flux density [Jy]
0.0100
0.0010
1
2
3
4
5
6
7
8
9
10
20
rest frame wavelength [μm]

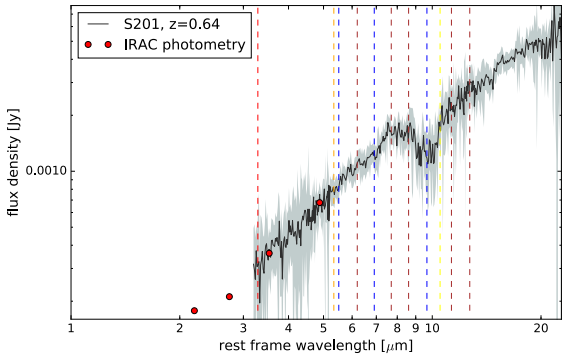
S201, z=0.64
IRAC photometry
flux density [Jy]
0.0010
1
2
3
4
5
6
7
8
9
10
20
rest frame wavelength [μm]

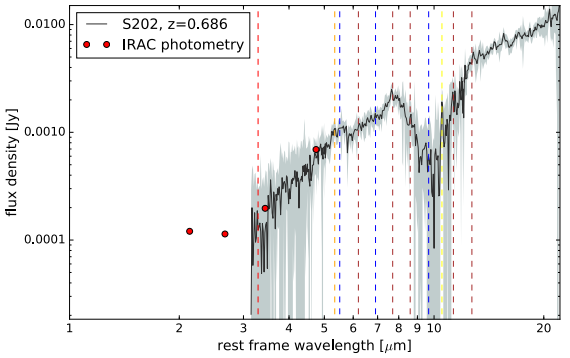
S202, z=0.686
IRAC photometry
flux density [Jy]
0.0100
0.0010
0.0001
1
2
3
4
5
6
7
8
9
10
20
rest frame wavelength [μm]

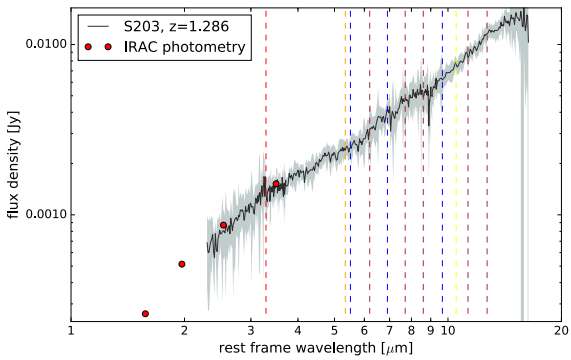
S203, z=1.286
IRAC photometry
flux density [Jy]
0.0100
0.0010
1
2
3
4
5
6
7
8
9
10
20
rest frame wavelength [μm]

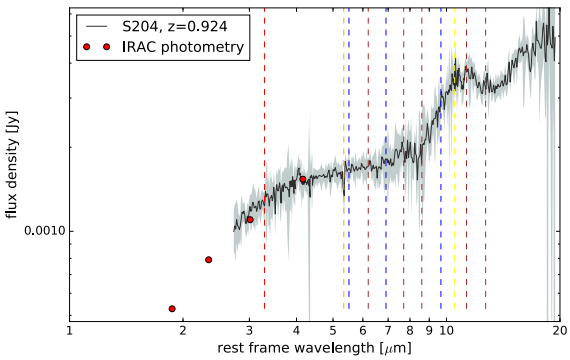
S204, z=0.924
IRAC photometry
flux density [Jy]
0.0010
1
2
3
4
5
6
7
8
9
10
20
rest frame wavelength [μm]

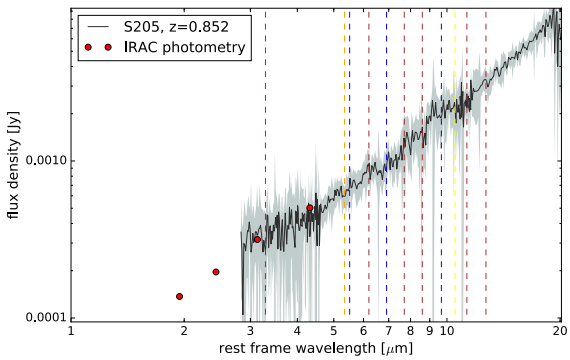
S205, z=0.852
IRAC photometry
flux density [Jy]
0.0010
0.0001
1
2
3
4
5
6
7
8
9
10
20
rest frame wavelength [μm]

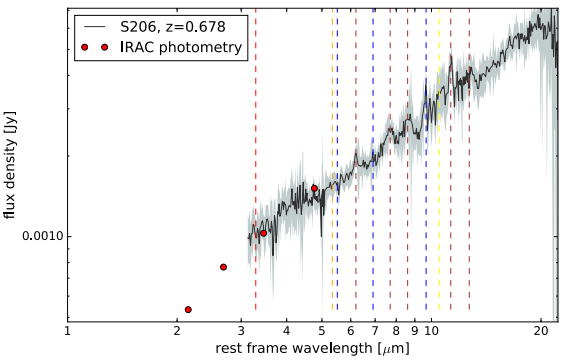
S206, z=0.678
IRAC photometry
flux density [Jy]
0.0010
1
2
3
4
5
6
7
8
9
10
20
rest frame wavelength [μm]

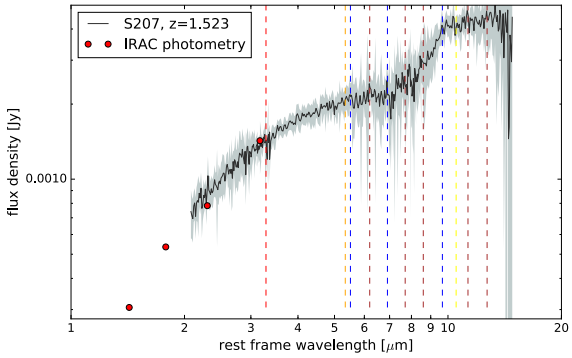
S207, z=1.523
IRAC photometry
flux density [Jy]
0.0010
rest frame wavelength [μm]

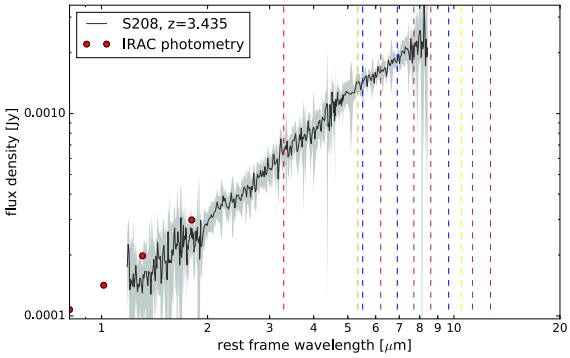
S208, z=3.435
IRAC photometry
flux density [Jy]
0.0010
0.0001
rest frame wavelength [μm]

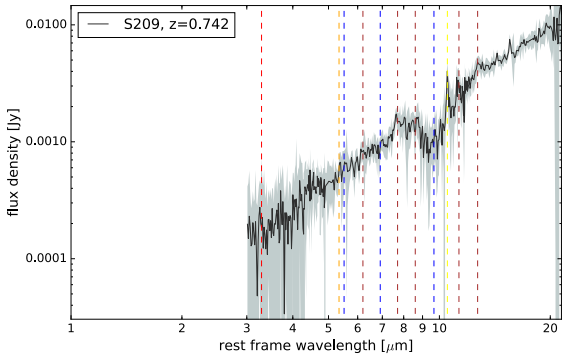
S209, z=0.742
flux density [Jy]
0.0100
0.0010
0.0001
rest frame wavelength [μm]

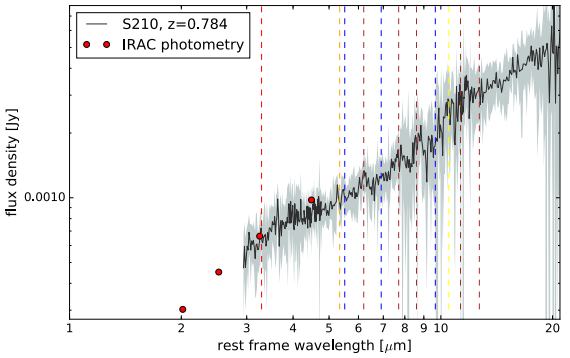
S210, z=0.784
IRAC photometry
flux density [Jy]
0.0010
rest frame wavelength [μm]

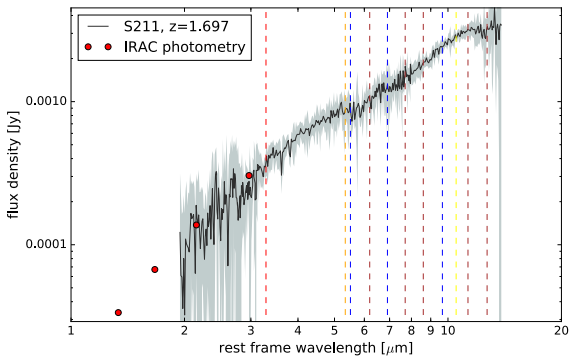
S211, z=1.697
IRAC photometry
flux density [Jy]
0.0010
0.0001
rest frame wavelength [μm]

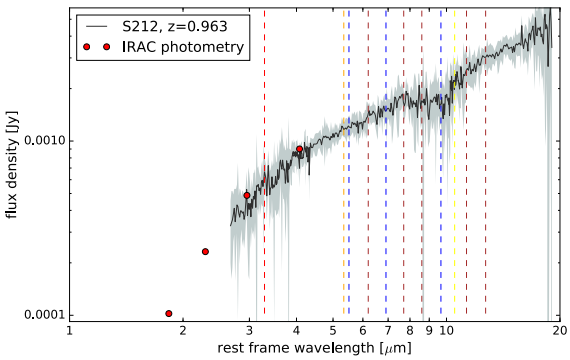
S212, z=0.963
IRAC photometry
flux density [Jy]
0.0010
0.0001
rest frame wavelength [μm]

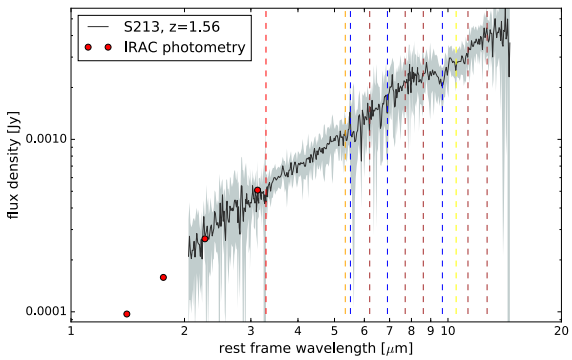
S213, z=1.56
IRAC photometry
flux density [Jy]
0.0010
0.0001
rest frame wavelength [μm]

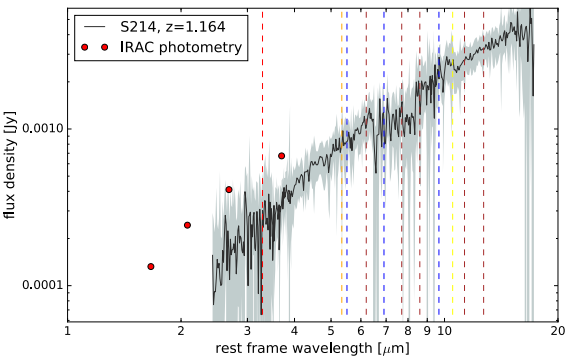
S214, z=1.164
IRAC photometry
flux density [Jy]
0.0010
0.0001
rest frame wavelength [μm]

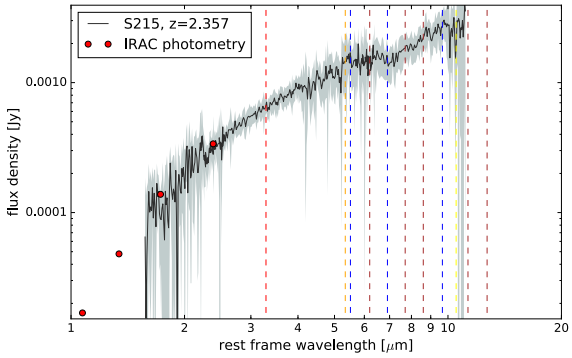
S215, z=2.357
IRAC photometry
flux density [Jy]
0.0010
0.0001
1
2
3
4
5
6
7
8
9
10
20
rest frame wavelength [μm]

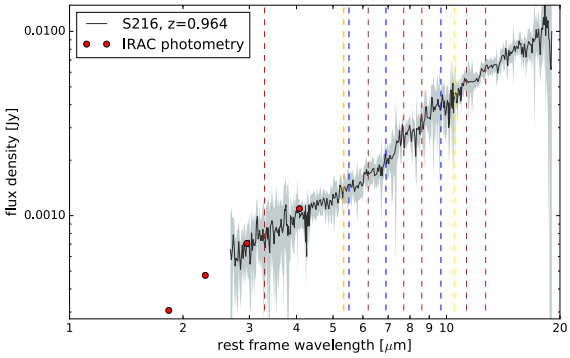
S216, z=0.964
IRAC photometry
flux density [Jy]
0.0100
0.0010
1
2
3
4
5
6
7
8
9
10
20
rest frame wavelength [μm]

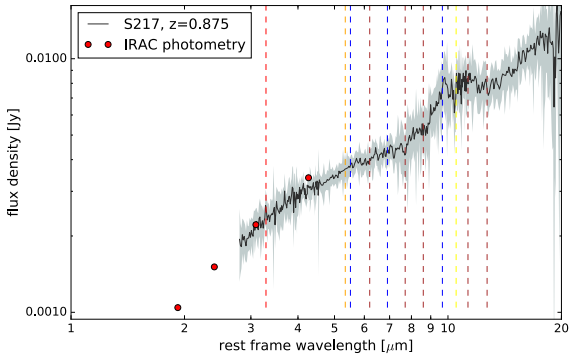
S217, z=0.875
IRAC photometry
flux density [Jy]
0.0100
0.0010
1
2
3
4
5
6
7
8
9
10
20
rest frame wavelength [μm]

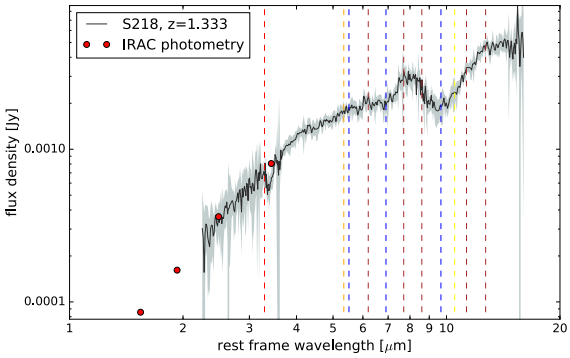
S218, z=1.333
IRAC photometry
flux density [Jy]
0.0010
0.0001
1
2
3
4
5
6
7
8
9
10
20
rest frame wavelength [μm]

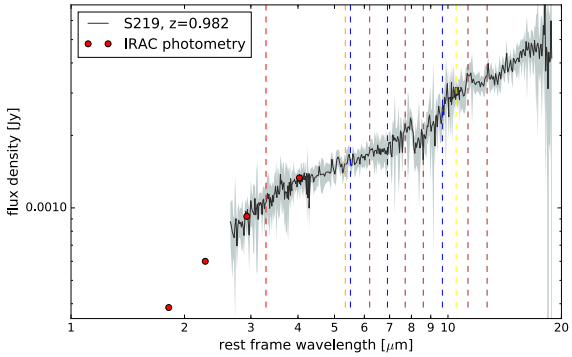
S219, z=0.982
IRAC photometry
flux density [Jy]
0.0010
1
2
3
4
5
6
7
8
9
10
20
rest frame wavelength [μm]

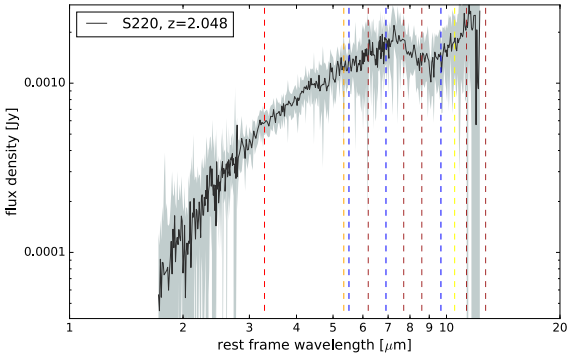
S220, z=2.048
flux density [Jy]
0.0010
0.0001
1
2
3
4
5
6
7
8
9
10
20
rest frame wavelength [μm]

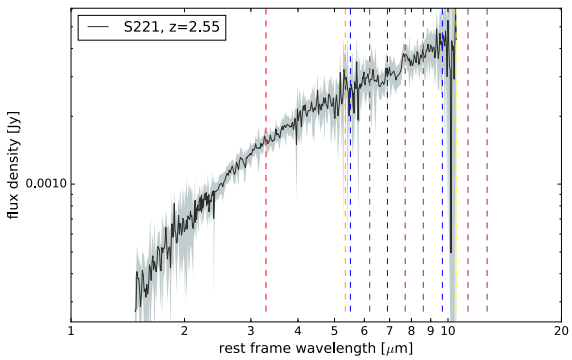
S221, z=2.55
flux density [Jy]
0.0010
1
2
3
4
5
6
7
8
9
10
20
rest frame wavelength [μm]

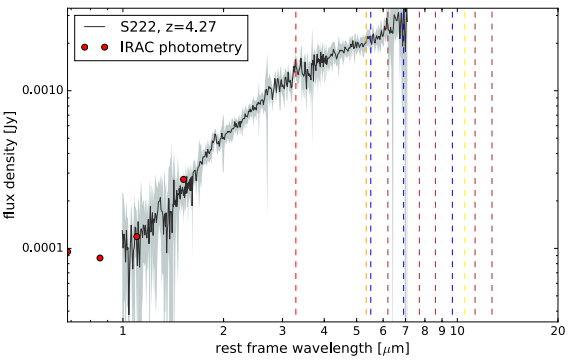
S222, z=4.27
IRAC photometry
flux density [Jy]
0.0010
0.0001
1
2
3
4
5
6
7
8
9
10
20
rest frame wavelength [μm]

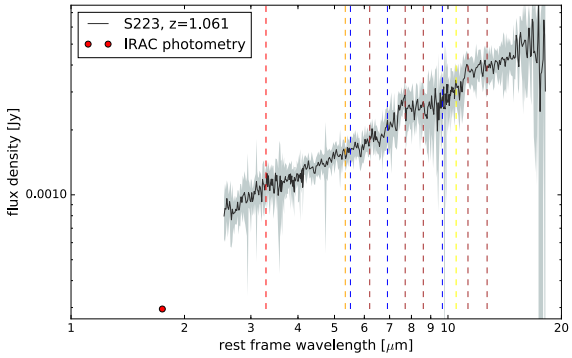
S223, z=1.061
IRAC photometry
flux density [Jy]
0.0010
rest frame wavelength [μm]

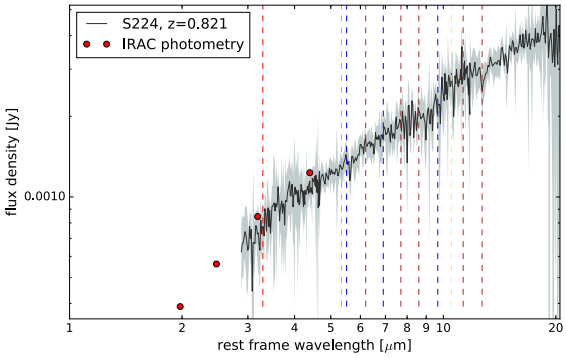
S224, z=0.821
IRAC photometry
flux density [Jy]
0.0010
rest frame wavelength [μm]

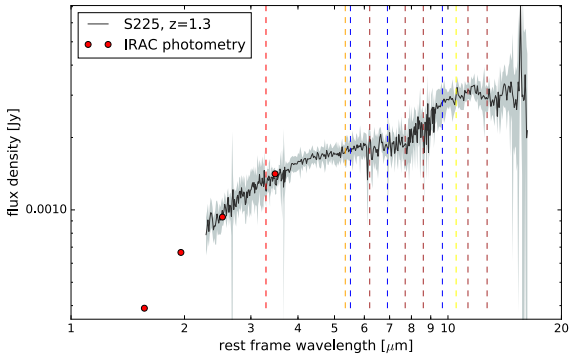
S225, z=1.3
IRAC photometry
flux density [Jy]
0.0010
rest frame wavelength [μm]

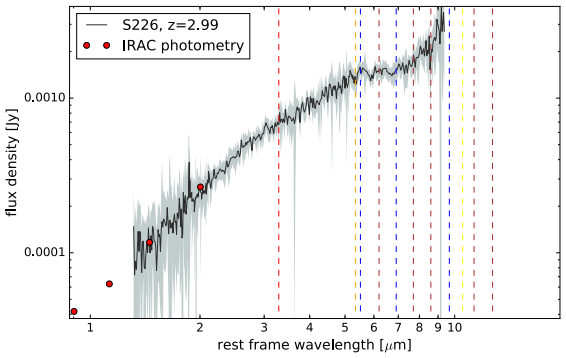
S226, z=2.99
IRAC photometry
flux density [Jy]
0.0010
0.0001
rest frame wavelength [μm]

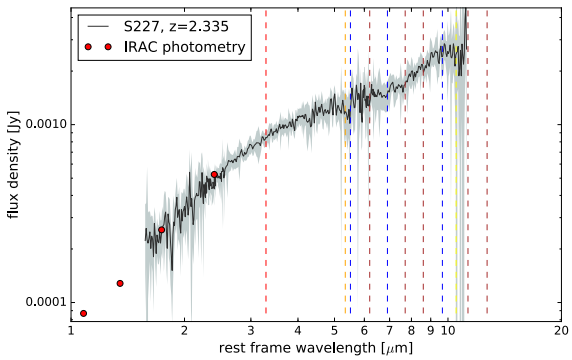
S227, z=2.335
IRAC photometry
flux density [Jy]
0.0010
0.0001
rest frame wavelength [μm]

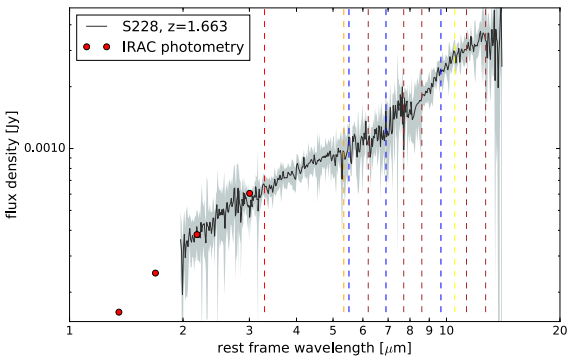
S228, z=1.663
IRAC photometry
flux density [Jy]
0.0010
rest frame wavelength [μm]

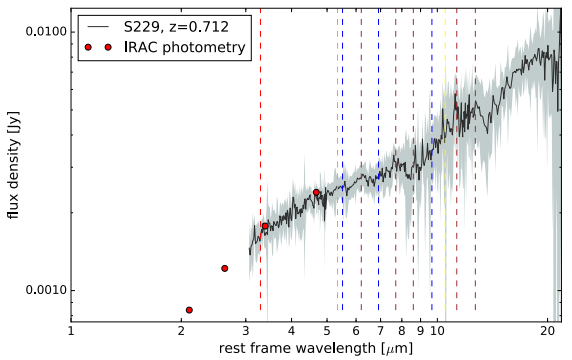
S229, z=0.712
IRAC photometry
flux density [Jy]
0.0100
0.0010
rest frame wavelength [μm]

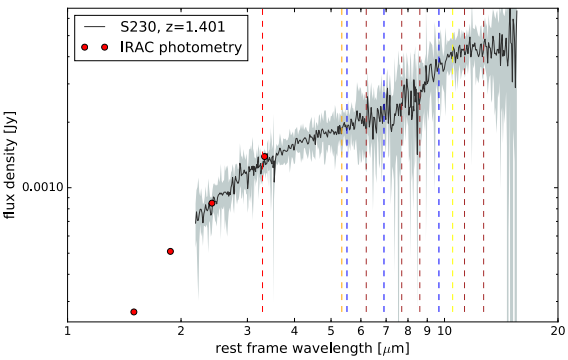
S230, z=1.401
IRAC photometry
flux density [Jy]
0.0010
rest frame wavelength [μm]

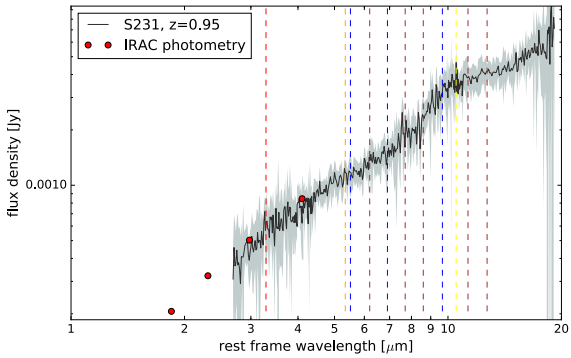
S231, z=0.95
IRAC photometry
flux density [Jy]
0.0010
rest frame wavelength [μm]

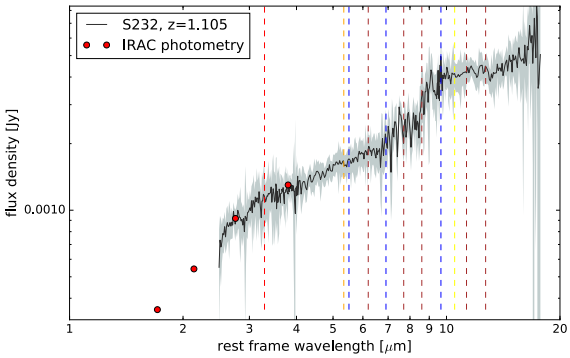
S232, z=1.105
IRAC photometry
flux density [Jy]
0.0010
rest frame wavelength [μm]

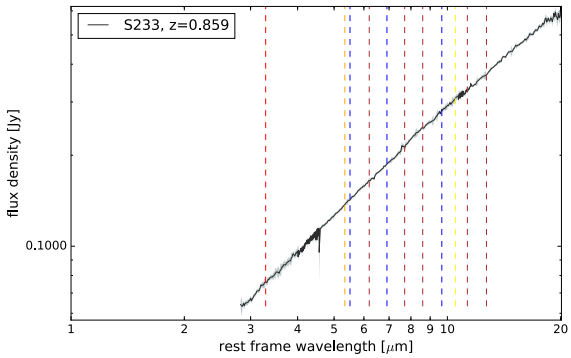
S233, z=0.859
flux density [Jy]
0.1000
rest frame wavelength [μm]

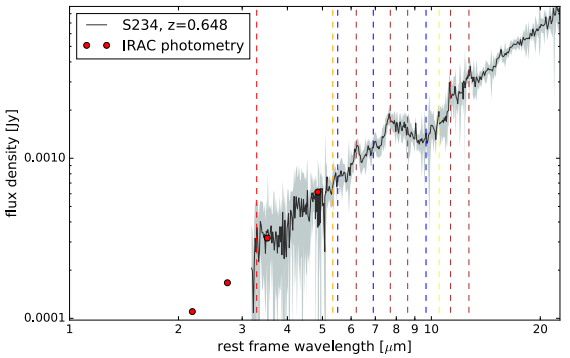
S234, z=0.648
IRAC photometry
flux density [Jy]
0.0010
0.0001
rest frame wavelength [μm]

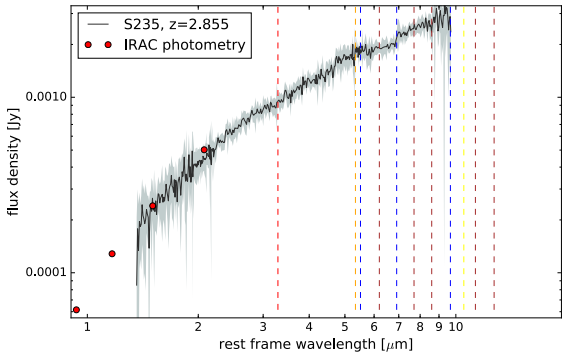
S235, z=2.855
IRAC photometry
flux density [Jy]
0.0010
0.0001
rest frame wavelength [μm]

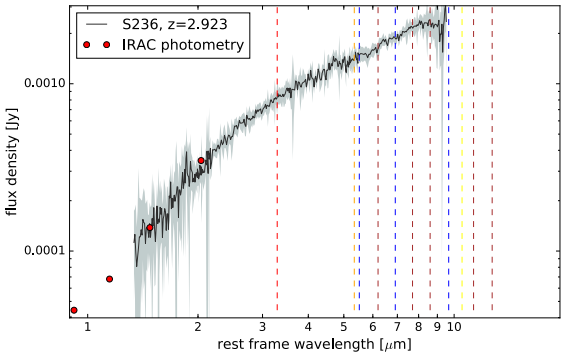
S236, z=2.923
IRAC photometry
flux density [Jy]
0.0010
0.0001
rest frame wavelength [μm]

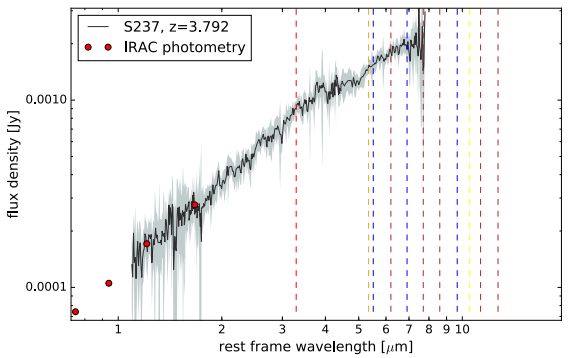
S237, z=3.792
IRAC photometry
flux density [Jy]
0.0010
0.0001
rest frame wavelength [μm]

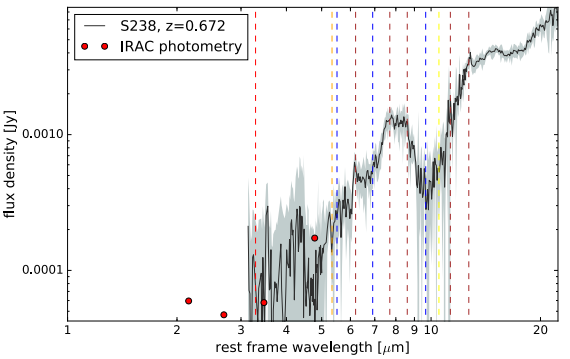
S238, z=0.672
IRAC photometry
flux density [Jy]
0.0010
0.0001
rest frame wavelength [μm]

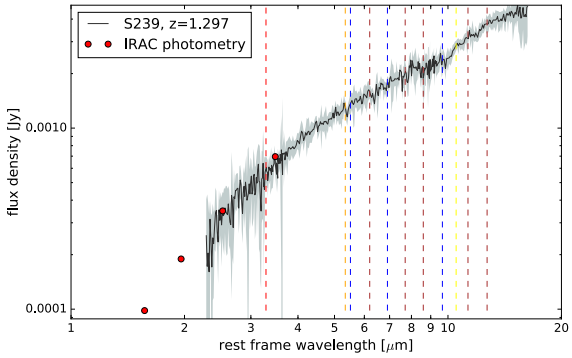
S239, z=1.297
IRAC photometry
flux density [Jy]
0.0010
0.0001
1
2
3
4
5
6
7
8
9
10
20
rest frame wavelength [μm]

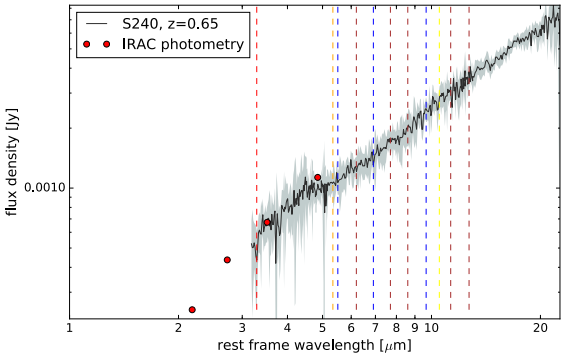
S240, z=0.65
IRAC photometry
flux density [Jy]
0.0010
1
2
3
4
5
6
7
8
9
10
20
rest frame wavelength [μm]

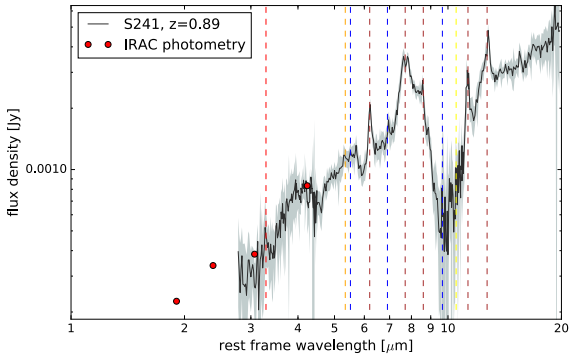
S241, z=0.89
IRAC photometry
flux density [Jy]
0.0010
1
2
3
4
5
6
7
8
9
10
20
rest frame wavelength [μm]

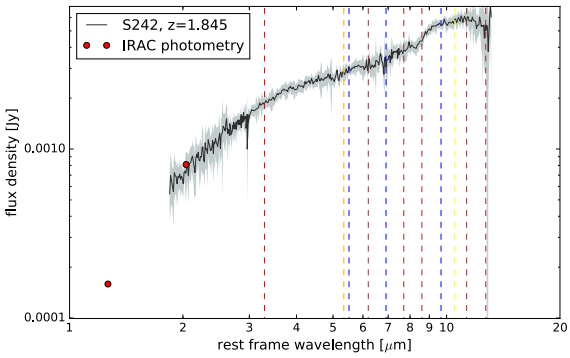
S242, z=1.845
IRAC photometry
flux density [Jy]
0.0010
0.0001
1
2
3
4
5
6
7
8
9
10
20
rest frame wavelength [μm]

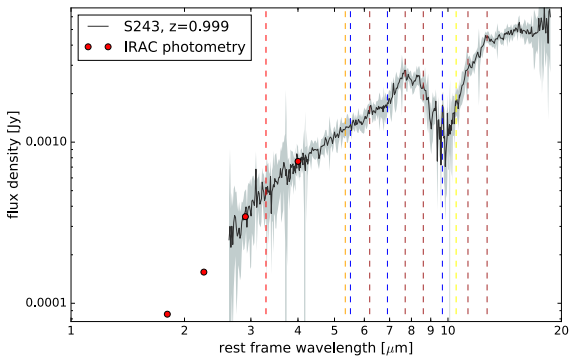
S243, z=0.999
IRAC photometry
flux density [Jy]
0.0010
0.0001
1
2
3
4
5
6
7
8
9
10
20
rest frame wavelength [μm]

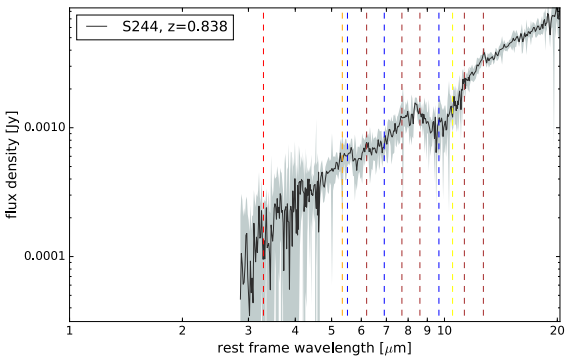
S244, z=0.838
flux density [Jy]
0.0010
0.0001
1
2
3
4
5
6
7
8
9
10
20
rest frame wavelength [μm]

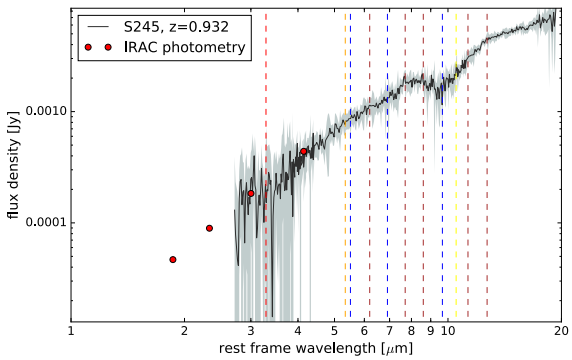
S245, z=0.932
IRAC photometry
flux density [Jy]
0.0010
0.0001
1
2
3
4
5
6
7
8
9
10
20
rest frame wavelength [μm]

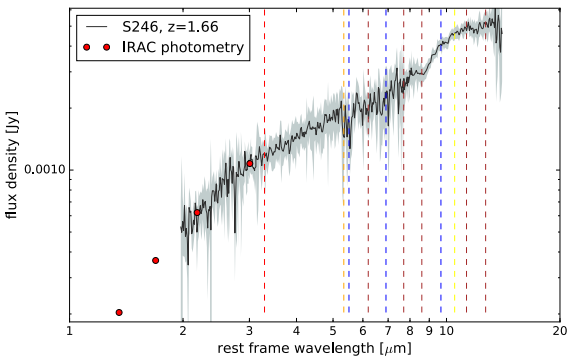
S246, z=1.66
IRAC photometry
flux density [Jy]
0.0010
1
2
3
4
5
6
7
8
9
10
20
rest frame wavelength [μm]

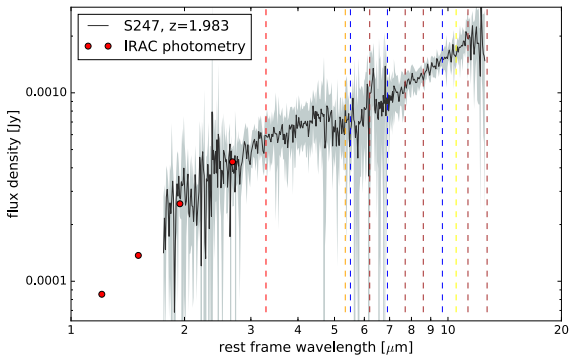
S247, z=1.983
IRAC photometry
flux density [Jy]
0.0010
0.0001
1 2 3 4 5 6 7 8 9 10 20
rest frame wavelength [μm]

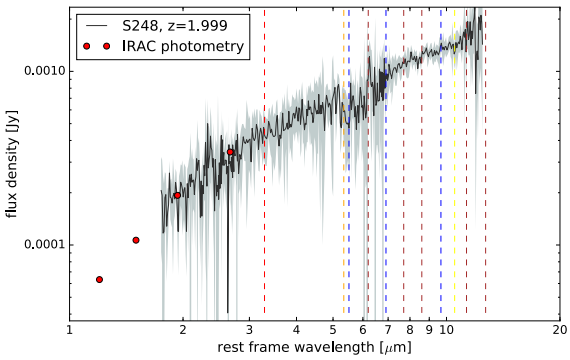
S248, z=1.999
IRAC photometry
flux density [Jy]
0.0010
0.0001
1 2 3 4 5 6 7 8 9 10 20
rest frame wavelength [μm]

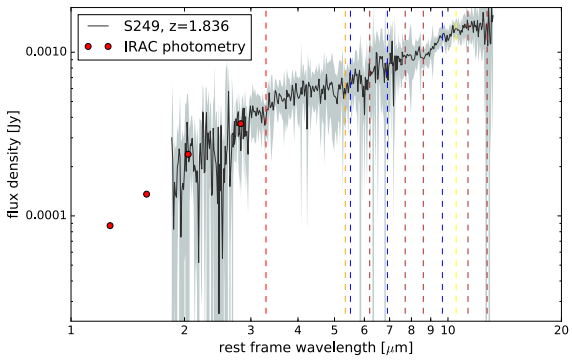
S249, z=1.836
IRAC photometry
flux density [Jy]
0.0010
0.0001
1 2 3 4 5 6 7 8 9 10 20
rest frame wavelength [μm]

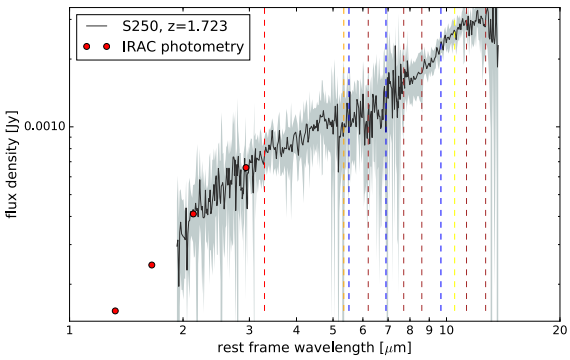
S250, z=1.723
IRAC photometry
flux density [Jy]
0.0010
1 2 3 4 5 6 7 8 9 10 20
rest frame wavelength [μm]

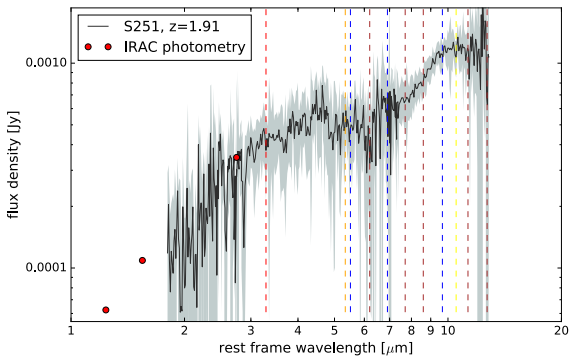
S251, z=1.91
IRAC photometry
flux density [Jy]
0.0010
0.0001
1 2 3 4 5 6 7 8 9 10 20
rest frame wavelength [μm]

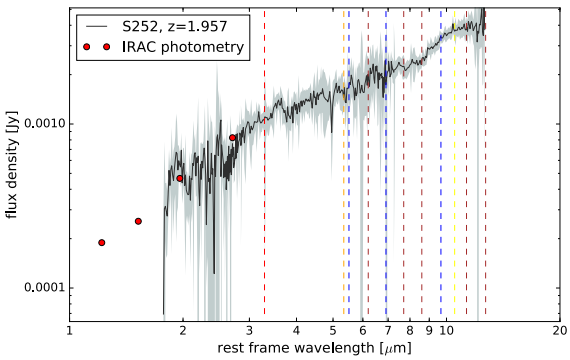
S252, z=1.957
IRAC photometry
flux density [Jy]
0.0010
0.0001
1 2 3 4 5 6 7 8 9 10 20
rest frame wavelength [μm]

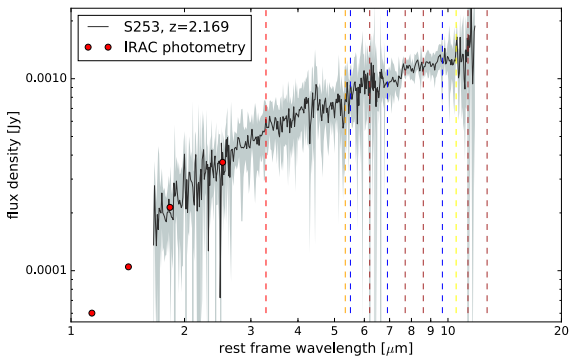
S253, z=2.169
IRAC photometry
flux density [Jy]
0.0010
0.0001
1 2 3 4 5 6 7 8 9 10 20
rest frame wavelength [μm]

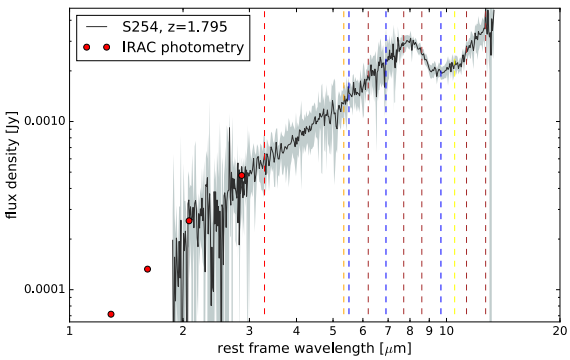
S254, z=1.795
IRAC photometry
flux density [Jy]
0.0010
0.0001
1 2 3 4 5 6 7 8 9 10 20
rest frame wavelength [μm]

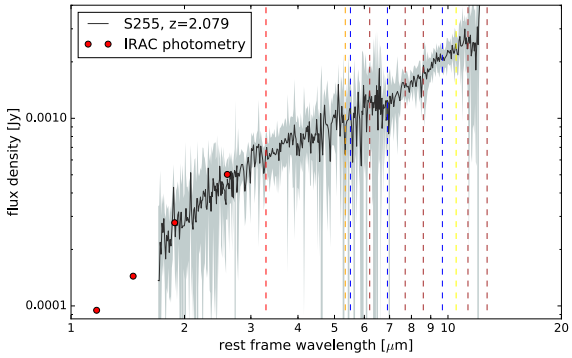
S255, z=2.079
IRAC photometry
flux density [Jy]
0.0010
0.0001
1 2 3 4 5 6 7 8 9 10 20
rest frame wavelength [μm]

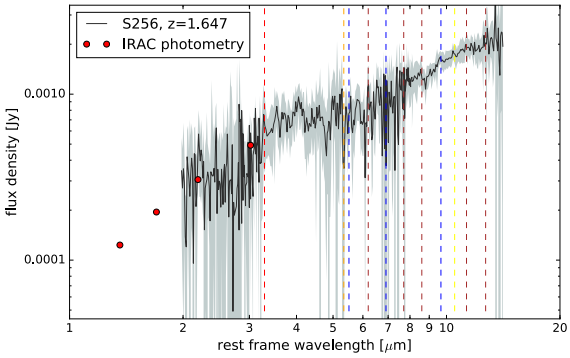
S256, z=1.647
IRAC photometry
flux density [Jy]
0.0010
0.0001
1 2 3 4 5 6 7 8 9 10 20
rest frame wavelength [μm]

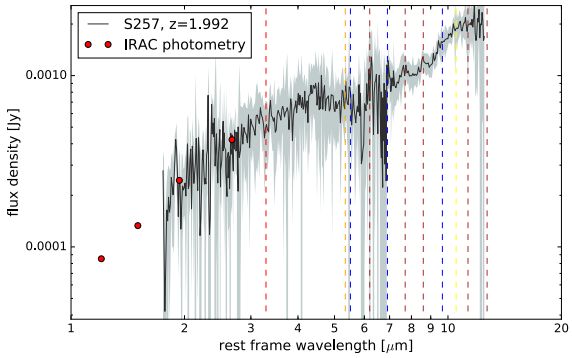
S257, z=1.992
IRAC photometry
flux density [Jy]
0.0010
0.0001
1 2 3 4 5 6 7 8 9 10 20
rest frame wavelength [μm]

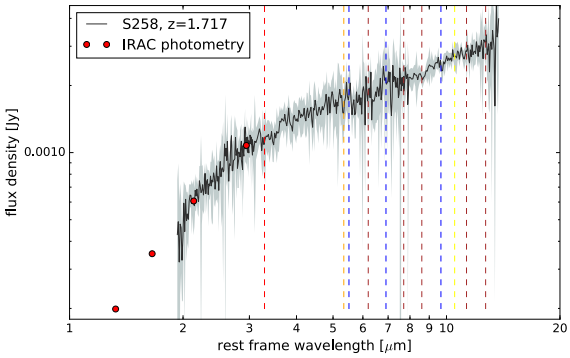
S258, z=1.717
IRAC photometry
flux density [Jy]
0.0010
1 2 3 4 5 6 7 8 9 10 20
rest frame wavelength [μm]

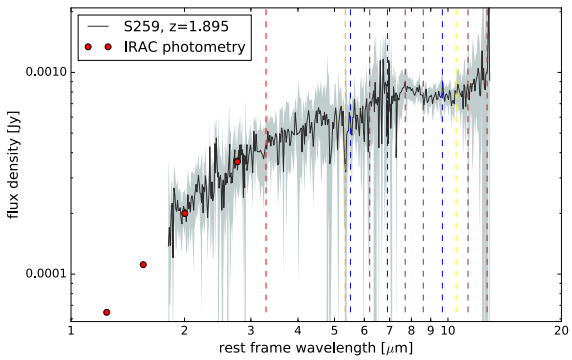
S259, z=1.895
IRAC photometry
flux density [Jy]
0.0010
0.0001
1 2 3 4 5 6 7 8 9 10 20
rest frame wavelength [μm]

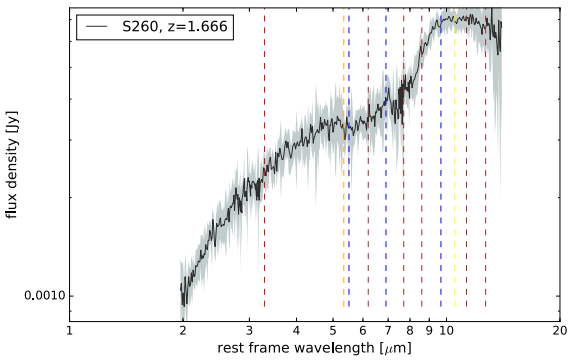
S260, z=1.666
flux density [Jy]
0.0010
1 2 3 4 5 6 7 8 9 10 20
rest frame wavelength [μm]

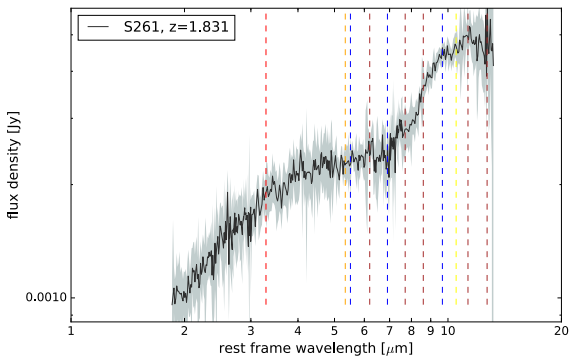
S261, z=1.831
flux density [Jy]
0.0010
1 2 3 4 5 6 7 8 9 10 20
rest frame wavelength [μm]

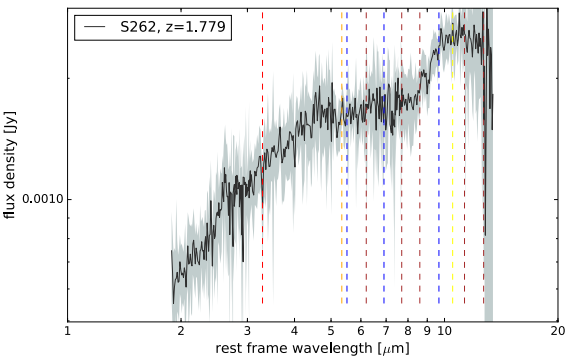
S262, z=1.779
flux density [Jy]
0.0010
1 2 3 4 5 6 7 8 9 10 20
rest frame wavelength [μm]

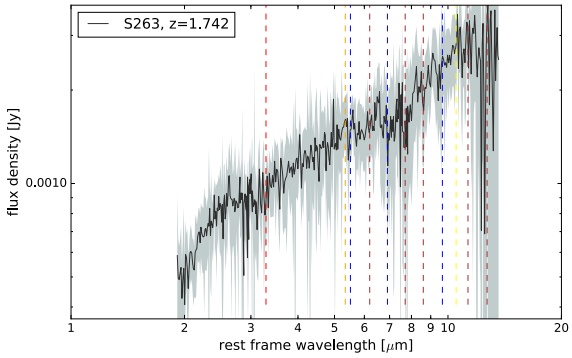
S263, z=1.742
flux density [Jy]
0.0010
rest frame wavelength [μm]

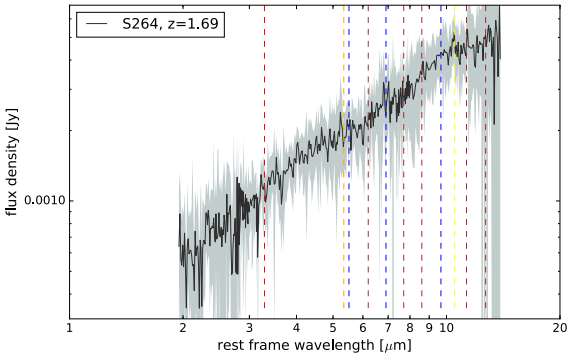
S264, z=1.69
flux density [Jy]
0.0010
rest frame wavelength [μm]

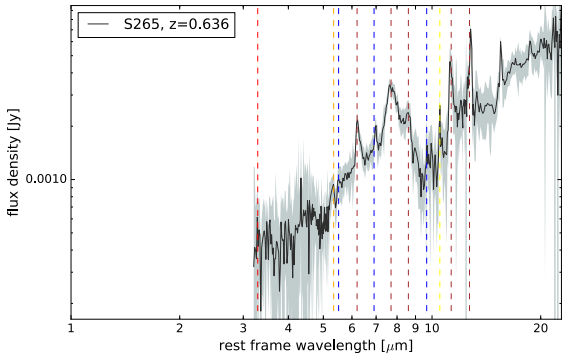
S265, z=0.636
flux density [Jy]
0.0010
rest frame wavelength [μm]

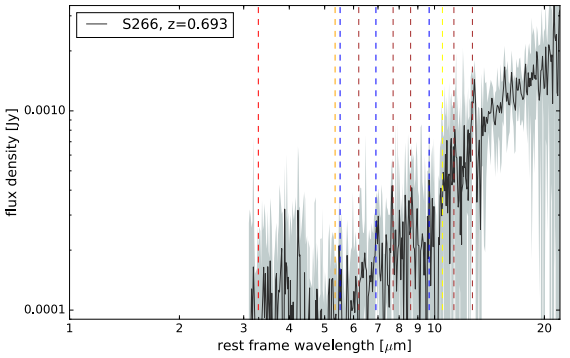
S266, z=0.693
flux density [Jy]
0.0010
0.0001
rest frame wavelength [μm]

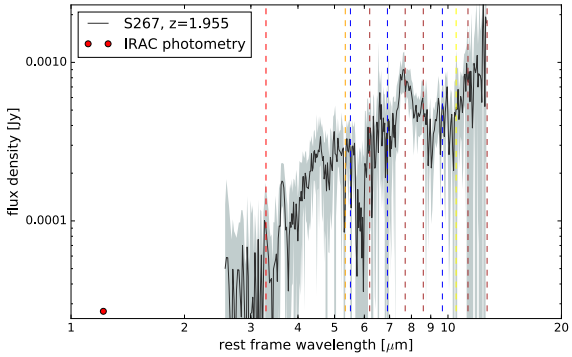
S267, z=1.955
IRAC photometry
flux density [Jy]
0.0010
0.0001
rest frame wavelength [μm]

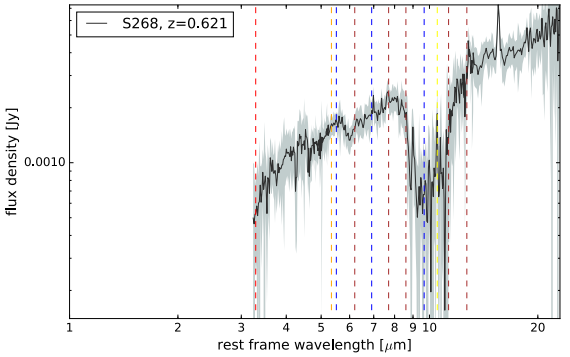
S268, z=0.621
flux density [Jy]
0.0010
rest frame wavelength [μm]

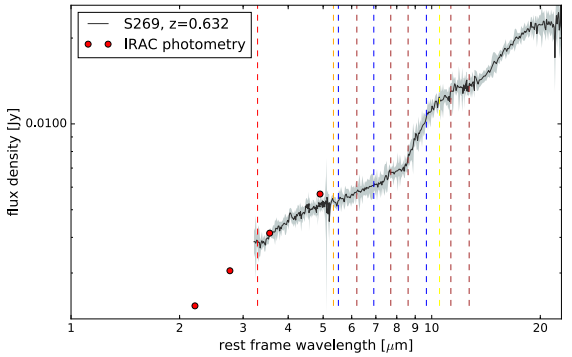
S269, z=0.632
IRAC photometry
flux density [Jy]
0.0100
rest frame wavelength [μm]

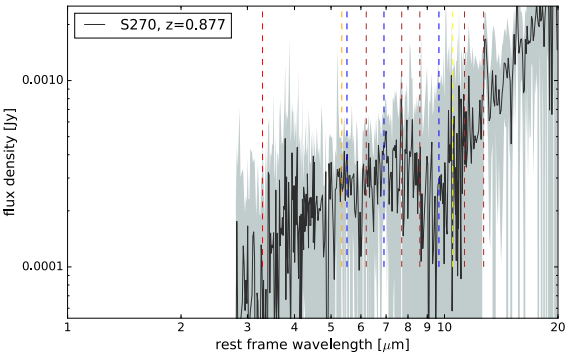
S270, z=0.877
flux density [Jy]
0.0010
0.0001
rest frame wavelength [μm]

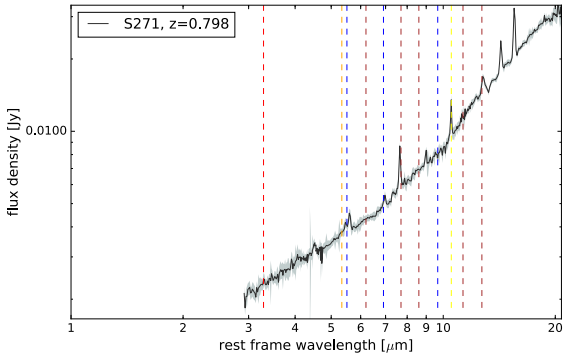
S271, z=0.798
flux density [Jy]
0.0100
rest frame wavelength [μm]

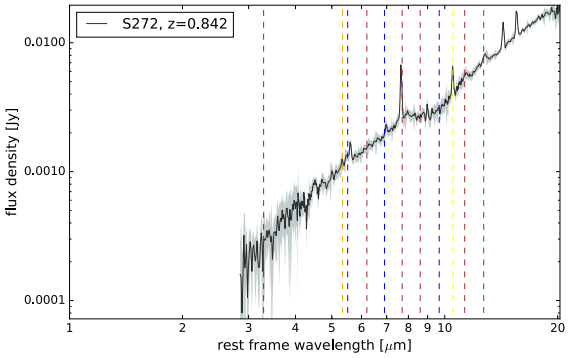
S272, z=0.842
flux density [Jy]
0.0100
0.0010
0.0001
rest frame wavelength [μm]

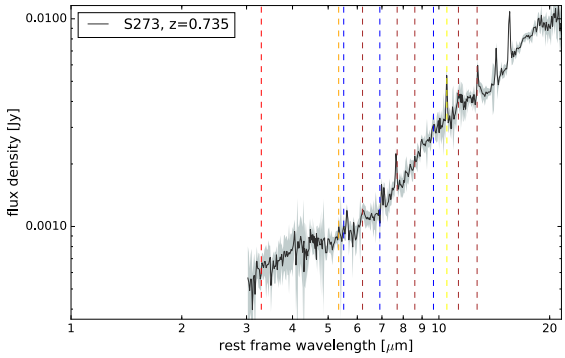
S273, z=0.735
flux density [Jy]
0.0100
0.0010
rest frame wavelength [μm]

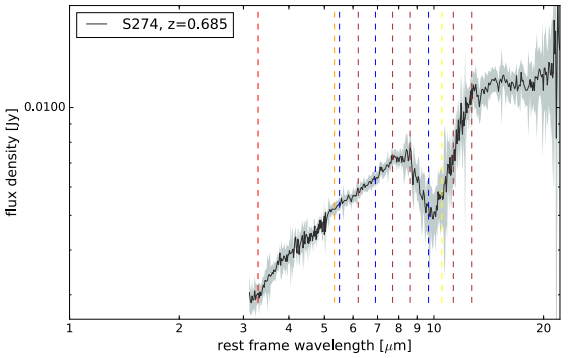
S274, z=0.685
flux density [Jy]
0.0100
rest frame wavelength [μm]

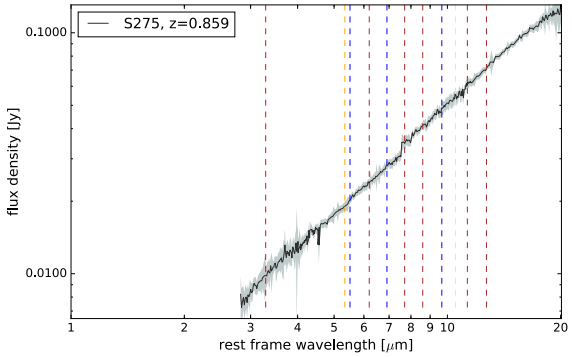
S275, z=0.859
flux density [Jy]
0.1000
0.0100
rest frame wavelength [μm]

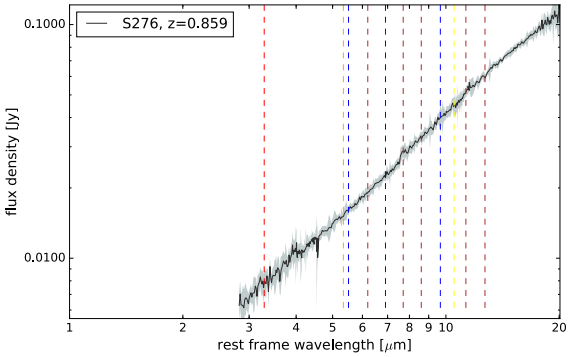
S276, z=0.859
flux density [Jy]
0.1000
0.0100
rest frame wavelength [μm]

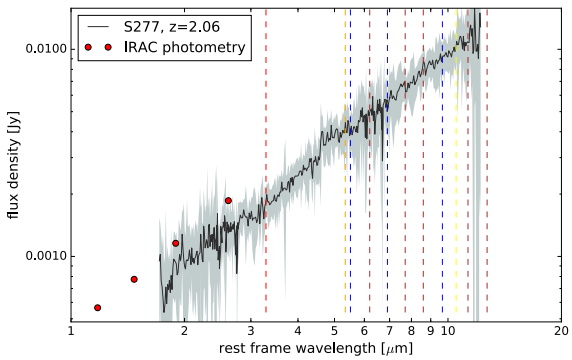
S277, z=2.06
IRAC photometry
flux density [Jy]
0.0100
0.0010
rest frame wavelength [μm]

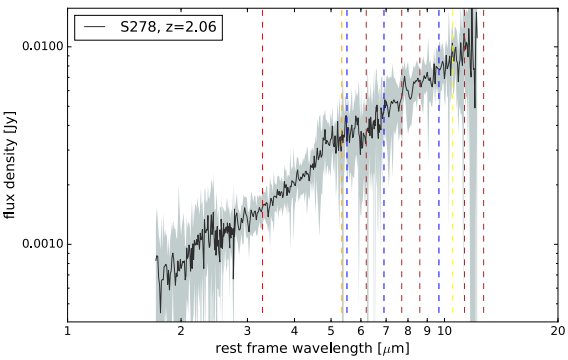
S278, z=2.06
flux density [Jy]
0.0100
0.0010
rest frame wavelength [μm]

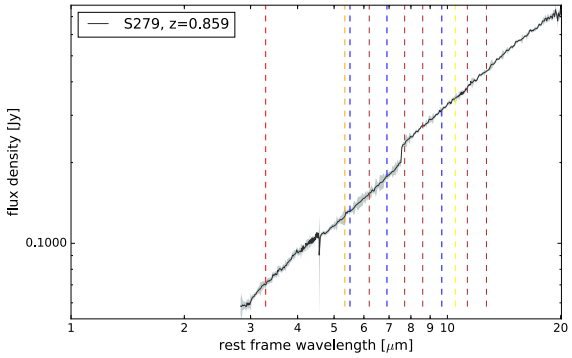
S279, z=0.859
flux density [Jy]
0.1000
1 2 3 4 5 6 7 8 9 10 20
rest frame wavelength [μm]

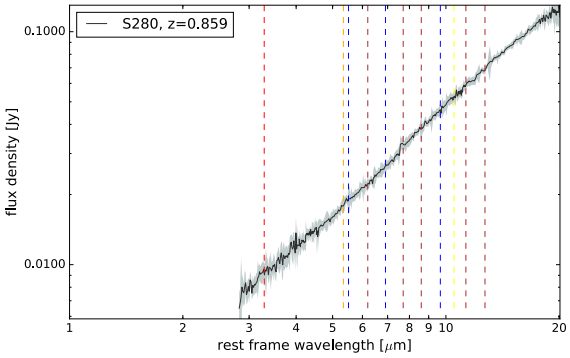
S280, z=0.859
flux density [Jy]
0.1000
0.0100
1 2 3 4 5 6 7 8 9 10 20
rest frame wavelength [μm]

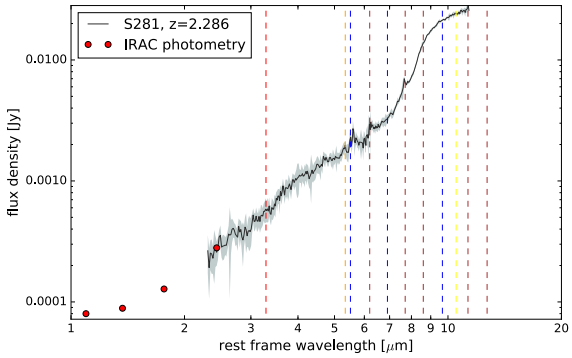
S281, z=2.286
IRAC photometry
flux density [Jy]
0.0100
0.0010
0.0001
1 2 3 4 5 6 7 8 9 10 20
rest frame wavelength [μm]

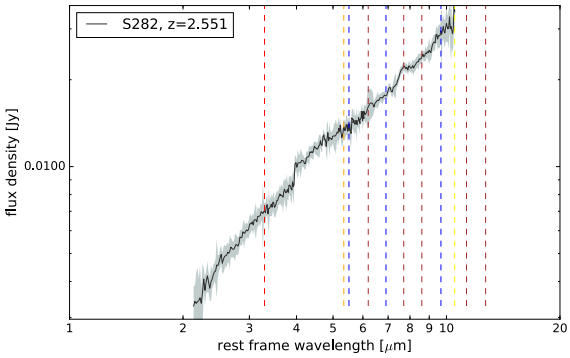
S282, z=2.551
flux density [Jy]
0.0100
1 2 3 4 5 6 7 8 9 10 20
rest frame wavelength [μm]

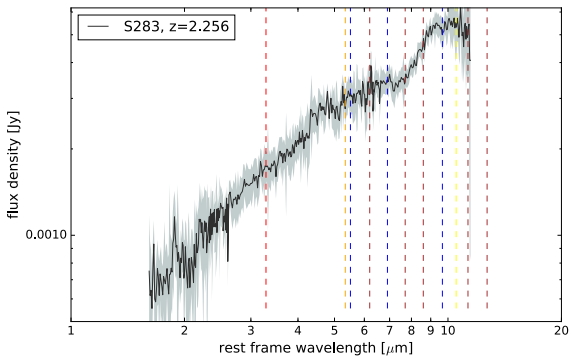
S283, z=2.256
flux density [Jy]
0.0010
1 2 3 4 5 6 7 8 9 10 20
rest frame wavelength [μm]

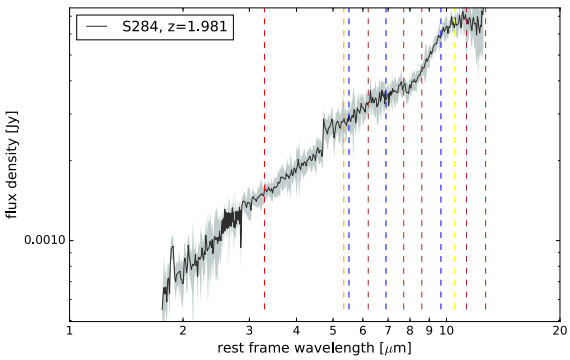
S284, z=1.981
flux density [Jy]
0.0010
1 2 3 4 5 6 7 8 9 10 20
rest frame wavelength [μm]

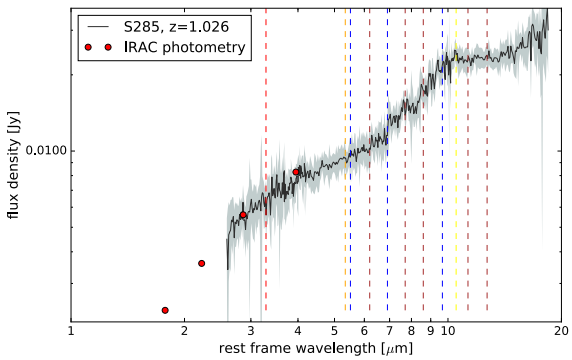
S285, z=1.026
IRAC photometry
flux density [Jy]
0.0100
1 2 3 4 5 6 7 8 9 10 20
rest frame wavelength [μm]

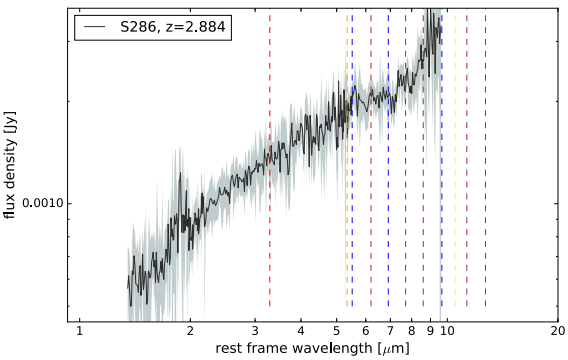
S286, z=2.884
flux density [Jy]
0.0010
1 2 3 4 5 6 7 8 9 10 20
rest frame wavelength [μm]

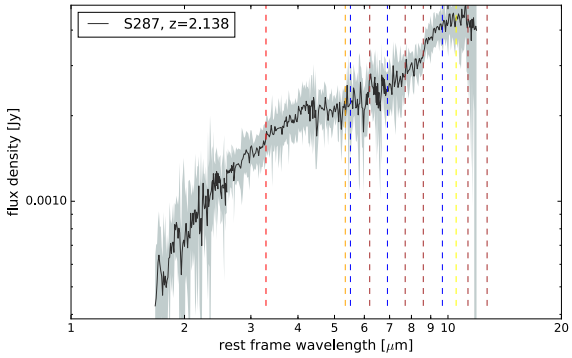
S287, z=2.138
flux density [Jy]
0.0010
rest frame wavelength [μm]

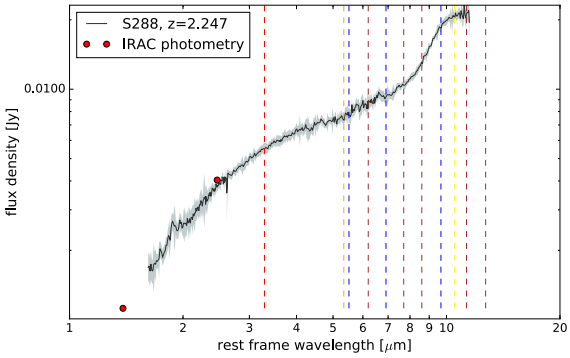
S288, z=2.247
IRAC photometry
flux density [Jy]
0.0100
rest frame wavelength [μm]

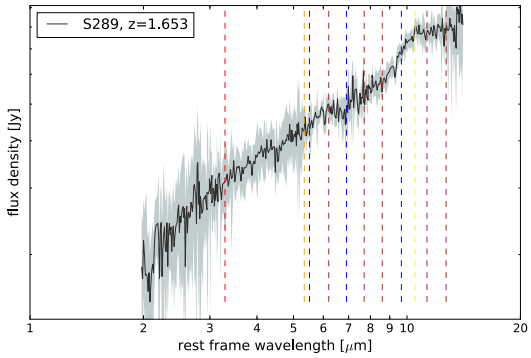
S289, z=1.653
flux density [Jy]
rest frame wavelength [μm]

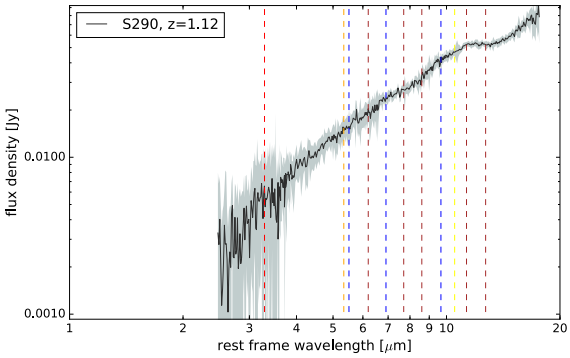
S290, z=1.12
flux density [Jy]
0.0100
0.0010
rest frame wavelength [μm]

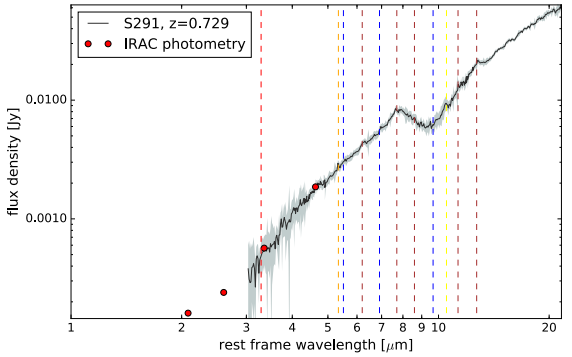
S291, z=0.729
IRAC photometry
flux density [Jy]
0.0100
0.0010
rest frame wavelength [μm]

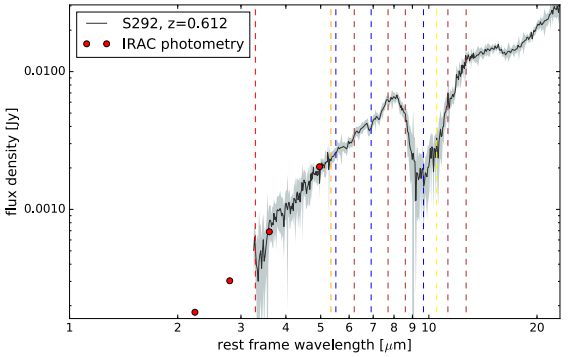
S292, z=0.612
IRAC photometry
flux density [Jy]
0.0100
0.0010
rest frame wavelength [μm]

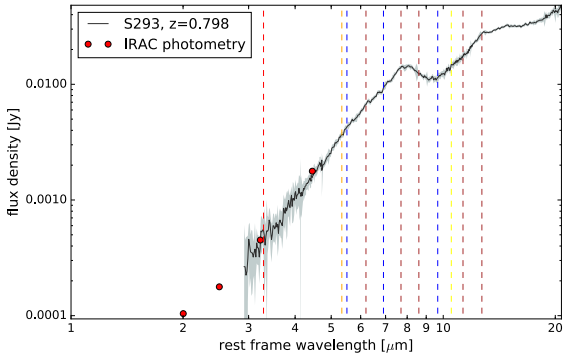
S293, z=0.798
IRAC photometry
flux density [Jy]
0.0100
0.0010
0.0001
rest frame wavelength [μm]

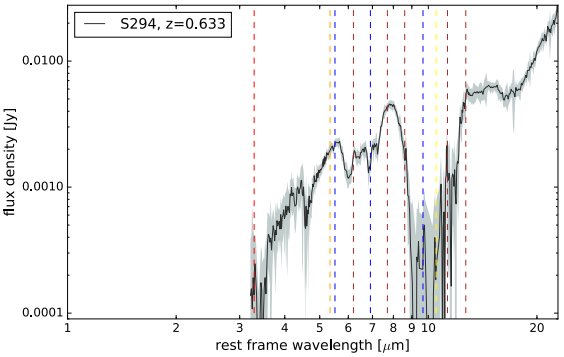
S294, z=0.633
flux density [Jy]
0.0100
0.0010
0.0001
rest frame wavelength [μm]

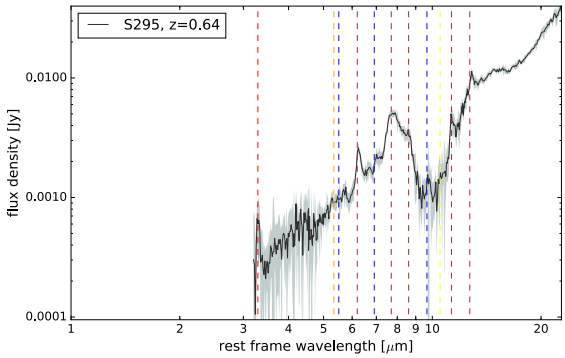
S295, z=0.64
flux density [Jy]
rest frame wavelength [μm]

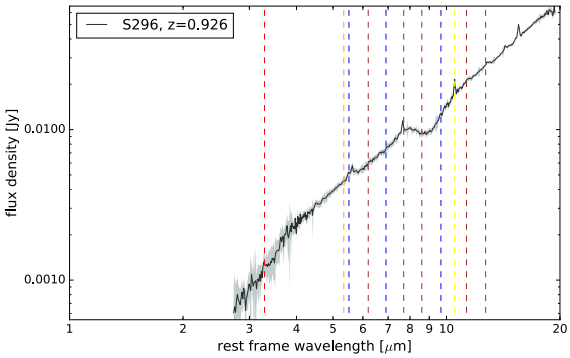
S296, z=0.926
flux density [Jy]
rest frame wavelength [μm]

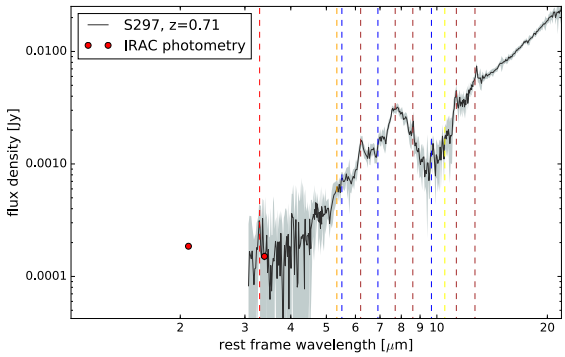
S297, z=0.71
IRAC photometry
flux density [Jy]
rest frame wavelength [μm]

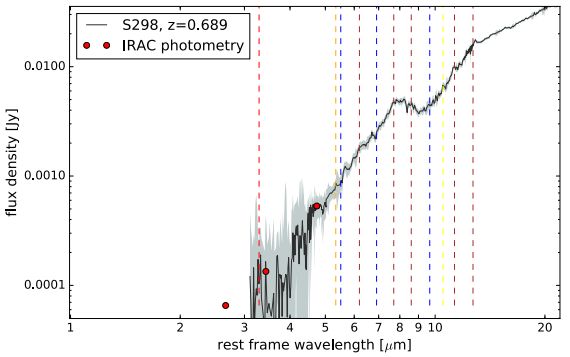
S298, z=0.689
IRAC photometry
flux density [Jy]
rest frame wavelength [μm]

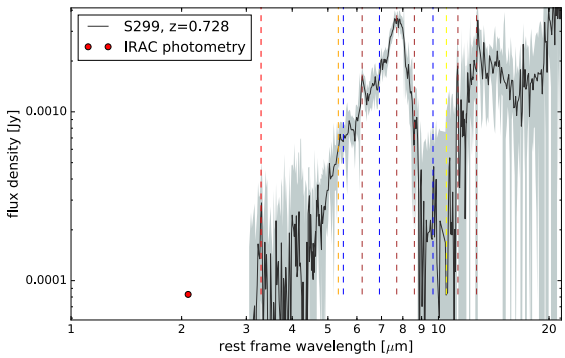
S299, z=0.728
IRAC photometry
flux density [Jy]
rest frame wavelength [μm]

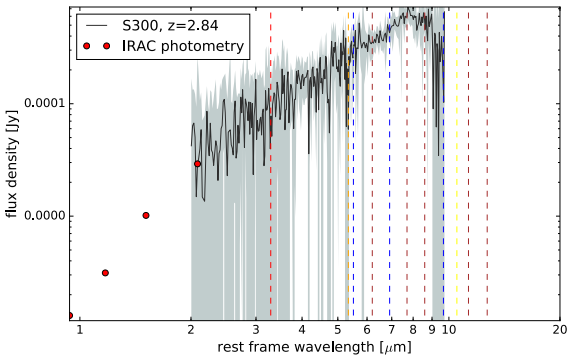
S300, z=2.84
IRAC photometry
flux density [Jy]
rest frame wavelength [μm]

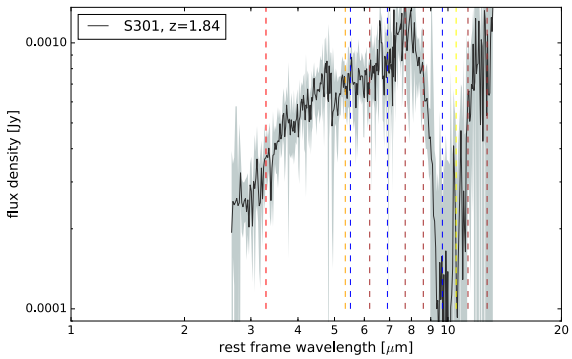
S301, z=1.84
flux density [Jy]
rest frame wavelength [μm]

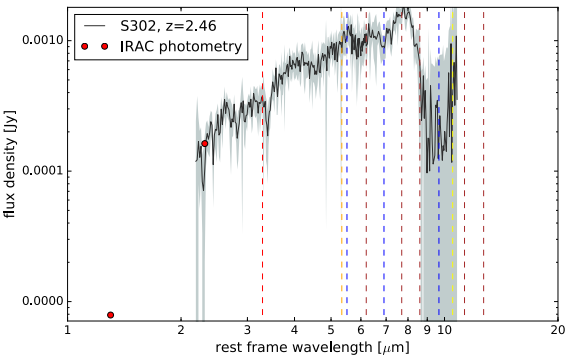
S302, z=2.46
IRAC photometry
flux density [Jy]
rest frame wavelength [μm]

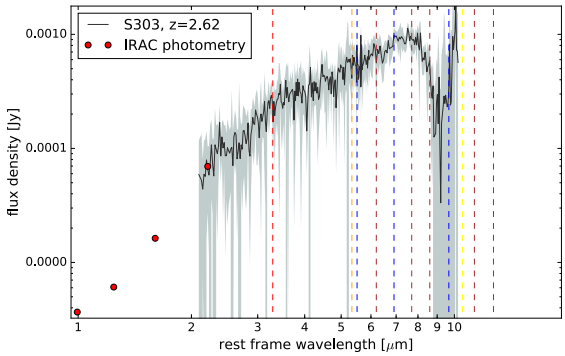
S303, z=2.62
IRAC photometry
flux density [Jy]
rest frame wavelength [μm]

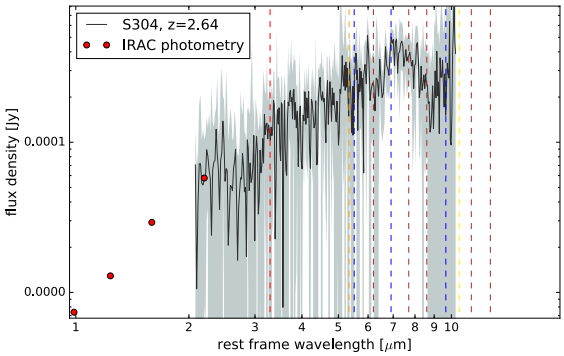
S304, z=2.64
IRAC photometry
flux density [Jy]
rest frame wavelength [μm]

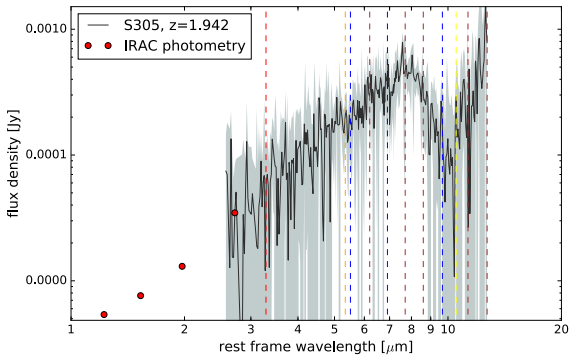
S305, z=1.942
IRAC photometry
flux density [Jy]
rest frame wavelength [μm]

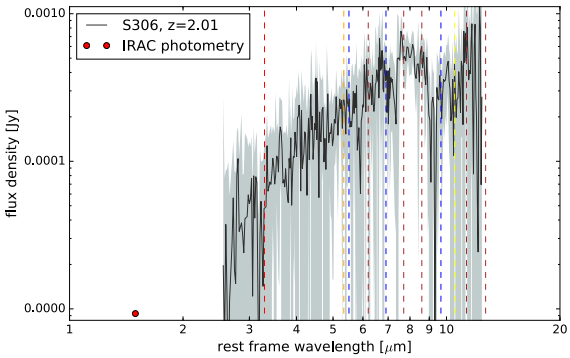
S306, z=2.01
IRAC photometry
flux density [Jy]
rest frame wavelength [μm]

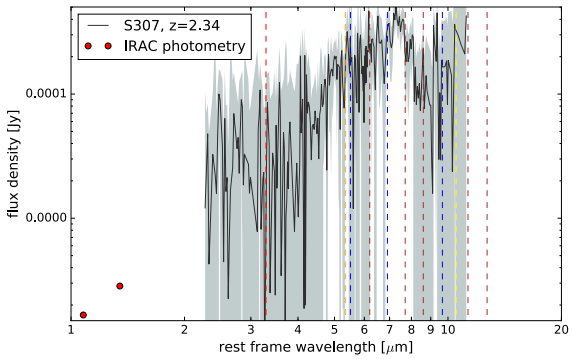
S307, z=2.34
IRAC photometry
flux density [Jy]
rest frame wavelength [μm]

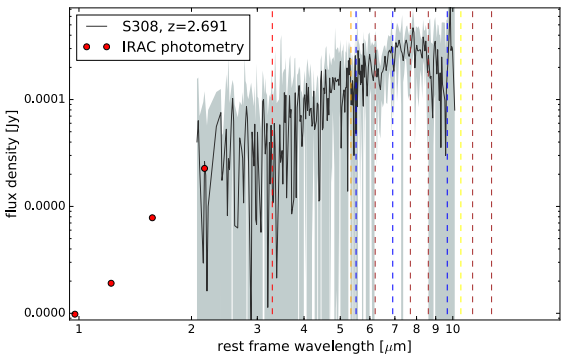
S308, z=2.691
IRAC photometry
flux density [Jy]
rest frame wavelength [μm]

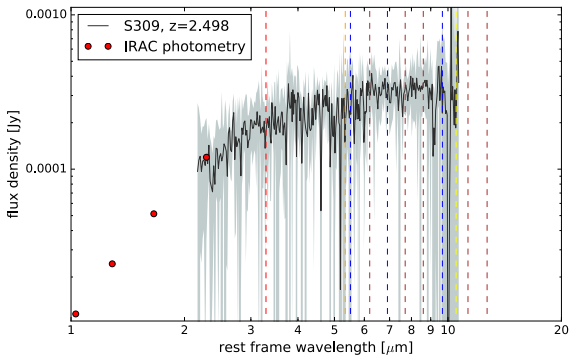
S309, z=2.498
IRAC photometry
flux density [Jy]
rest frame wavelength [μm]

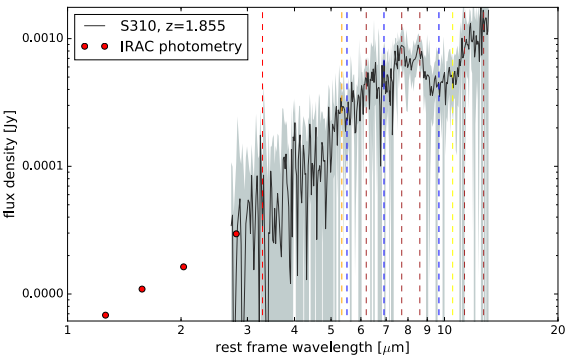
S310, z=1.855
IRAC photometry
flux density [Jy]
rest frame wavelength [μm]

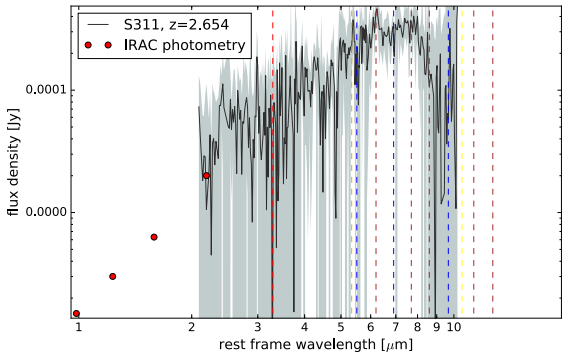
S311, z=2.654
IRAC photometry
flux density [Jy]
0.0001
0.0000
1 2 3 4 5 6 7 8 9 10
rest frame wavelength [μm]

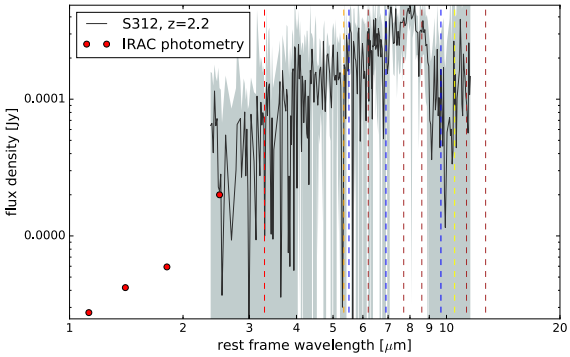
S312, z=2.2
IRAC photometry
flux density [Jy]
0.0001
0.0000
1 2 3 4 5 6 7 8 9 10 20
rest frame wavelength [μm]

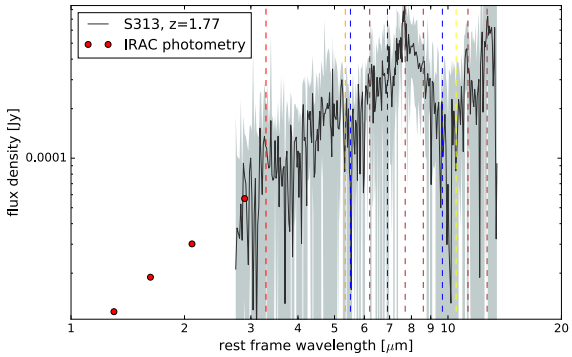
S313, z=1.77
IRAC photometry
flux density [Jy]
0.0001
1 2 3 4 5 6 7 8 9 10 20
rest frame wavelength [μm]

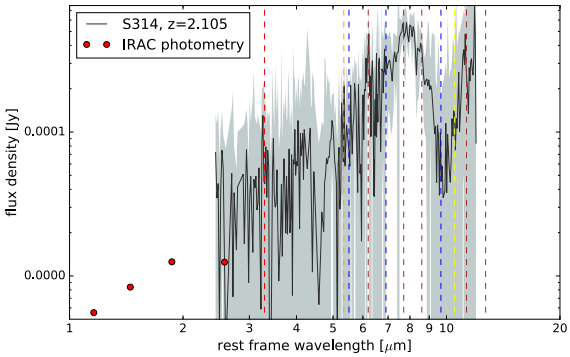
S314, z=2.105
IRAC photometry
flux density [Jy]
0.0001
0.0000
1 2 3 4 5 6 7 8 9 10 20
rest frame wavelength [μm]

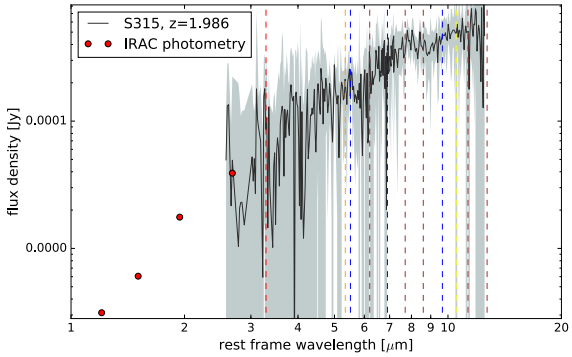
S315, z=1.986
IRAC photometry
flux density [Jy]
0.0001
0.0000
1 2 3 4 5 6 7 8 9 10 20
rest frame wavelength [μm]

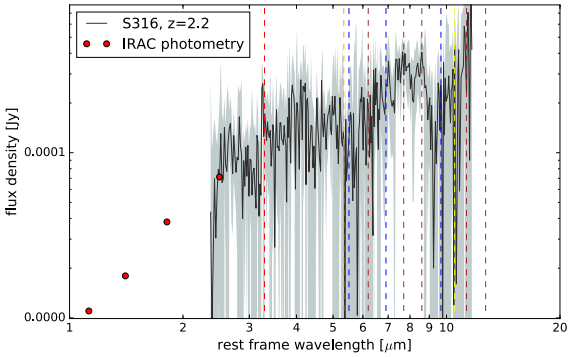
S316, z=2.2
IRAC photometry
flux density [Jy]
0.0001
0.0000
1 2 3 4 5 6 7 8 9 10 20
rest frame wavelength [μm]

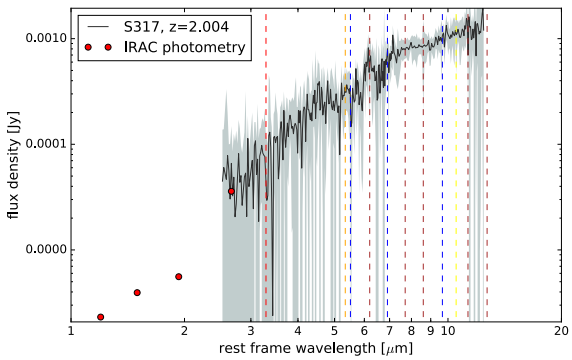
S317, z=2.004
IRAC photometry
flux density [Jy]
0.0010
0.0001
0.0000
1 2 3 4 5 6 7 8 9 10 20
rest frame wavelength [μm]

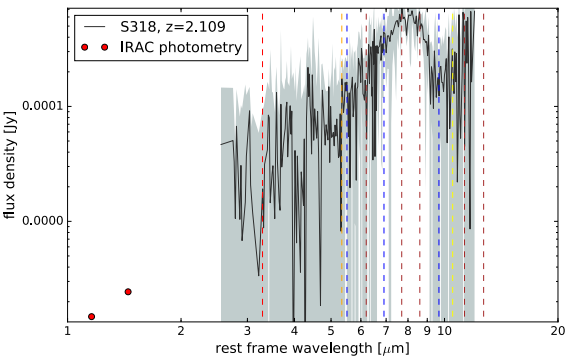
S318, z=2.109
IRAC photometry
flux density [Jy]
0.0001
0.0000
1 2 3 4 5 6 7 8 9 10 20
rest frame wavelength [μm]

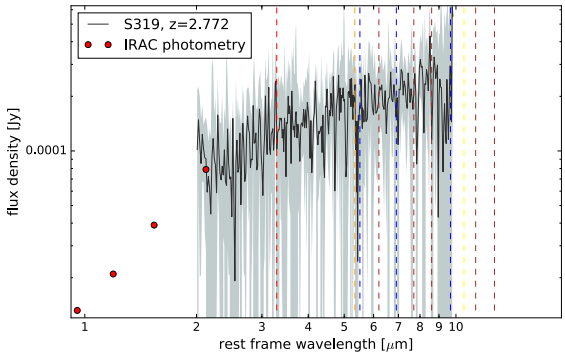
S319, z=2.772
IRAC photometry
flux density [Jy]
0.0001
rest frame wavelength [μm]

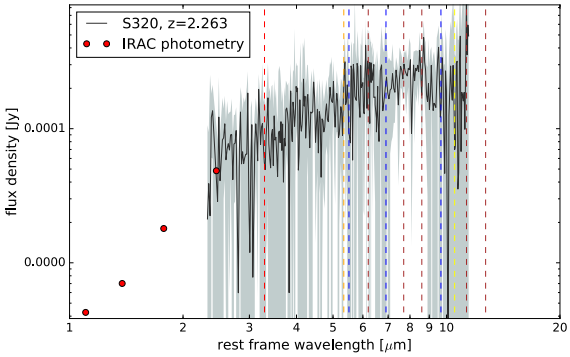
S320, z=2.263
IRAC photometry
flux density [Jy]
0.0001
0.0000
rest frame wavelength [μm]

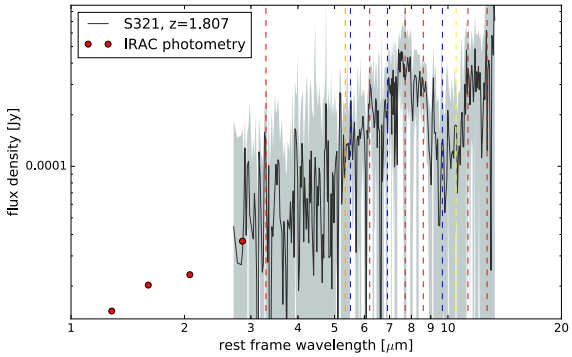
S321, z=1.807
IRAC photometry
flux density [Jy]
0.0001
rest frame wavelength [μm]

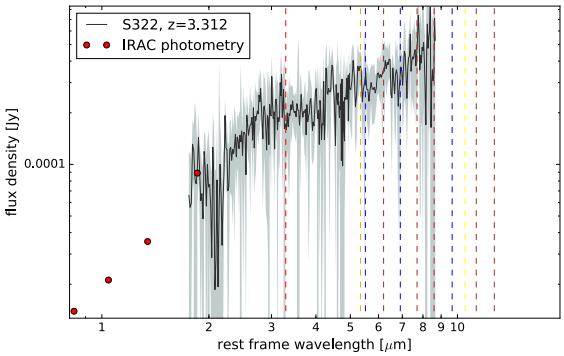
S322, z=3.312
IRAC photometry
flux density [Jy]
0.0001
rest frame wavelength [μm]

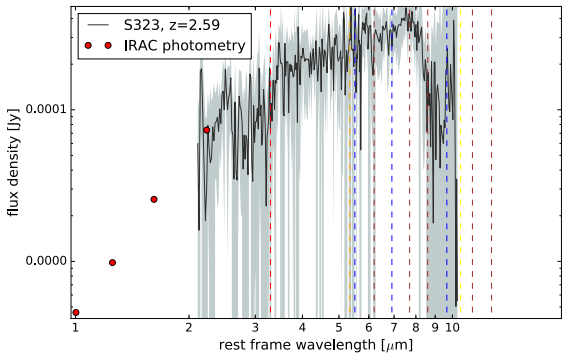
S323, z=2.59
IRAC photometry
flux density [Jy]
0.0001
0.0000
rest frame wavelength [μm]

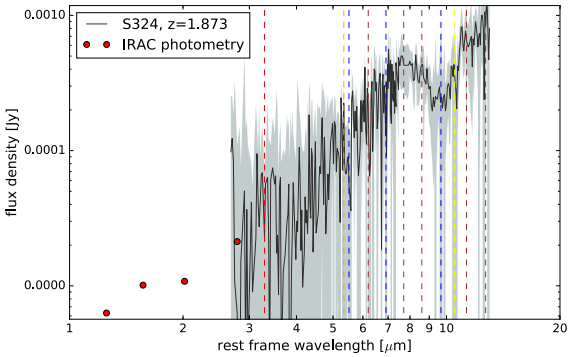
S324, z=1.873
IRAC photometry
flux density [Jy]
0.0010
0.0001
0.0000
rest frame wavelength [μm]

BIBLIOGRAPHY

Bauschlicher Charles W., Jr., Els Peeters, and Louis J. Allamandola (2008). "The Infrared Spectra of Very Large, Compact, Highly Symmetric, Polycyclic Aromatic Hydrocarbons (PAHs)". In: *ApJ* 678, pp. 316–327.

Bauschlicher Charles W., Jr., Els Peeters, and Louis J. Allamandola (2009). "The Infrared Spectra of Very Large Irregular Polycyclic Aromatic Hydrocarbons (PAHs): Observational Probes of Astronomical PAH Geometry, Size, and Charge". In: *ApJ* 697, pp. 311–327.

Bertoldi, F. et al. (2000). "Three high-redshift millimeter sources and their radio and near-infrared identifications". In: *A&A* 360, pp. 92–98.

Borys, C. et al. (2004). "The Hubble Deep Field North SCUBA Super-map - II. Multiwavelength properties". In: *MNRAS* 355, pp. 485–503.

Casey, C. M., D. Narayanan, and A. Cooray (2014). "Dusty star-forming galaxies at high redshift". In: *Phys. Rep.* 541, pp. 45–161.

Ciesla, L. et al. (2015). "Constraining the properties of AGN host galaxies with spectral energy distribution modelling". In: 576, A10, A10.

Cortzen, I. et al. (2019). "PAHs as tracers of the molecular gas in star-forming galaxies". In: *MNRAS* 482, pp. 1618–1633.

Dasyra, Kalliopi M. et al. (2009). "The 0.9 mJy Sample: A Mid-Infrared Spectroscopic Catalog of 150 Infrared-Luminous, 24 m Selected Galaxies at $0.3 \leq z \leq 3.5$". In: *ApJ* 701.2, p. 1123.

Dole, H. et al. (2005). *Probing the Moderate Redshift Galaxies Mid- and Far-Infrared Spectral Energy Distribution [ModzSED]*. Spitzer Proposal.

Donley, J. L. et al. (2012). “Identifying Luminous Active Galactic Nuclei in Deep Surveys: Revised IRAC Selection Criteria”. In: *ApJ* 748, 142, p. 142.

Draine, B. T. and Aigen Li (2001). “Infrared Emission from Interstellar Dust. I. Stochastic Heating of Small Grains”. In: *ApJ* 551.2, p. 807.

Draine, B. T. and Aigen Li (2007a). “Infrared Emission from Interstellar Dust. IV. The Silicate-Graphite-PAH Model in the Post-Spitzer Era”. In: *ApJ* 657.2, p. 810.

Draine, B. T. and Aigen Li (2007b). “Infrared Emission from Interstellar Dust. IV. The Silicate-Graphite-PAH Model in the Post-Spitzer Era”. In: *ApJ* 657, pp. 810–837.

Draine, B.T. (2003). “Interstellar Dust Grains”. In: *ARA&A* 41.1, pp. 241–289.

Fox, M. J. et al. (2002). “The SCUBA 8-mJy survey - II. Multiwavelength analysis of bright submillimetre sources”. In: *MNRAS* 331, pp. 839–852.

Genzel, R. et al. (1998). “What Powers Ultraluminous IRAS Galaxies?” In: *ApJ* 498, pp. 579–605.

Gillett, F. C. and W. J. Forrest (1973). “Spectra of the Becklin-Neugebauer point source and the Kleinmann-Low nebula from 2.8 to 13.5 microns.” In: *ApJ* 179, p. 483.

Gordon, Karl D. et al. (2008). “The Behavior of the Aromatic Features in M101 H II Regions: Evidence for Dust Processing”. In: *ApJ* 682, pp. 336–354.

Hartigan, Patrick, John Raymond, and Rachel Pierson (2004). “Infrared Emission Lines of [Fe II] as Diagnostics of Shocked Gas in Stellar Jets”. In: *ApJ* 614, pp. L69–L71.

Hauser, M. G. et al. (1998). “The COBE Diffuse Infrared Background Experiment Search for the Cosmic Infrared Background. I. Limits and Detections”. In: *ApJ* 508, pp. 25–43.

Hauser, Michael G. and Eli Dwek (2001). “The Cosmic Infrared Background: Measurements and Implications”. In: *ARA&A* 39, pp. 249–307.

Helou, George et al. (2001). “Evidence for the Heating of Atomic Interstellar Gas by Polycyclic Aromatic Hydrocarbons”. In: *ApJ* 548, pp. L73–L76.

Hernán-Caballero, Antonio et al. (2016). “The infrared database of extragalactic observables from Spitzer - I. The redshift catalogue”. In: *MNRAS* 455, pp. 1796–1806.

Hony, S. et al. (2001). “The CH out-of-plane bending modes of PAH molecules in astrophysical environments”. In: *A&A* 370, pp. 1030–1043.

Houck, J. R. et al. (1985). “Unidentified IRAS sources - Ultrahigh-luminosity galaxies”. In: *ApJ* 290, pp. L5–L8.

Huang, J. -S. et al. (2009). “Infrared Spectrograph Spectroscopy and Multi-Wavelength Study of Luminous Star-Forming Galaxies at z 1.9”. In: *ApJ* 700, pp. 183–198.

Imanishi, Masatoshi and C. C. Dudley (2000). “Energy Diagnoses of Nine Infrared Luminous Galaxies Based on 3-4 Micron Spectra”. In: *ApJ* 545, pp. 701–711.

Imanishi, Masatoshi, C. C. Dudley, and Philip R. Maloney (2006). “Infrared 3-4 μm Spectroscopic Investigations of a Large Sample of Nearby Ultraluminous Infrared Galaxies”. In: *ApJ* 637, pp. 114–137.

Imanishi, Masatoshi, Takao Nakagawa, Yoichi Ohyama, et al. (2008). “Systematic Infrared 2.5-5 μm Spectroscopy of Nearby Ultraluminous Infrared Galaxies with AKARI”. In: *PASJ* 60, S489.

Imanishi, Masatoshi, Takao Nakagawa, Mai Shirahata, et al. (2010). “AKARI IRC Infrared 2.5-5 μm Spectroscopy of a Large Sample of Luminous Infrared Galaxies”. In: *ApJ* 721, pp. 1233–1261.

Imanishi, M. et al. (2007). “A Spitzer IRS Low-Resolution Spectroscopic Search for Buried AGNs in Nearby Ultraluminous Infrared Galaxies: A Constraint on Geometry between Energy Sources and Dust”. In: *ApJS* 171, pp. 72–100.

Inami, H. et al. (2018). “The AKARI Spectra of Luminous Infrared Galaxies in the Local Universe”. In: *The Cosmic Wheel and the Legacy of the AKARI Archive: From Galaxies and Stars to Planets and Life*. Ed. by T. Ootsubo et al., pp. 221–224.

Kennicutt Robert C., Jr. (1998). “Star Formation in Galaxies Along the Hubble Sequence”. In: *ARA&A* 36, pp. 189–232.

Kennicutt Jr., Robert C. (1998). “Star formation in galaxies along the Hubble sequence”. In: *ARA&A* 36, pp. 189–231.

Kessler, M. F. et al. (1996). “The Infrared Space Observatory (ISO) mission.” In: *A&A* 315, pp. L27–L31.

Kim, Ji Hoon et al. (2012). “The 3.3 μm Polycyclic Aromatic Hydrocarbon Emission as a Star Formation Rate Indicator”. In: *ApJ* 760, 120, p. 120.

Kirkpatrick, A. et al. (2012). “GOODS-Herschel: Impact of Active Galactic Nuclei and Star Formation Activity on Infrared Spectral Energy Distributions at High Redshift”. In: *ApJ* 759, 139, p. 139.

Kleinmann, D. E. and F. J. Low (1970). “Observations of Infrared Galaxies”. In: *ApJ* 159, p. L165.

Lacy, M., A. O. Petric, et al. (2007). “Optical Spectroscopy and X-Ray Detections of a Sample of Quasars and Active Galactic Nuclei Selected in the Mid-Infrared from Two Spitzer Space Telescope Wide-Area Surveys”. In: *AJ* 133.1, p. 186.

Lacy, M., L. J. Storrie-Lombardi, et al. (2004). “Obscured and Unobscured Active Galactic Nuclei in the Spitzer Space Telescope First Look Survey”. In: *ApJS* 154.1, p. 166.

Laurent, O. et al. (2000). “Mid-infrared diagnostics to distinguish AGNs from starbursts”. In: *A&A* 359, pp. 887–899.

Lebouteiller, V. et al. (2011). “CASSIS: The Cornell Atlas of Spitzer/Infrared Spectrograph Sources”. In: *ApJS* 196, 8, p. 8.

Levenson, N. A. et al. (2007). “Deep Mid-Infrared Silicate Absorption as a Diagnostic of Obscuring Geometry toward Galactic Nuclei”. In: *ApJ* 654, pp. L45–L48.

Lonsdale, C. J., D. Farrah, and H. E. Smith (2006). “Ultraluminous Infrared Galaxies”. In: *Astrophysics Update 2*. Ed. by J. W. Mason, p. 285.

Low, J. and D. E. Kleinmann (1968). “Proceedings of the Conference on Seyfert Galaxies and Related Objects: 17. Infrared Observations of Seyfert Galaxies, Quasistellar Sources, and Planetary Nebulae”. In: *AJ* 73, p. 868.

Lutz, Dieter (2014). “Far-infrared surveys of galaxy evolution”. In: *ARA&A* 52, pp. 373–414.

Lutz, D. et al. (1996). “What powers luminous infrared galaxies?” In: *A&A* 315, pp. L137–L140.

Madden, S. C. et al. (2006). “ISM properties in low-metallicity environments”. In: *A&A* 446, pp. 877–896.

Magdis, G. E. et al. (2013). “Mid- to far-infrared properties of star-forming galaxies and active galactic nuclei”. In: *A&A* 558, A136, A136.

Magnelli, B. et al. (2009). “The 0.4 < z < 1.3 star formation history of the Universe as viewed in the far-infrared”. In: *A&A* 496, pp. 57–75.

Marshall, J. A. et al. (2018). “The Nature of Deeply Buried Ultraluminous Infrared Galaxies: A Unified Model for Highly Obscured Dusty Galaxy Emission”. In: *ApJ* 858.1, p. 59.

Menéndez-Delmestre, Karın et al. (2009). “Mid-Infrared Spectroscopy of Submillimeter Galaxies: Extended Star Formation in Massive High-redshift Galaxies”. In: *ApJ* 699, pp. 667–685.

Moorwood, A. F. M. (1986). “3.28 mu-m feature and continuum emission in galaxy nuclei.” In: *A&A* 166, pp. 4–12.

Negrello, M. et al. (2009). “Photometric redshift accuracy in AKARI deep surveys”. In: *MNRAS* 394, pp. 375–397.

Noll, S. et al. (2009). “Analysis of galaxy spectral energy distributions from far-UV to far-IR with CIGALE: studying a SINGS test sample”. In: 507, pp. 1793–1813.

Peeters, E., L. J. Allamandola, et al. (2004). “The Unidentified InfraRed Features after ISO”. In: *Astrophysics of Dust*. Ed. by Adolf N. Witt, Geoffrey C. Clayton, and Bruce T. Draine. Vol. 309, p. 141.

Peeters, E., C. W. Bauschlicher Jr., et al. (2017). “The PAH Emission Characteristics of the Reflection Nebula NGC 2023”. In: *ApJ* 836, 198, p. 198.

Peeters, E., S. Hony, et al. (2002). “The rich 6 to 9 vec mu m spectrum of interstellar PAHs”. In: *A&A* 390, pp. 1089–1113.

Peeters, E., H. W. W. Spoon, and A. G. G. M. Tielens (2004). “Polycyclic Aromatic Hydrocarbons as a Tracer of Star Formation?” In: *ApJ* 613, pp. 986–1003.

Pilbratt, G. L. et al. (2010). “Herschel Space Observatory. An ESA facility for far-infrared and submillimetre astronomy”. In: *A&A* 518, L1, p. L1.

Puget, J. -L. et al. (1996). “Tentative detection of a cosmic far-infrared background with COBE.” In: *A&A* 308, p. L5.

Rieke, G. H. and M. J. Lebofsky (1979). “Infrared emission of extragalactic sources”. In: *ARA&A* 17, pp. 477–511.

Risaliti, G., M. Imanishi, and E. Sani (2010). “A quantitative determination of the AGN content in local ULIRGs through L-band spectroscopy”. In: *MNRAS* 401, pp. 197–203.

Risaliti, G., R. Maiolino, et al. (2006). “Unveiling the nature of Ultraluminous Infrared Galaxies with 3-4μm spectroscopy*”. In: *MNRAS* 365, pp. 303–320.

Roussel, H. et al. (2001). “The relationship between star formation rates and mid-infrared emission in galactic disks”. In: *A&A* 372, pp. 427–437.

Rowan-Robinson, M. et al. (1991). “A high-redshift IRAS galaxy with huge luminosity - Hidden quasar or protogalaxy?” In: *Nature* 351, pp. 719–721.

Rujopakarn, W. et al. (2013). “Mid-infrared Determination of Total Infrared Luminosity and Star Formation Rates of Local and High-redshift Galaxies”. In: *ApJ* 767, 73, p. 73.

Russell, R. W., B. T. Soifer, and K. M. Merrill (1977). “Observations of the unidentified 3.3 micrometer emission feature in nebulae.” In: *ApJ* 213, pp. 66–70.

Sajina, Anna et al. (2009). “Detections of Water Ice, Hydrocarbons, and 3.3 μm PAH in z 2 ULIRGs”. In: *ApJ* 703, pp. 270–284.

Sajina, Anna et al. (2007). “Spitzer Mid-Infrared Spectroscopy of Infrared Luminous Galaxies at z 2. II. Diagnostics”. In: *ApJ* 664.2, p. 713.

Sánchez, S. F. et al. (2004). “Colors of Active Galactic Nucleus Host Galaxies at 0.5z1.1 from the GEMS Survey”. In: *ApJ* 614, pp. 586–606.

Sani, E. et al. (2008). “3-5 μm Spectroscopy of Obscured AGNs in ULIRGs”. In: *ApJ* 675, pp. 96–105.

Schmidt, Maarten (1959). “The Rate of Star Formation.” In: *ApJ* 129, p. 243.

Siana, B. et al. (2009). “Detection of Far-Infrared and Polycyclic Aromatic Hydrocarbon Emission from the Cosmic Eye: Probing the Dust and Star Formation of Lyman Break Galaxies”. In: *ApJ* 698, pp. 1273–1281.

Sloan, G. C. et al. (1999). “Direct Spectroscopic Evidence for Ionized Polycyclic Aromatic Hydrocarbons in the Interstellar Medium”. In: *ApJl* 513.1, p. L65.

Smith, J. D. T. et al. (2007). “The Mid-Infrared Spectrum of Star-forming Galaxies: Global Properties of Polycyclic Aromatic Hydrocarbon Emission”. In: *ApJ* 656, pp. 770–791.

Soifer, B. T. and G. Neugebauer (1991). “The properties of infrared galaxies in the local universe”. In: *AJ* 101, pp. 354–361.

Soifer, B. T., G. Neugebauer, and J. R. Houck (1987). “The IRAS view of the extragalactic sky.” In: *ARA&A* 25, pp. 187–230.

Soifer, B. T., R. W. Russell, and K. M. Merrill (1976). “2 - 4 micron spectrophotometric observations of the galactic center.” In: *ApJ* 207, pp. L83–L85.

Spoon, H. W. W. et al. (2007). “Mid-Infrared Galaxy Classification Based on Silicate Obscuration and PAH Equivalent Width”. In: *ApJ* 654, pp. L49–L52.

Stanford, S. A. et al. (2000). “The FIRST Sample of Ultraluminous Infrared Galaxies at High Redshift. I. Sample and Near-Infrared Morphologies”. In: *ApJS* 131, pp. 185–221.

Stern, Daniel et al. (2005). “Mid-Infrared Selection of Active Galaxies”. In: *ApJ* 631.1, p. 163.

Strauss, M. A. et al. (1990). “A redshift survey of IRAS galaxies. I - Sample selection”. In: *ApJ* 361, pp. 49–62.

Sturm, E. et al. (2000). “ISO-SWS spectra of galaxies: Continuum and features”. In: *A&A* 358, pp. 481–493.

Surace, J. A. et al. (1998). “HST/WFPC2 Observations of Warm Ultraluminous Infrared Galaxies”. In: *ApJ* 492, pp. 116–136.

Tielens, A. G. G. M. (2008). “Interstellar polycyclic aromatic hydrocarbon molecules.” In: *ARA&A* 46, pp. 289–337.

Voit, G. M. (1992). “Destruction and survival of polycyclic aromatic hydrocarbons in active galaxies”. In: *MNRAS* 258, pp. 841–848.

Wada, Koji et al. (2009). “Collisional Growth Conditions for Dust Aggregates”. In: *ApJ* 702.2, p. 1490.

Webb, T. M. A. et al. (2003). “The Canada-UK Deep Submillimeter Survey. VII. Optical and Near-Infrared Identifications for the 14 Hour Field”. In: *ApJ* 597, pp. 680–698.

Weedman, D. W. et al. (2005). “Mid-Infrared Spectra of Classical AGNs Observed with the Spitzer Space Telescope”. In: *ApJ* 633, pp. 706–716.

Werner, M. W. et al. (2004). “The Spitzer Space Telescope Mission”. In: *ApJS* 154, pp. 1–9.

Woo, Jong-Hak et al. (2012). “The Connection between 3.3 μm Polycyclic Aromatic Hydrocarbon Emission and Active Galactic Nucleus Activity”. In: *AJ* 143, 49, p. 49.

Yan, Lin et al. (2007). “Spitzer Mid-Infrared Spectroscopy of Infrared Luminous Galaxies at z$\sim$2 I: the Spectra”. In: *ApJ* 658, pp. 778–793.